

THE BIASES OF OPTICAL LINE-RATIO SELECTION FOR ACTIVE GALACTIC NUCLEI, AND THE INTRINSIC RELATIONSHIP BETWEEN BLACK HOLE ACCRETION AND GALAXY STAR FORMATION

JONATHAN R. TRUMP,^{1,†} MOUYUAN SUN,^{1,2} GREGORY R. ZEIMANN,¹ CUYLER LUCK,³ JOANNA S. BRIDGE,¹ CATHERINE J. GRIER,¹ ALEX HAGEN,¹ STEPHANIE JUNEAU,⁴ ANTONIO MONTERO-DORTA,⁵ DAVID J. ROSARIO,⁶ W. NIEL BRANDT,¹ ROBIN CIARDULLO,¹ AND DONALD P. SCHNEIDER¹*Draft version September 3, 2015*

ABSTRACT

We use 317,000 emission-line galaxies from the Sloan Digital Sky Survey to investigate line-ratio selection of active galactic nuclei (AGNs). In particular, we demonstrate that “star formation dilution” by HII regions causes a significant bias against AGN selection in low-mass, blue, star-forming, disk-dominated galaxies. This bias is responsible for the observed preference of AGNs among high-mass, green, moderately star-forming, bulge-dominated hosts. We account for the bias and simulate the intrinsic population of emission-line AGNs using a physically-motivated Eddington ratio distribution, intrinsic AGN narrow line region line ratios, a luminosity-dependent $L_{\text{bol}}/L[\text{OIII}]$ bolometric correction, and the observed $M_{\text{BH}} - \sigma$ relation. These simulations indicate that, in massive ($\log(M_*/M_\odot) \gtrsim 10$) galaxies, AGN accretion is correlated with specific star formation rate but is otherwise uniform with stellar mass. There is some hint of lower black hole occupation in low-mass ($\log(M_*/M_\odot) \lesssim 10$) hosts, although our modeling is limited by uncertainties in measuring and interpreting the velocity dispersions of low-mass galaxies. The presence of star formation dilution means that AGNs contribute little to the observed strong optical emission lines (e.g., [OIII] and H α) in low-mass and star-forming hosts. However the AGN population recovered by our modeling indicates that feedback by typical (low- to moderate-accretion) low-redshift AGNs has nearly uniform efficiency at all stellar masses, star formation rates, and morphologies. Taken together, our characterization of the observational bias and resultant AGN occupation function suggest that AGNs are unlikely to be the dominant source of star formation quenching in galaxies, but instead are fueled by the same gas which drives star formation activity.

Subject headings: galaxies: active – galaxies: nuclei – galaxies: Seyfert – quasars: emission lines – galaxies: evolution

1. INTRODUCTION

The observed correlations between the mass of a galaxy’s bulge and the mass of its supermassive black hole (SMBH) (e.g., Magorrian et al. 1998; Gebhardt et al. 2000; Ferrarese & Merritt 2000; Marconi & Hunt 2003; Kormendy & Ho 2013) imply that galaxy growth via star formation (SF) must have a corresponding period of SMBH growth in the active galactic nucleus (AGN) phase. Yet the details that couple AGN-galaxy coevolution remain mysterious. Theoretical frameworks invoke mergers (e.g., Sanders et al. 1988; Di Matteo, Springel, & Hernquist 2005; Hopkins et al. 2006, 2008), violent disk instabilities (Dekel et al. 2009; Bournaud et al.

2011; Gabor & Bournaud 2013), or secular processes in gas-rich disks (e.g., Shlosman et al. 1989; Hopkins & Hernquist 2009; Hopkins et al. 2014) to simultaneously (or near-simultaneously, e.g., Wild et al. 2010) fuel rapid star formation and drive gas inward to power an AGN. Many simulations also invoke AGN “feedback” which quenches star formation through gas blowout by radiative winds (Silk & Rees 1998; Fabian 2002; Di Matteo, Springel, & Hernquist 2005) or gas heating by radio jets (Croton et al. 2006). Both AGN feedback and coupled AGN-SF fueling leave an imprint on the observed properties (e.g., color, star formation rate, and morphology) of AGN host galaxies. This scenario means the physical processes behind AGN-galaxy coevolution can be revealed by the simple question: *Are AGN host galaxies special?*

In seminal work Kauffmann et al. (2003) used $\sim 120,000$ galaxies from the Sloan Digital Sky Survey (SDSS, York et al. 2000) to demonstrate that AGNs are most frequently observed in massive bulge-dominated galaxies, with more luminous AGNs found in host galaxies with more recent star formation. Kauffmann et al. (2003), along with subsequent work reaching similar conclusions (Heckman et al. 2004; Schawinski et al. 2010), selected AGNs using the characteristic optical signature of the AGN narrow line region (NLR): AGN emission produces higher ratios of partially ionized forbidden lines compared to Balmer recombination lines (Baldwin et al. 1981; Veilleux & Osterbrock

¹ Department of Astronomy and Astrophysics and Institute for Gravitation and the Cosmos, 525 Davey Lab, The Pennsylvania State University, University Park, PA 16802, USA

² Department of Astronomy and Institute of Theoretical Physics and Astrophysics, Xiamen University, Xiamen, Fujian 361005, China

³ State College High School, 650 Westerly Parkway, State College, PA 16801, USA

⁴ Irfu/Service d’Astrophysique, CEA-Saclay, Orme des Merisiers, 91191 Gif-sur-Yvette Cedex, France

⁵ Department of Physics and Astronomy, The University of Utah, 115 South 1400 East, Salt Lake City, UT 84112, USA

⁶ Max-Planck-Institut für extraterrestrische Physik (MPE), Giessenbachstrasse 1, D-85748 Garching bei München, Germany

[†] Hubble Fellow

1987). Studies of AGN host galaxies using large samples with X-ray (Nandra et al. 2007; Salim et al. 2007; Georgakakis et al. 2008; Silverman et al. 2008; Schawinski et al. 2009; Hickox et al. 2009; Kocevski et al. 2009; Haggard et al. 2010), infrared (Hickox et al. 2009), and radio (Best et al. 2005) AGN selection found a similar observed preference for massive and bulge-dominated hosts, with infrared \Rightarrow X-ray \Rightarrow radio corresponding to a sequence in declining star formation rate (SFR) in the host galaxy (Hickox et al. 2009). Taken together these observations implied a critical stellar mass for accretion onto an AGN, with indirect evidence for AGN feedback in the green/red colors of X-ray/radio AGN host galaxies.

More recent studies, however, have suggested that the apparent green-valley preference of X-ray AGNs is purely a relic of selection effects (Silverman et al. 2009; Xue et al. 2010). There is also a mass bias for AGN selection at a fixed accretion rate (Aird et al. 2012), most easily understood with the unitless Eddington ratio, $\lambda_{\text{Edd}} \equiv L_{\text{bol}}/L_{\text{Edd}}$. The bolometric luminosity is driven by mass accretion, $L_{\text{bol}} = \eta \dot{M} c^2$, and the Eddington luminosity is defined as $L_{\text{Edd}} = (1.3 \times 10^{38} \text{ erg s}^{-1}) M_{\text{BH}}/M_{\odot}$, so that $L_{\text{bol}}/L_{\text{Edd}} \simeq 0.44\eta(\dot{M}/\text{Gyr}^{-1})/M_{\text{BH}}$. The radiative efficiency $\eta \sim 0.1$ at $\dot{m} \equiv \dot{M}/[L_{\text{Edd}}/(\eta c^2)] \gtrsim 10^{-2}$, while lower accretion rates lead to radiatively inefficient accretion and $\log(\eta) \sim -1 + 0.5 \log(\dot{m}/10^{-2})$ (Xie & Yuan 2012). The Eddington ratio better describes the mode of AGN accretion and feedback than does luminosity, as the AGN accretion flow changes from a geometrically thin accretion disk with radiative winds at $\lambda_{\text{Edd}} \gtrsim 0.01$ to a radiatively inefficient accretion flow with stronger radio jets at $\lambda_{\text{Edd}} \lesssim 0.01$ (Narayan & McClintock 2008; Ho 2008; Trump et al. 2011a; Heckman & Best 2014). Because M_{BH} is correlated with galaxy bulge mass M_{bulge} , which is in turn correlated with total stellar mass M_* , a given AGN flux limit means it is easier to find lower- λ_{Edd} AGNs in high-mass galaxies than in low-mass galaxies. The λ_{Edd} function for AGNs is likely to steeply decline with increasing accretion rate, since there are many more weakly-accreting than rapidly-accreting AGNs in the local universe (e.g., Ho 2008). In a flux-limited sample this results in a steep bias towards finding more AGNs in massive hosts.

Aird et al. (2012) reported that the X-ray AGN host occupation fraction is consistent with a *uniform AGN Eddington ratio distribution across all host galaxy stellar masses*. Thus, after controlling for selection bias, AGN host galaxies are not special in terms of stellar mass. It remains unclear if AGN host galaxies are special in SFR or morphology. Recent work combining far-infrared observations with X-ray selection demonstrates that AGNs are most common in star-forming galaxies (Mullaney et al. 2012; Harrison et al. 2012; Juneau et al. 2013; Rosario et al. 2013a,b; Chen et al. 2013). This result is generally similar to the connection between AGN luminosity and host galaxy SFR seen in the initial line-ratio AGN⁸ sample of Kauffmann et al. (2003) and in subsequent studies of broad-line AGN hosts (Trump et al. 2013a; Matsuoka et al. 2014). In terms of

host morphology, most recent observations demonstrate that AGNs are not preferentially fueled by major mergers (Grogin et al. 2005; Gabor et al. 2009; Cisternas et al. 2011; Kocevski et al. 2012), although mergers may play a role in fueling nearby AGNs that are very luminous and/or obscured (Koss et al. 2010; Ellison et al. 2011; Treister et al. 2012; Trump 2013b). Observations are mixed on whether violent disk instabilities play a significant role in AGN fueling, with evidence both for (Bournaud et al. 2012) and against (Trump et al. 2014). So while X-ray AGN hosts do not appear to be special in their stellar mass, it remains under debate if they are special in SFR or morphology. And it is still unclear how the larger population of line-ratio AGNs connect to this X-ray picture.

In this work we use line-ratio AGN selection to recover the intrinsic AGN occupation fraction with host galaxy properties. For this purpose we use a very large sample of $>300,000$ galaxies from the SDSS, described in Section 2. Just as Kauffmann et al. (2003) originally found, Section 3 demonstrates that line-ratio AGNs are observed to be most common in massive, concentrated galaxies with intermediate colors and specific star formation rates (sSFRs). The selection bias for line-ratio AGNs is a function of the contrast between AGN and galaxy emission lines rather than a simple flux limit, and in Section 4 we quantify this bias with host galaxy properties. In Section 5 we model the intrinsic AGN population as a function of galaxy properties, beginning with a uniform Eddington ratio distribution, then allowing Eddington ratio and black hole occupation to vary with galaxy properties. Section 6 describes the implications of the modeled AGN occupation function for galaxy emission-line measurements, the connection between AGN accretion and galaxy SFR, AGN feedback, and black hole seed formation. Throughout the paper we use a basic Λ CDM cosmology with $h = 0.70$, $\Omega_M = 0.3$, $\Omega_\Lambda = 0.7$.

2. OBSERVATIONAL DATA

Our galaxy sample is drawn from the Sloan Digital Sky Survey (SDSS, York et al. 2000). SDSS data include *ugriz* broad-band photometry (Fukugita et al. 1996) and spectroscopy with $R \sim 2000$ over $3800 < \lambda < 9200 \text{ \AA}$ (Smee et al. 2013), taken using a 2.5-m telescope at Apache Point Observatory (Gunn et al. 2006). The galaxy sample in this work is drawn from the SDSS Data Release 10 (Ahn et al. 2014), which covers a total sky area of $14,555 \text{ deg}^2$. We used the public SkyServer SQL server⁹ to select a parent sample of 317,192 galaxies (`class=GALAXY`) with $r < 17.77$, spectroscopic redshifts in the range $0.01 < z < 0.1$, and line flux errors of $0 < \sigma_{\text{line}} < 10^{-15} \text{ erg s}^{-1} \text{ cm}^{-2}$ (to remove bad spectra). The r -magnitude limit represents the main spectroscopy limit of the SDSS galaxy survey (Strauss et al. 2002). The limits in the line flux errors effectively remove objects with problematic spectra (artifacts and bad pixels) in the line regions. These spectral issues are uncorrelated with galaxy properties and are essentially random occurrences.

The redshift range of $0.01 < z < 0.1$ is designed to include a broad range of galaxy stellar masses without significant evolution in galaxy properties. The up-

⁸ Throughout the paper we refer to AGNs selected by Seyfert-like optical line ratios as “line-ratio AGNs.”

⁹ <http://skyserver.sdss3.org/dr10/en/tools/search/sql.aspx>

per limit in redshift corresponds roughly to a mass limit of $\log(M_*/M_\odot) \gtrsim 10.7$ with the SDSS magnitude limit, and the lower redshift limit adds lower-mass galaxies to $\log(M_*/M_\odot) \gtrsim 8$. In Section 4.1 we demonstrate that the fractional coverage of the SDSS fiber varies by $\lesssim 20\%$ over the stellar mass range of the full sample. There is also minimal galaxy evolution within this redshift range: for example, the cosmic SFR evolves by $\lesssim 25\%$ (Wyder et al. 2005; Cucciati et al. 2012; Madau & Dickinson 2014). Thus we do not expect a significant change in AGN fraction with redshift driven by changing galaxy properties.

SDSS galaxies have redshifts and line measurements computed using the `idlspec2d` software: details of this automated processing are given by Bolton et al. (2012). In brief, galaxy classifications and redshifts are computed by finding the best-fit (minimum- χ^2) template, with templates constructed from sets of eigenspectra derived from a principal component analysis of training spectra. Emission line fluxes are computed using the best-fit velocity dispersion template as the continuum, which implicitly corrects for stellar absorption. Each line is fit as a Gaussian, with line width fixed across the Balmer lines, and a separate fixed line width for the group of all other emission lines visible in our redshift range.

Stellar velocity dispersion is computed by fitting a set of stellar templates from the library of Prugniel & Soubiran (2001), degrading the templates to match the instrumental broadening ($\sim 70 \text{ km s}^{-1}$) and minimizing χ^2 over a grid of $0 < \sigma < 850 \text{ km s}^{-1}$ with 25 km s^{-1} bins. Since these velocity dispersions are fit using the stellar absorption lines, they are unaffected by AGN emission. Low-mass galaxies ($\log(M_*) < 10^{10} M_\odot$) tend to have measured dispersions less than the instrumental resolution: we include dispersions for these galaxies using survival analysis (e.g., Feigelson & Nelson 1985) on their $1\text{-}\sigma$ upper limits. The lack of reliable velocity dispersions in low-mass galaxies is an issue we return to in Sections 5 and 6.

We create samples of galaxies with well-measured line ratios, following Juneau et al. (2014) and requiring the signal-to-noise ratio (S/N) of the line ratios to have $(S/N)_{\text{ratio}} > 3/\sqrt{2}$. This is the equivalent of each line detected at $(S/N)_{\text{line}} > 3$, but has the advantage of including well-constrained line ratios where one line is bright and the other faint (for example, $H\beta$ is frequently bright and $[\text{OIII}]\lambda 5007$ weak in massive galaxies, and $H\alpha$ is bright and $[\text{NII}]\lambda 6584$ weak in low-metallicity galaxies). From the parent sample of 317,192 galaxies with $r < 17.77$ and $0.01 < z < 0.1$, 223,448 galaxies possess each of the $[\text{OIII}]\lambda 5007/H\beta$ and $[\text{NII}]\lambda 6584/H\alpha$ ratios measured at $(S/N)_{\text{ratio}} > 3/\sqrt{2}$: these lines form the “BPT” (Baldwin et al. 1981) diagram and so we designate this galaxy set as the “BPT well-measured sample.” Similarly the $[\text{OIII}]\lambda 5007/H\beta$ and $([\text{SII}]\lambda 6717 + 6731)/H\alpha$ ratios define the “VO87” (Veilleux & Osterbrock 1987) diagram, and the “VO87 well-measured sample” includes the 215,242 galaxies with these ratios measured at $(S/N)_{\text{ratio}} > 3/\sqrt{2}$. For most galaxies the $(S/N)_{\text{ratio}}$ threshold corresponds to a line flux limit of $f \gtrsim 1 \times 10^{-16} \text{ erg s}^{-1} \text{ cm}^{-2}$. Our line-ratio classifications generally use only these well-measured samples, although we also discuss the likely AGN fraction among the full

parent sample of galaxies (including those with poorly-measured line ratios) in Section 3.3.

Unless otherwise specified, the emission-line luminosities in each galaxy are dust-corrected using the measured Balmer decrement and a Cardelli et al. (1989) attenuation curve with O’Donnell (1994) coefficients. The extinction corrections use an intrinsic (dust-free) Balmer decrement of $H\alpha/H\beta = 2.86$ for SF-dominated emission-lines (i.e., classified as HII-dominated on the BPT or VO87 diagrams) and $H\alpha/H\beta = 3.1$ for AGN emission (appropriate for narrow line region gas conditions, e.g., Osterbrock & Ferland 2006). Galaxies with observed Balmer decrements less than the assumed intrinsic decrements were assigned zero extinction.

We characterize basic galaxy properties using stellar mass, color, specific star formation rate (sSFR), and concentration. Stellar masses and specific star formation rates are estimated by Montero-Dorta et al. (in prep.), fitting the broad-band *ugriz* SDSS photometry with a grid of templates from the flexible stellar population synthesis code (FSPS, Conroy et al. 2009). The templates assume a Kroupa (2001) initial mass function, allowing a wide range of galaxy formation times $2 < t_{\text{age}}/\text{Gyr} < T_U(z)$, where T_U is the age of the universe at redshift z . The stellar mass and sSFR determination uses a broad-band fit for the dust attenuation (separate from the Balmer decrements used for dust-correcting the emission lines), following Charlot & Fall (2000) and Calzetti et al. (2000) by assuming τ_1 for birth clouds and τ_2 for old stars, with $\tau_1 = 3\tau_2$, and fitting a grid of values spanning $0 < \tau_2 < 0.75$. The use of broad-band photometry to estimate stellar mass and sSFR minimizes potential AGN contamination. Our study uses only narrow-line AGNs (not quasars), which generally have weak continuum emission. The AGN emission lines also do not significantly affect the broad-band photometry, since almost all AGNs in the sample have emission line equivalent widths $< 100\text{\AA}$.

All galaxy colors are k -corrected to $z = 0.05$ using the `kcorrect` IDL software (Blanton & Roweis 2007). We characterize galaxy morphology using a concentration parameter C_r defined as the ratio of the radii containing 90% and 50% of the galaxy’s r -band light, $C_r = R_{90,r}/R_{50,r}$. Details on the measurement of these Petrosian (1976) radii are given by Blanton et al. (2001). Galaxies with high concentration ($R_{90,r}/R_{50,r} \gtrsim 2.5$) tend to be bulge-dominated, while galaxies with $R_{90,r}/R_{50,r} \lesssim 2.5$ are typically disks.

It is important to note that the sample of galaxies with well-detected emission lines occupies a slightly different parameter space in galaxy properties compared to the full SDSS parent sample. In Figure 1 we compare the color-mass, sSFR-mass, and concentration-mass diagrams for the full parent sample with the well-measured BPT and VO87 samples. The restrictions on BPT and VO87 line ratios result in nearly identical well-measured samples, with fewer red, concentrated, and low-sSFR galaxies. Since the galaxies removed from the well-measured sample typically have $S/N_{\text{line}} < 3$, they tend to have weaker emission lines and so are significantly less likely to have AGNs. In Section 3.3 we devise a strategy that accounts for the small AGN fraction likely present in galaxies with poorly-measured line ratios.

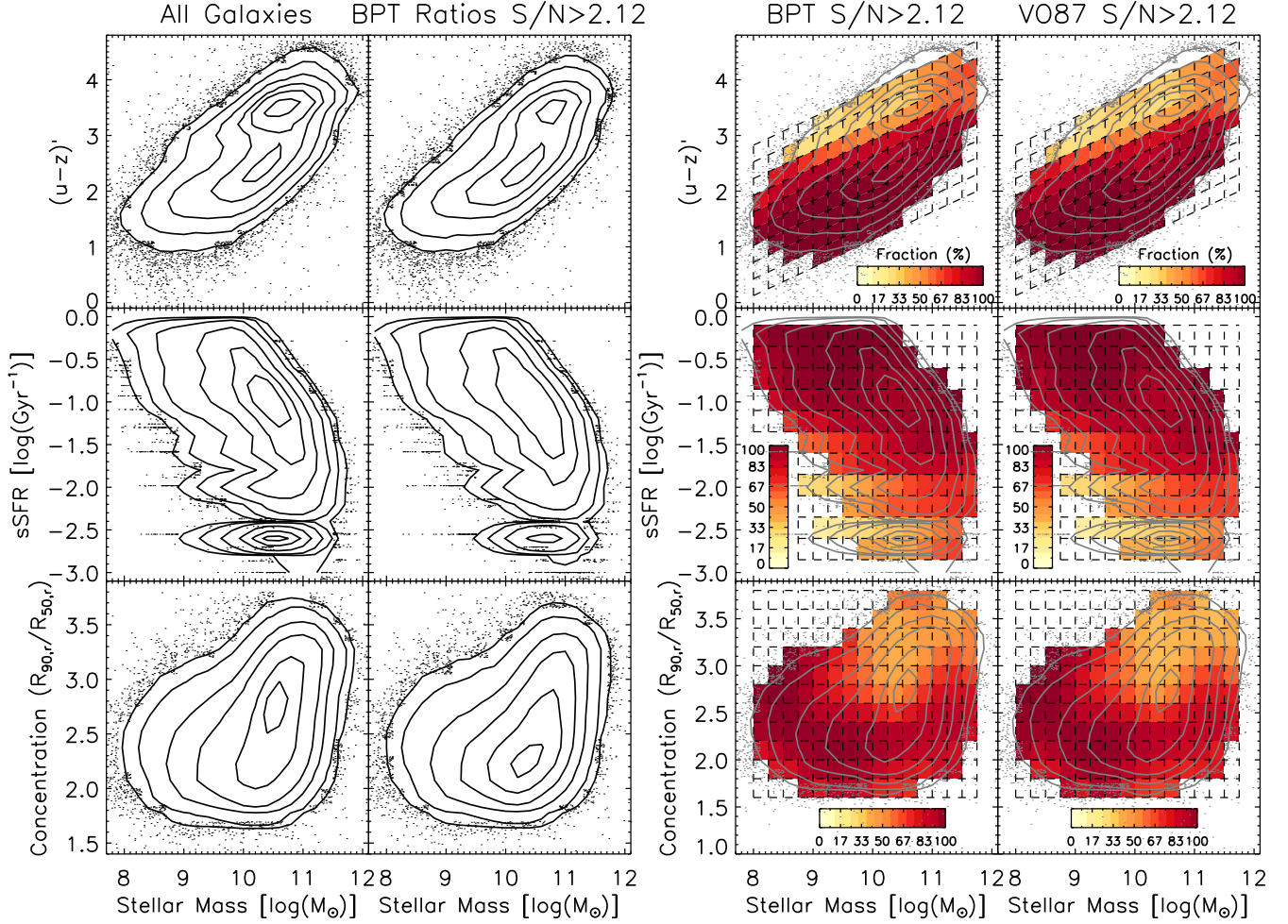


FIG. 1.— The distribution of galaxy properties for the full parent sample (left column, 317,192 galaxies) with the well-measured sample of galaxies having both BPT line ratios measured at $(S/N)_{\text{ratio}} > 3/\sqrt{2}$ (second column, 223,448 galaxies). The two columns at right also display the fraction of the full sample with well-measured $((S/N)_{\text{ratio}} > 3/\sqrt{2})$ BPT or VO87 line ratios. The emission-line ratio S/N requirements result in fewer red, low-sSFR, concentrated galaxies.

3. OBSERVED HOST PROPERTIES OF LINE-RATIO AGNS

We begin by examining the observed AGN fractions among host galaxies of different mass, color, SFR, and morphology. Section 3.1 introduces our adopted methods of line-ratio selection, including a method to separate AGNs and low-ionization narrow emission regions (LINERs). We use the well-measured sample in Section 3.2 to determine the fraction of BPT and VO87 AGNs with galaxy color, specific star formation rate, morphology, and stellar mass. In Section 3.3 we additionally provide a correction for the (small) fraction of AGNs missed among galaxies with poorly-measured line ratios, concluding with an estimate of the overall AGN fraction among the entire parent sample.

3.1. Line-Ratio AGN Selection

The most widely used methods for line-ratio classification of AGNs use the “BPT” (Baldwin et al. 1981) and “VO87” (Veilleux & Osterbrock 1987) diagrams. Each compares the ratios of forbidden lines of partially ionized metals with Balmer recombination lines of hydrogen: $[\text{O III}]\lambda 5007/\text{H}\beta$ vs $[\text{N II}]\lambda 6584/\text{H}\alpha$ for the BPT, and $[\text{O III}]\lambda 5007/\text{H}\beta$ vs $[\text{Si II}]\lambda(6717 + 6731)/\text{H}\alpha$ for the VO87

diagram. These lines are also typically among the brightest features in rest-frame optical spectra of galaxies, and the close wavelength range of each pair means that the ratios are largely insensitive to dust (assuming that forbidden metal lines and hydrogen recombination lines are emitted in the same galaxy regions). Note that BPT and VO87 classification is appropriate for use on narrow (i.e. <1000 km/s) emission lines only. Our sample does not include broad-line AGNs, which also exhibit broad (>1000 km/s) $\text{H}\alpha$ and $\text{H}\beta$ emission lines in their spectra.

Figure 2 presents our well-measured galaxy samples in the BPT and VO87 diagrams. Each galaxy in this sample has both of the relevant line ratios measured at $(S/N)_{\text{ratio}} > 3/\sqrt{2}$ (at left, $[\text{O III}]/\text{H}\beta$ and $[\text{N II}]/\text{H}\alpha$, and at right, $[\text{O III}]/\text{H}\beta$ and $[\text{Si II}]/\text{H}\alpha$). Also shown in Figure 2 are several demarcation lines for classifying galaxies:

1. BPT Kauffmann et al. (2003) empirical AGN/SF division line (long-dashed red),

$$\log([\text{O III}]/\text{H}\beta) = 1.3 + 0.61/[\log([\text{N II}]/\text{H}\alpha) - 0.05] \quad (1)$$

2. VO87 empirical AGN/SF division line defined for

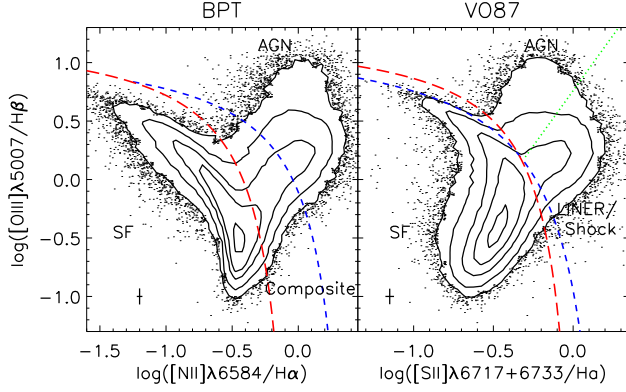


FIG. 2.— The BPT and VO87 diagrams for line-ratio classification of AGNs and star-forming galaxies. Median line ratio errors are shown by the error bars in the lower left of each panel. We adopt the long-dashed red lines for AGN/SF classification: in the BPT diagram this is the empirical line of Kauffmann et al. (2003), and in the VO87 diagram this is an empirical line of our own construction. Also shown in each diagram are the Kewley et al. (2001) maximal starburst lines (short-dashed blue), and the green dotted line in the VO87 diagram is the AGN/LINER division of Kewley et al. (2006).

this work (long-dashed red),

$$\log([OIII]/H\beta) = 1.3 + 0.48/[\log([SII]/H\alpha) - 0.10] \quad (2)$$

3. BPT Kewley et al. (2001) maximal starburst line (dashed blue),

$$\log([OIII]/H\beta) = 1.19 + 0.61/[\log([NII]/H\alpha) - 0.47] \quad (3)$$

4. VO87 Kewley et al. (2001) maximal starburst line (dashed blue),

$$\log([OIII]/H\beta) = 1.3 + 0.72/[\log([SII]/H\alpha) - 0.32] \quad (4)$$

5. VO87 Kewley et al. (2006) division between AGNs and LINERS (dotted green),

$$\log([OIII]/H\beta) = 0.76 + 1.89 \log([SII]/H\alpha) \quad (5)$$

We adopt Equations 1 and 2 as our lines for AGN/SF classification in this work, along with Equation 5 for AGN/LINER separation.

Accurate AGN selection lines are subject to considerable uncertainty, largely due to differences in interpretation. For example, the Kewley et al. (2001) lines (Equations 3 and 4) are the maximal line ratios for starbursts in photoionization models, and so can be treated as minimum AGN lines. Galaxies between the Kauffmann et al. (2003) and Kewley et al. (2001) lines (Equations 1 and 3) in the BPT diagram are often classified as “composite galaxies” with emission-line contribution from both SF and AGN. In general, composites have higher SFRs than AGN-dominated galaxies (Salim et al. 2007), and the two categories exhibit little difference in X-ray properties (Juneau et al. 2011; Trouille et al. 2011; Trump et al. 2011b). Therefore we assume that composite galaxies host similar AGNs but with more dilution from HII regions compare to galaxies with AGN-dominated line ratios. For this reason we include both composite and AGN-dominated galaxies lying above the Kauffmann et al. (2003) empirical AGN/SF line (Equation 1) in our initial BPT AGN selection.

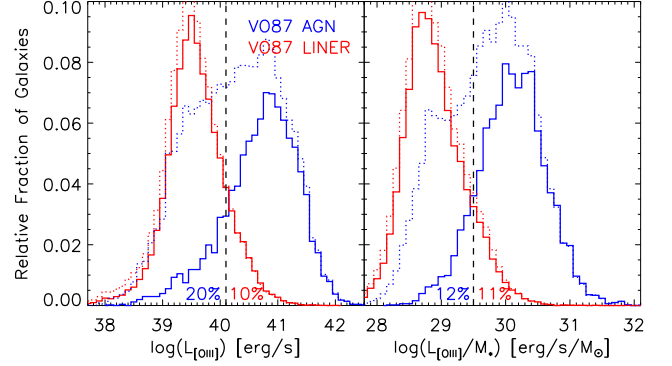


FIG. 3.— Distributions of dust-corrected $L[OIII]$ (left) and $L[OIII]/M_*$ (right) for AGNs and LINERS classified on the VO87 diagram. The dotted lines show all objects, while the solid lines show only “well-separated” AGNs and LINERS with line ratios at least 1σ from the AGN/LINER classification line (Equation 5). Vertical lines show empirical divisions between the two categories, with percentages of outliers indicated for the well-separated AGN (blue) and LINER (red) samples. The $L[OIII]/M_*$ ratio, a proxy for Eddington ratio, better distinguishes the two categories than $[OIII]$ luminosity alone, and we adopt this ratio to separate AGNs and LINERS identified by the BPT diagram.

We create a new empirical line in the VO87 diagram (Equation 2) which is designed to be parallel to the star-forming galaxy sequence in a similar fashion to the Kauffmann et al. (2003) empirical BPT line. In particular, our new VO87 line contrasts with the Kewley et al. (2001) maximal starburst line in the treatment of low-metallicity galaxies (the upper left in each panel of Figure 2). Equation 4 selects several AGNs from the symmetric tail of the low-metallicity star-forming galaxy sequence, while our Equation 2 avoids classifying these galaxies as AGNs.

In the VO87 diagram, the Kewley et al. (2006) line (Equation 5) additionally separates AGNs from low-ionization narrow emission-line regions (LINERS, Heckman 1980). X-ray and radio observations suggest that LINER galaxies are likely to host nuclear AGNs (Ho 2008, and references therein). However LINERS have much lower accretion rates than stronger-lined AGNs (Ho 2009) and much of their line emission is probably powered by extended ionization sources rather than nuclear activity (Yan & Blanton 2012). For these reasons we avoid LINERS in our sample and define “VO87 AGNs” as lying above the new empirical AGN/SF line (Equation 2) and the Kewley et al. (2006) AGN/LINER line (Equation 5) in the VO87 diagram.

Unlike the “VO87 AGN” category, the BPT diagram does not distinguish between AGNs and LINERS. Indeed, the BPT diagram does not lend itself to a similar LINER/AGN separation as the Kewley et al. (2006) line in the VO87 diagram: while the $[SII]$ critical density relates to the LINER/AGN transition, the $[NII]$ critical density is a factor of ~ 30 higher and does not. (Veilleux & Osterbrock (1987) originally suggested a simple AGN/LINER separation of $[OIII]/H\beta > 3$, but AGNs and LINERS form a continuous rather than bimodal distribution in $[OIII]/H\beta$, e.g. Ho et al. 2003.)

AGNs typically have stronger emission lines than LINERS, and so we investigate the use of $[OIII]$ luminosity and the ratio $L[OIII]/M_*$ to separate the two classes in Figure 3. The $L[OIII]/M_*$ ratio is related to the Edding-

ton ratio $L_{\text{bol}}/L_{\text{Edd}}$: for a bolometric correction $k_{[\text{OIII}]}$ = $L_{\text{bol}}/L_{[\text{OIII}]}$ (the inverse of the fraction of total AGN light reprocessed as $[\text{OIII}]$ emission) and a mass ratio $\gamma = M_{\text{BH}}/M_*$, $L_{[\text{OIII}]} / M_* = \frac{\gamma}{k_{[\text{OIII}]}} \frac{L_{\text{bol}}}{1.3 \times 10^{38} M_{\text{BH}}}$. (The variables $k_{[\text{OIII}]}$ and γ are not actually constants: more accurate relationships between $L_{[\text{OIII}]} / M_*$ and Eddington ratio are discussed in Section 5. However $\log(L_{[\text{OIII}]} / M_*)$ does monotonically increase with $\log(L_{\text{bol}} / L_{\text{Edd}})$ with a nearly linear slope of ~ 0.5 , making it a useful simple proxy.)

Figure 3 compares $L_{[\text{OIII}]}$ and $L_{[\text{OIII}]} / M_*$ of “well-separated” AGNs and LINERs with measured line ratios at least 1σ from the AGN/LINER classification line. The left panel shows a significant tail of low-luminosity VO87 AGNs overlapping with the LINERs. This overlap is reduced when the two populations are instead compared in $L_{[\text{OIII}]} / M_*$. In the right panel of Figure 3, AGNs and LINERs with line ratios well-separated from the classification line are divided by:

$$\log(L_{[\text{OIII}]} / M_*) \geq 29.5 \text{ [log(erg s}^{-1} M_{\odot}^{-1})] \quad (6)$$

Due to both the physical motivation and the good empirical separation, we use Equation 6 to define a “BPT AGN” category which is mostly free of LINERs.

In summary, we identify two categories of AGNs using emission-line properties:

- BPT AGN: Above the Kauffmann et al. (2003) line $\log([\text{OIII}]/\text{H}\beta) > 1.3 + 0.61/[\log([\text{NII}]/\text{H}\alpha) - 0.05]$, and with $\log(L_{[\text{OIII}]} / M_*) \geq 29.5$ (units of erg s^{-1} and M_{\odot}): Equations 1 and 6.
- VO87 AGN: Above our empirical AGN/SF line and the Kewley et al. (2006) AGN/LINER division, $\log([\text{OIII}]/\text{H}\beta) > 1.3 + 0.48/[\log([\text{SII}]/\text{H}\alpha) - 0.10]$ and $\log([\text{OIII}]/\text{H}\beta) > 0.76 + 1.89 \log([\text{SII}]/\text{H}\alpha)$: Equations 2 and 5.

Among each well-measured sample, 6.3% (14,175/223,448) of galaxies are classified as BPT AGNs and 4.3% (9210/215,242) are classified as VO87 AGNs. In the next section we demonstrate that both methods identify AGNs in similar kinds of galaxies, and the lower AGN fraction identified by the VO87 is due to slightly lower overall selection efficiency.

3.2. Observed AGN Fractions in Well-Measured Galaxies

Figure 4 shows the observed BPT and VO87 AGN fractions in bins of galaxy color, specific star formation rate, and concentration versus stellar mass among galaxies of the well-measured sample. The AGN fraction is defined as the fraction of galaxies (with line ratio $(S/N)_{\text{ratio}} > 3/\sqrt{2}$) in each bin that meet the criteria of the BPT AGN or VO87 AGN categories defined in Section 3.1, and bins with less than 50 galaxies are left blank. In both the BPT and VO87 diagrams, the AGN fraction is observed to be highest in massive ($M_* \sim 10^{10.5} M_{\odot}$), green, moderate-sSFR, bulge-dominated galaxies with $R_{90,r}/R_{50,r} > 2.5$. There is also a small population of VO87 AGNs in low-mass hosts which are not identified by the BPT AGN classification. We demonstrate in Section 5 that this result may be due to a bias of the BPT

against AGNs with low-metallicity NLRs which remain detected in the VO87 diagram.

The maximal AGN fraction in massive green, moderate-sSFR, bulge-dominated galaxies led to previous conclusions that AGN require massive host galaxies and cause feedback that quenches star formation (e.g., Kauffmann et al. 2003; Schawinski et al. 2010). Xue et al. (2010) demonstrated that the similar massive green-valley host preference observed for X-ray AGNs is caused solely by selection effects, and Aird et al. (2012) additionally showed that the intrinsic AGN distribution is actually uniform at all stellar masses. In Sections 4 and 5 we similarly investigate the selection biases affecting line-ratio selection and demonstrate that the intrinsic AGN occupation fraction differs from the the simplest interpretation of the observations, especially for low-mass galaxies.

As discussed in Section 2 and shown in Figure 1, the well-measured galaxy samples (with line ratio $(S/N)_{\text{ratio}} > 3/\sqrt{2}$) include fewer massive, red, concentrated, and low-sSFR galaxies than the parent population. In the next subsection we account for AGNs in poorly-measured galaxies, showing that the green-valley (moderate-sSFR, concentrated) AGN preference is even more apparent among the full parent sample of galaxies.

3.3. The Line-Ratio AGN Fraction Among All Galaxies

It is only possible to select line-ratio AGNs in galaxies with well-measured emission-line ratios. However Figure 1 demonstrates that the well-measured galaxy sample results in a biased set of galaxy properties. Measuring an unbiased AGN fraction requires understanding the likely AGN occupation among galaxies with poorly-measured $(S/N < 3/\sqrt{2})$ emission-line ratios.

In Section 3.1 we demonstrated that the VO87 AGN classification (Equations 2 and 5) tends to select AGNs with $L_{[\text{OIII}]} / M_* > 29.5$ (units of erg s^{-1} and M_{\odot}), and we impose the same limit to select non-LINER BPT AGNs (Equation 6). Figure 5 presents the $L_{[\text{OIII}]} / M_*$ distributions for galaxies with both poorly-measured (black) and well-detected emission-line ratios (gray), alongside the AGN fraction (red) measured from the well-detected galaxy sample. Some of the $[\text{OIII}]$ measurements for poorly-measured galaxies are likely to have large error bars, especially at the lowest $L_{[\text{OIII}]} / M_*$ ratios. Still, it is clear that most galaxies with poorly-measured line ratios typically have $\log(L_{[\text{OIII}]} / M_*) < 29.5$, suggesting that they are unlikely to host AGNs. There is only a small tail of poorly-measured galaxies with $\log(L_{[\text{OIII}]} / M_*) > 29.5$ which might have a significant number of “missed” AGNs.

We account for the potentially missed AGNs by assuming that poorly-measured galaxies have the same AGN fraction as a function of $L_{[\text{OIII}]} / M_*$ as observed in the well-measured galaxies, in each bin of galaxy properties. Since poorly-measured galaxies have lower typical $L_{[\text{OIII}]} / M_*$ than well-measured galaxies, bins with significant numbers of missed galaxies (i.e., high-mass, red, high-sSFR, and concentrated galaxies) are likely to have lower AGN fractions than those presented in Section 3.2 and Figure 4 for the well-measured galaxy sample.

Figure 6 presents the total BPT and VO87 AGN fractions for the entire parent sample of 317,192 galaxies.

Observed AGN Fractions (Well-Measured Galaxies)

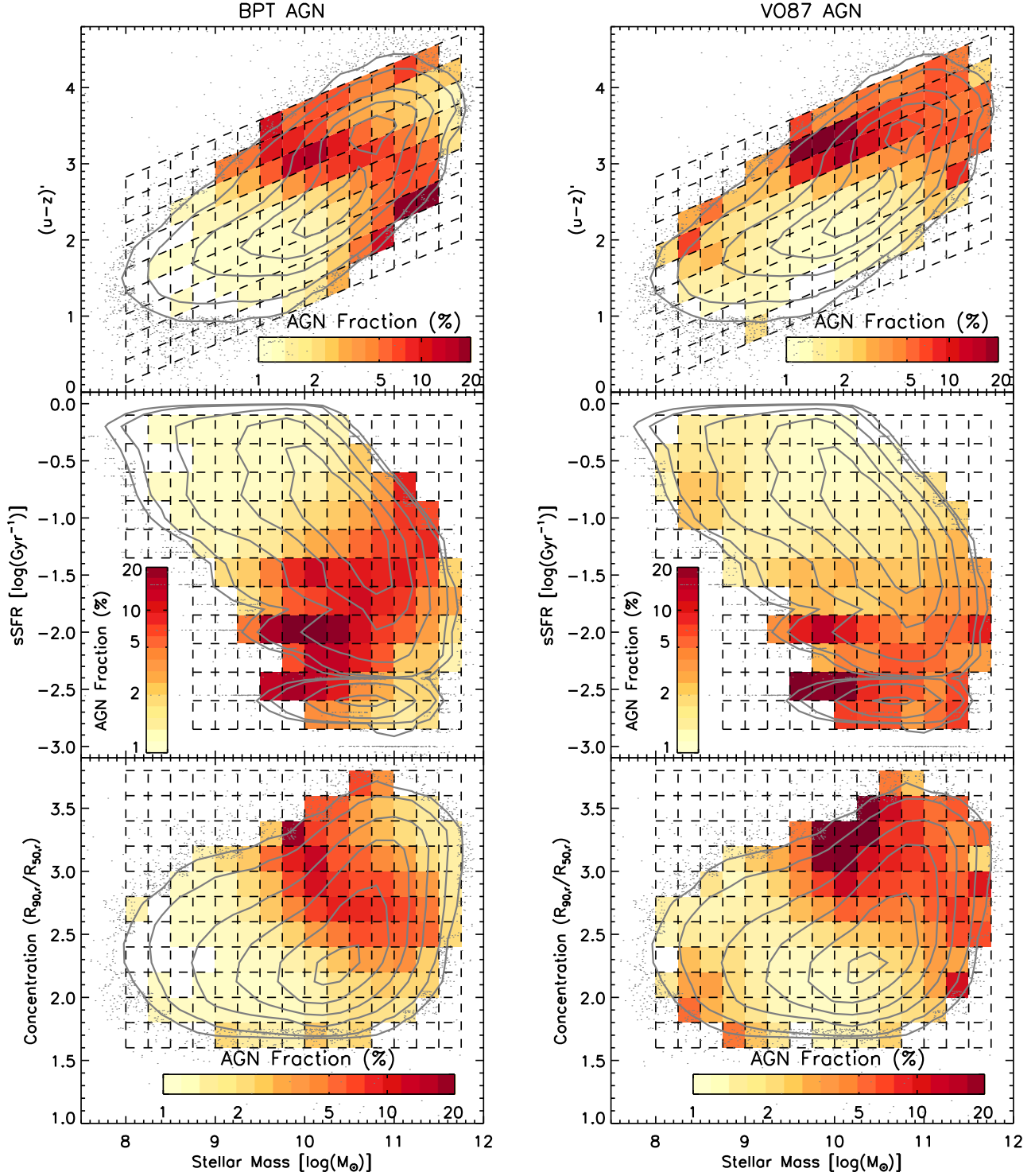


FIG. 4.— The observed fractions of BPT AGNs and VO87 AGNs among galaxies in the well-measured samples (with $(S/N)_{\text{ratio}} > 3/\sqrt{2}$), in bins of galaxy color, specific star formation rate, and concentration versus stellar mass. Color is k-corrected to be observed at $z = 0.05$ and color-mass bins are tilted (with a slope of 0.5) to match the slope of the blue cloud. Bins with less than 50 galaxies are left blank (white). Gray contours represent the overall population of well-measured galaxies. The observed (non-LINER) AGN fraction is highest in massive green, moderate-sSFR, and concentrated galaxies and lower on both the low-mass and red (low-sSFR) extremes of the galaxy population.

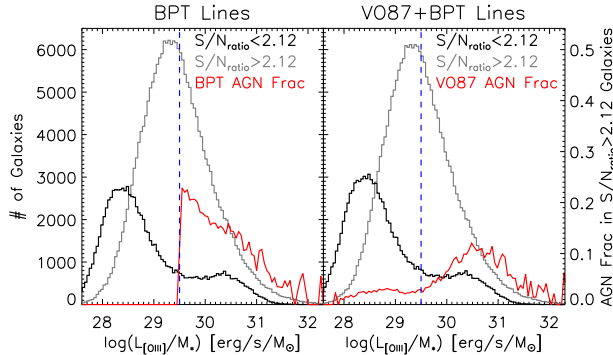


FIG. 5.— The distributions of dust-corrected $L[\text{OIII}]/M_*$ for weak-lined ($S/N_{\text{ratio}} < 3/\sqrt{2}$) galaxies compared to the AGN fraction as a function of $L[\text{OIII}]/M_*$ measured from strong-lined ($S/N_{\text{ratio}} > 3/\sqrt{2}$) galaxies. The dashed line shows the $L[\text{OIII}]/M_* > 29.5$ empirical limit for AGN selection. Most poorly-measured galaxies have $L[\text{OIII}]/M_* < 29.5$ and so are typically less likely to host AGNs than well-measured galaxies.

In each bin, we begin with the measured AGN fraction among well-measured galaxies, then add a correction by assuming the same AGN fraction as a function of $L[\text{OIII}]/M_*$ in the poorly-measured galaxies. These corrections are only significant (with $>25\%$ as many “missed” AGNs as well-measured AGNs) in high-mass red, low-sSFR, and concentrated galaxies, and the correction in these galaxies results in a smaller AGN fraction than found in the well-measured sample. The lack of non-LINER AGNs among massive quenched galaxies agrees with previous AGN host studies for line-ratio AGNs (Kauffmann et al. 2003; Heckman et al. 2004; Kauffmann & Heckman 2009; Schawinski et al. 2010; Tanaka 2012), broad-line AGNs (Trump et al. 2013a; Matsuoka et al. 2014), and X-ray AGNs (Mullaney et al. 2012; Harrison et al. 2012; Rosario et al. 2013a,b; Chen et al. 2013; Azadi et al. 2015). Otherwise the estimated total BPT and VO87 AGN fractions are very similar to the well-measured AGN fractions (Figure 4), and the correction for poorly-detected galaxies leads to a qualitatively identical preference for AGNs to be observed in massive green-valley (moderate-sSFR, bulge-dominated) galaxies.

4. BIASES OF LINE-RATIO CLASSIFICATION

The AGN line-ratio signature can be hidden by HII region line ratios in galaxies with a significant level of star formation. Below we investigate how this “star formation dilution” changes with galaxy properties and influences the observed AGN fractions. We begin by computing basic AGN detection limits, quantified by $L[\text{OIII}]_{\text{AGN}}/M_*$, for galaxies to host BPT and VO87 AGNs. These detection limits implicitly account for the changing spectroscopic aperture by using observed HII region emission within the same aperture, although we also directly investigate aperture effects by comparing the observed AGN fractions in different redshift bins. Finally, we compute the intrinsic AGN fractions across host galaxy properties using Monte Carlo simulations of physically-motivated distributions of Eddington ratio and black hole / galaxy mass ratios.

4.1. Basic Limits for AGN Detection

The biases of BPT and VO87 AGN selection can be characterized by estimating the threshold at which AGN emission exceeds star formation dilution within a $3''$ fiber for galaxies of different properties. We quantify this threshold using the intrinsic (dust-free) $[\text{OIII}]$ luminosity of the AGN divided by the galaxy stellar mass: $L[\text{OIII}]_{\text{AGN}}/M_*$. This quantity is related to the Eddington ratio $L_{\text{bol}}/L_{\text{Edd}}$ by a $[\text{OIII}]$ bolometric correction and the mass ratio M_{BH}/M_* . For now, we simply assume that $L[\text{OIII}]_{\text{AGN}}/M_*$ is monotonically related to $L_{\text{bol}}/L_{\text{Edd}}$, reserving a detailed discussion of the functional form until Section 5.

We estimate the changes in star formation dilution with galaxy properties using the typical HII region line strengths in the bins of the various panels in Figure 4. That is, for each bin in color-mass, sSFR-mass, and concentration-mass, we calculate the median dust-corrected (assuming an intrinsic $\text{H}\alpha/\text{H}\beta = 2.86$) luminosity of each emission line for galaxies with line ratios classified as star-forming in the BPT or VO87 diagrams. The typical HII region emission depends both on spectroscopic aperture and galaxy properties, and we implicitly account for both by using the observed line fluxes of SF galaxies in each bin. The AGN detection limit is given by the AGN contribution needed to push these line ratios onto the AGN/SF diagnostic lines: Kauffmann et al. (2003) on the BPT (Equation 1), or our empirical line on the VO87 (Equation 2). For the moment we neglect the AGN/LINER divisions (Equations 5 and 6), although we include these requirements in our detailed models of AGN selection biases in Section 5. We assume a “pure AGN NLR” has $\log([\text{OIII}]/\text{H}\beta) = 0.5$, $\log([\text{NII}]/\text{H}\alpha) = 0.0$, and $\text{H}\alpha/\text{H}\beta = 3.1$. Because we are starting from dust-corrected HII region emission lines, the derived AGN detection limits are similarly dust-free, assuming that both NLR and HII region gas have the same dust extinction. We demonstrate that this assumption is valid in the Appendix. Using dust-free $L[\text{OIII}]_{\text{AGN}}/M_*$ makes it easier to relate to an Eddington ratio, although it does mean that our detection limits are not strictly observed quantities.

Our method of computing AGN detection limits is illustrated by Figure 7, which shows the line ratios and strengths (in L_{line}/M_*) for two bins in galaxy color-mass. Low-mass blue galaxies have higher L_{line}/M_* from integrated HII regions than high-mass red galaxies. Thus low-mass blue galaxies (which also tend to have high-sSFR and low-concentration) require an AGN with higher $L[\text{OIII}]_{\text{AGN}}/M_*$ to be classified as a BPT or VO87 AGN compared to massive red (low-sSFR, high-concentration) galaxies.

The $L[\text{OIII}]_{\text{AGN}}/M_*$ detection limits for an AGN to exceed the star formation dilution are shown in bins of color-mass, sSFR-mass, and concentration-mass in Figure 8. At a basic level the detection limits mirror the observed AGN fractions: the bins of lowest AGN fraction (low-mass, blue, high-sSFR, low-concentration) tend to also have the highest AGN detection thresholds. If we assume $\gamma = M_{\text{BH}}/M_* \sim 0.001$ (Häring & Rix 2004, assuming $M_* \sim 1.5M_{\text{bulge}}$) and $k_{[\text{OIII}]} \sim 100$ (Lamastra et al. 2009, for $\log(L[\text{OIII}]_{\text{AGN}}) \sim 40$), then the $L[\text{OIII}]_{\text{AGN}}/M_*$ limits translate to $\log(L_{\text{bol}}/L_{\text{Edd}}) \sim -2$ for blue low-mass (high-sSFR, mixed-concentration)

Line Ratio AGN Fractions (All Galaxies)

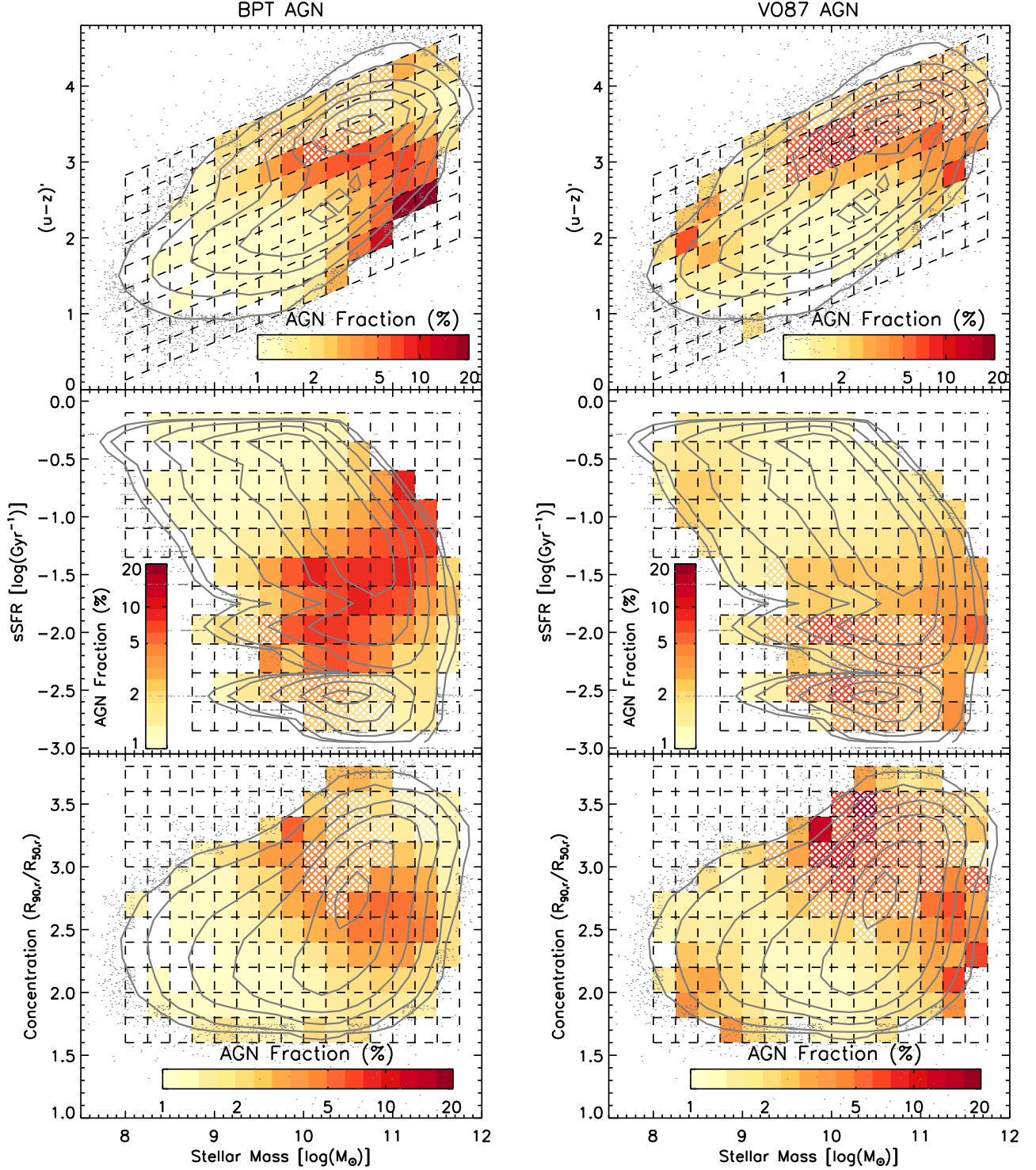


FIG. 6.— Total fractions of observed BPT and VO87 AGNs estimated for the entire parent sample of 317,192 galaxies, in bins of galaxy color (k -corrected $u - z$), specific star formation rate, and concentration ($R_{90,r}/R_{50,r}$) versus stellar mass. The AGN fractions are determined from the well-measured sample with a correction for the AGNs missed among galaxies with poorly-detected lines, assuming the same AGN fraction with $L[\text{OIII}]/M_*$ as outlined in Section 3.3. Gray contours show the overall galaxy population from the full parent sample. Bins where the correction is $>25\%$ of the total AGN fraction are marked with crossed hashes: this only occurs among massive, red, low-sSFR, concentrated galaxies. The corrected AGN fractions are very similar to the well-measured AGN fractions in Figure 4. The observed BPT and VO87 AGN fractions are highest among massive green-valley hosts, with lower AGN fractions for both massive red (low-sSFR, concentrated) and low-mass blue (high-sSFR, low-concentration) galaxies.

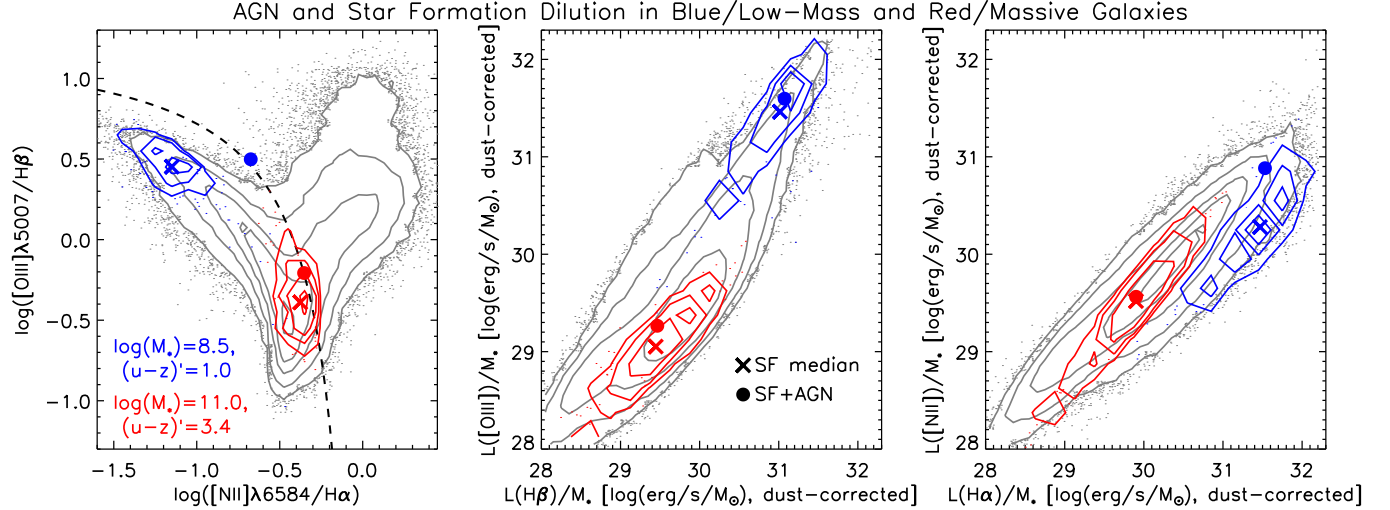


FIG. 7.— An illustration of star formation dilution and AGN detectability for galaxies with different properties. The contours show the line ratios and strengths of BPT-classified star-forming galaxies: in blue, low-mass blue galaxies with $8.5 < \log(M_*/M_\odot) < 8.75$ and $-3.275 < (u-z)' - 0.5 \log(M_*/M_\odot) \leq -2.975$; in red, high-mass red galaxies with $11 < \log(M_*/M_\odot) < 11.25$ and $-2.075 < (u-z)' - 0.5 \log(M_*/M_\odot) \leq -1.775$; and in gray, all galaxies with $(S/N)_{\text{ratio}} > 3/\sqrt{2}$. Crosses represent the median values of the star-forming galaxies, and filled circles indicate the combined ratios after adding enough “pure AGN NLR” emission to reach the Kauffmann et al. (2003) AGN/SF division line. There is more star formation dilution in low-mass blue (high-sSFR, low-concentration) galaxies, requiring a relatively more powerful AGN to be selected as a BPT AGN.

galaxies and $\log(L_{\text{bol}}/L_{\text{Edd}}) \sim -5$ for red high-mass (low-sSFR, high-concentration) galaxies. Since the AGN Eddington ratio distribution is steeply declining (e.g., Kauffmann & Heckman 2009; Aird et al. 2012; Hickox et al. 2014), this behavior leads to a significantly lower observed AGN fraction in low-mass galaxies. We use more detailed models of Eddington ratio, bolometric correction, and M_{BH}/M_* to investigate the AGN selection biases in Section 5 below.

Interpreting the biases of BPT and VO87 AGN selection crucially depends on the metric used to estimate AGN power. Kauffmann et al. (2003) (and later, Schawinski et al. 2010) used $L[\text{OIII}]$ as an indicator of AGN strength, concluding that “powerful” ($L[\text{OIII}] > 10^7 L_\odot$) AGNs are present only in high-mass galaxies. These luminous AGNs make up the bulk of the total cosmic accretion history of AGNs, since mass accretion rate \dot{M}_{BH} is related to $L[\text{OIII}]$ by a bolometric correction $k_{[\text{OIII}]}$ and an efficiency η , $\dot{M}_{\text{BH}} = k_{[\text{OIII}]} L[\text{OIII}] / (\eta c^2)$. However, the Eddington ratio $L_{\text{bol}}/L_{\text{Edd}}$ is a more effective indicator of AGN accretion structure and wind/jet outflow properties (e.g., Narayan & McClintock 2008; Ho 2008; Trump et al. 2011a; Heckman & Best 2014). In this sense, our Eddington ratio proxy $L[\text{OIII}]/M_*$ is an effective way to quantify how line-ratio selection biases relate to AGN-galaxy coevolution.

The “pure AGN NLR” line ratios assumed here are estimated from the locus of AGN-dominated galaxies on the BPT diagram. Figure 4 demonstrates that AGN-dominated line ratios are most often seen in massive hosts. Massive galaxies also tend to have high (near-solar) metallicities, which means that the pure AGN NLR line ratios are appropriate only for metal-rich NLR emission. In the Appendix we demonstrate that the observed line-ratio AGN occupation fractions are better described by the presence of low-metallicity AGN NLRs in low-metallicity galaxies. This effect further worsens the AGN detection bias in low-mass galaxies beyond that

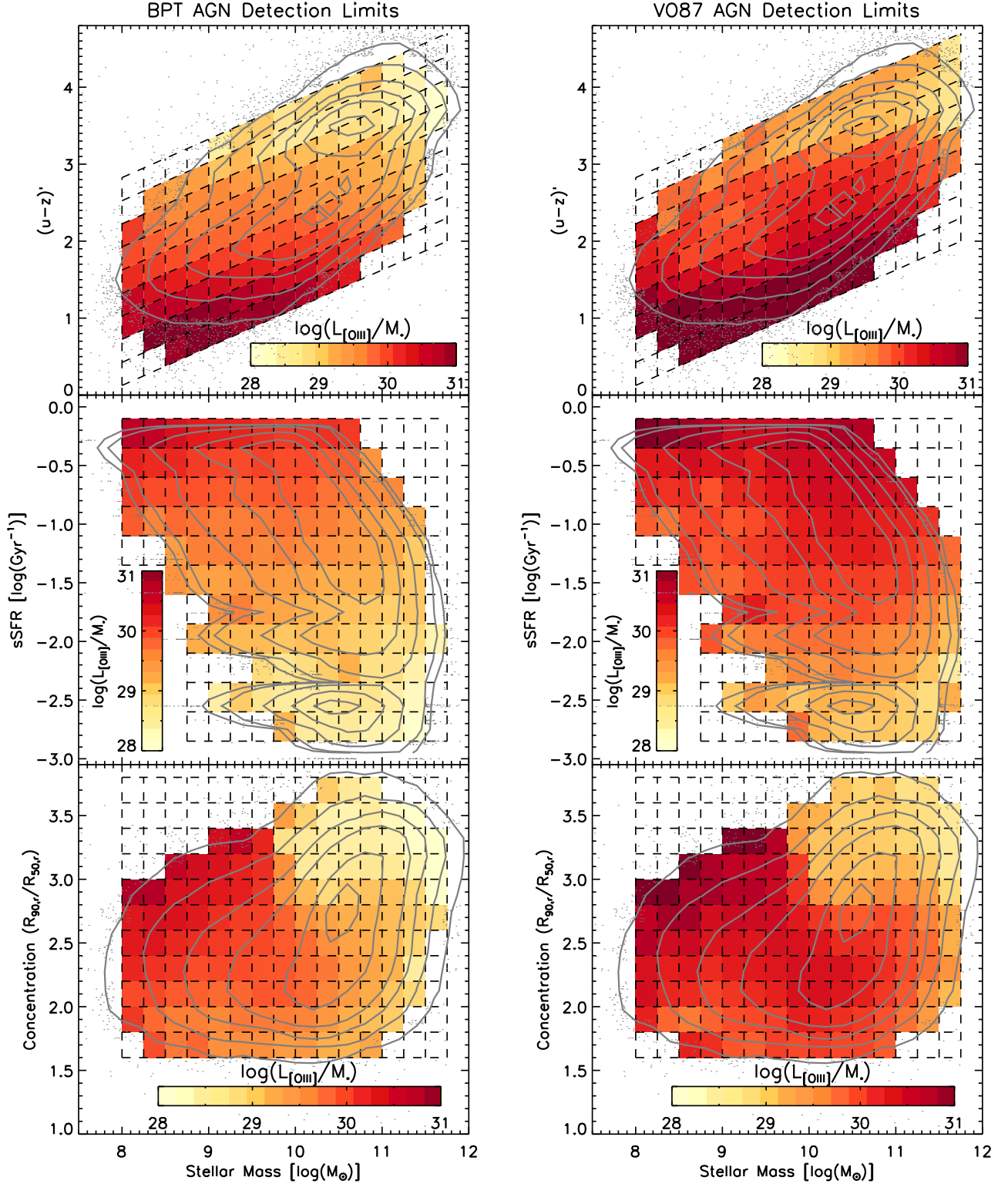
already present in Figure 8.

4.2. Aperture Effects on AGN Detection

The size of the spectroscopic aperture affects the amount of star formation dilution in the observed emission-line ratios. Smaller apertures include less star formation relative to the nuclear AGN: for example, Moran et al. (2002) demonstrated that many nearby narrow-line AGNs are hidden by star formation dilution in larger spectroscopic apertures. Our objects were all observed in $3''$ fibers with the SDSS spectrograph. Figure 9 demonstrates that the $3''$ aperture covers a different fraction of the galaxy light at different redshifts and different galaxy sizes. The median ratio of fiber radius to r -band half-light radius, $R_{\text{fiber}}/R_{50,r}$, ranges from ~ 0.3 to ~ 0.6 (and 1σ bounds extending to ~ 0.2 and ~ 0.8). The fractional aperture changes are smaller than the changes in absolute aperture size because low-mass galaxies, which are smaller in physical size, are only observed at low redshift, corresponding to smaller physical aperture sizes. Larger high-mass galaxies are mostly in the higher-redshift volume and consequently have larger physical aperture sizes. These r -band half-light radii are not necessarily equivalent to the emission-line half-light radii, but Figure 9 remains a useful demonstration of the changes in aperture effects with redshift.

The lack of aperture effects with redshift is similarly seen in Figure 10, which compares observed fractions of galaxies classified as BPT AGN and VO87 AGN at $0.01 < z < 0.03$, $0.04 < z < 0.06$, and $0.08 < z < 0.1$. The “break” from high to low AGN fraction is at $\log(M_*) \sim 10$ in all three redshift bins. As seen in Figure 9, there are no significant aperture effects causing differential star formation dilution and AGN identification as a function of stellar mass.

It should be emphasized again that both the AGN limits from Section 4.1 and the Monte Carlo simulations of Section 5 implicitly account for aperture effects. We



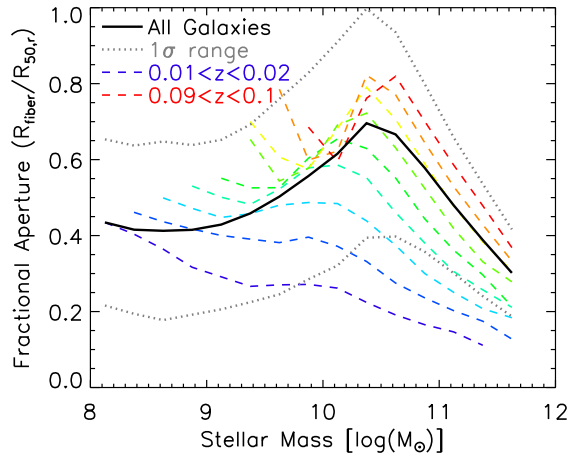


FIG. 9.— The fractional aperture covered by the SDSS fiber, quantified as the ratio between fiber radius and r -band half-light radius, with stellar mass. The thick black line shows the median aperture coverage for all galaxies, and the gray dotted lines represent the 1σ range at each stellar mass. The dashed lines display the median fractional aperture in redshift bins of width $\Delta z = 0.01$ (i.e., 9 bins from $0.01 < z < 0.02$ to $0.09 < z < 0.10$). Although there are significant aperture changes with redshift, the average fractional aperture for the whole sample changes by less than a factor of two with stellar mass.

empirically quantify star formation dilution using line fluxes of HII regions only within the spectroscopic aperture, rather than total-galaxy measurements. Thus even if there were aperture effects missed by Figures 9 and 10, they would be accounted for in our models of AGN limits and in the resultant intrinsic AGN fraction with host properties.

5. MODELING THE INTRINSIC AGN POPULATION

In Section 4 we demonstrated that line-ratio AGN selection is biased against host galaxies with low stellar mass, blue color, and high sSFR. Such galaxies have more “star formation dilution” from optical emission lines produced in HII regions. But it remains unclear if the absence of observed AGNs in low-mass blue disk hosts is caused purely by bias, or there is also some change in AGN occupation with galaxy properties.

In this Section we directly model the intrinsic AGN population as a function of galaxy properties. Separate simulations are run for both the BPT and VO87 AGN selection methods, comparing the modeled and observed fraction of galaxies meeting each set of AGN selection criteria. Within each bin of galaxy properties (color–mass, sSFR–mass, or concentration–mass), the simulations follow these basic steps:

1. A set of “non-AGN” line ratios is randomly drawn (with replacement) from the dust-corrected lines of observed galaxies with well-measured line ratios not classified as BPT AGNs or VO87 AGNs. We require that these galaxies be face-on ($b/a > 0.5$) and remove outliers in velocity dispersion (using iterative 2σ clipping). The number of simulated galaxies is the same as the total number of galaxies within each bin.
2. Each simulated “non-AGN” galaxy is assigned an AGN with an Eddington ratio $L_{\text{bol}}/L_{\text{Edd}}$ randomly

drawn from a probability distribution. The average Eddington ratio is either fixed or allowed to vary as a free parameter.

3. The Eddington ratio is translated to AGN emission-line luminosities in three steps. First, black hole mass is estimated from galaxy velocity dispersion (or allowed to be a free parameter). [OIII] luminosity is then derived from L_{bol} using a (luminosity-dependent) bolometric correction. From $L[\text{OIII}]_{\text{AGN}}$, we then compute the other line luminosities assuming “pure AGN NLR” line ratios.
4. We compute the number of simulated galaxies with resultant AGN+galaxy line luminosities classified as BPT AGNs (Equations 1 and 6) or VO87 AGNs (Equations 2 and 5). The simulated AGN fraction is given by the median from 200 Monte Carlo simulations of steps 1–3 above, with an associated error given by the normalized median absolute deviation (NMAD).

The assumptions inherent in these steps are motivated and discussed in Section 5.1, with detailed tests of the assumptions also given in the Appendix. Inspired by the work of Aird et al. (2012) for X-ray AGN hosts, in Section 5.2 we test if the observed AGN fractions are consistent with uniform SMBH growth regardless of host properties. In Sections 5.3 and 5.4, respectively, we instead fit the Eddington ratio and black hole mass as free parameters, demonstrating that AGN accretion is correlated with galaxy sSFR and low-mass galaxies may have undermassive black holes.

5.1. Basic Modeling Assumptions

In each bin of galaxy properties, initial sets of “non-AGN” line ratios are empirically drawn from well-measured ($(S/N)_{\text{ratio}} > 3/\sqrt{2}$) galaxies that have reliable velocity dispersions (described below) and do not meet the BPT or VO87 AGN selection criteria. The empirical sets of galaxies implicitly reflect the distribution of non-AGN line ratios in each bin of galaxy properties. The breadth of the line-ratio distribution comes from the scatter in the mass-metallicity relation (e.g., Tremonti et al. 2004), a range of ionization conditions from HII regions and old star winds (e.g., Sánchez et al. 2015), and fiber aperture effects for different galaxy sizes and redshifts. Beginning the simulations with empirical non-AGN line ratios accurately reproduces the observed line-ratio distributions (see Section 5.5). Since we do not classify LINERs as BPT or VO87 AGNs, they are included in the “non-AGN” galaxy sets. LINER galaxies are likely to host weakly accreting AGNs (e.g., Ho 2008, 2009), but Yan & Blanton (2012) demonstrated that the bulk of their emission-line flux is extended rather than due to a nuclear AGN. Thus we include LINERs among the empirically-drawn “non-AGN” line ratios, simulating the addition of more powerful AGNs with Seyfert-like line ratios to such galaxies.

Because the simulations begin with empirical line ratios of non-AGN galaxies, they cannot predict the AGN fraction in poorly-measured galaxies (which, by definition, cannot be reliably classified as star-forming

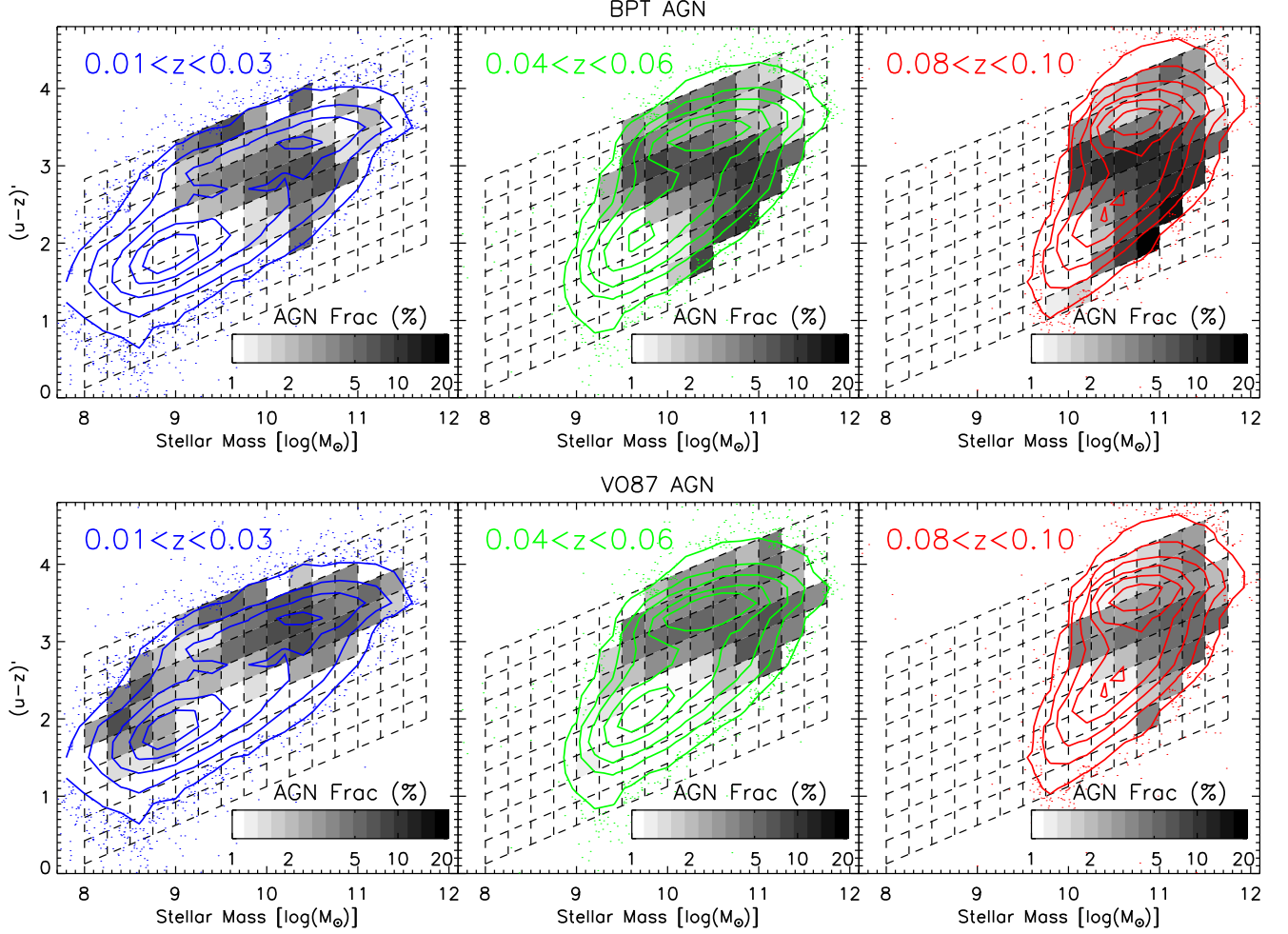


FIG. 10.— The fraction of galaxies classified as BPT AGN and VO87 AGN in three bins of redshift, from low to high. Gray contours show the distribution of galaxies in each redshift bin. Where galaxies are present in multiple redshift bins, there is little difference in the observed AGN fraction, suggesting that AGN selection is minimally affected by the changing aperture. Essentially the increase in galaxy size with stellar mass is balanced by a corresponding increase in the typical physical aperture size, since low-mass galaxies are observed only at low redshift and high-mass galaxies are mostly at high redshift.

or AGN). For this reason we only compare (or fit) the simulations to the observed AGN fractions among well-measured galaxies. The inability to simulate poorly-measured line ratios has consequences for massive red (low-sSFR, concentrated) galaxies, which tend to be excluded in the well-measured sample. We investigate this issue in Section 5.3 by assuming that poorly-measured galaxies have the same median ratio of $L_{\text{bol}}/L_{\text{Edd}}/(L[\text{OIII}]_{\text{total}}/M_*)$ as the well-measured galaxies.

The Eddington ratio distribution of our simulated AGNs is parameterized as a Schechter function, following Hopkins & Hernquist (2009):

$$P(\lambda) = \frac{dt}{d \log \lambda} = P_0 \left(\frac{\lambda}{\lambda_*} \right)^{-\alpha} \exp \left(-\frac{\lambda}{\lambda_*} \right). \quad (7)$$

This functional form is effectively a power-law distribution, with a “turnover” Eddington ratio of $\lambda_* = 0.4$ set to impose the Eddington limit $\lambda < 1$. The Eddington ratio $\lambda \equiv L_{\text{bol}}/L_{\text{Edd}}$, with $L_{\text{Edd}} \simeq 1.3 \times 10^{38} (M_{\text{BH}}/M_{\odot}) \text{ erg s}^{-1}$, and P_0 is a normalization constant. Equation 7 is, at best, an approximation for the true Eddington ratio distribution, which is poorly

known and not well-constrained by observations (e.g., Kelly et al. 2010). However, adopting a functional form allows us to effectively compare *relative* Eddington ratios across galaxy properties.

We use $\alpha = 0.6$ for the power-law slope of Equation 7, consistent with the observed Eddington ratio distribution (Hopkins & Hernquist 2009; Kauffmann & Heckman 2009) and similar to the distribution used by Aird et al. (2012). In the Appendix we demonstrate that shallower Eddington ratio distributions (e.g., $\alpha = 0.2$ from Hickox et al. 2014 or $\alpha = 0.05$ from Schulze & Wisotzki 2010) result in simulations with worse fits to the observed AGN fractions. We also prefer a steeper slope in $L_{\text{bol}}/L_{\text{Edd}}$ because it qualitatively reflects the decreasing efficiency η for radiatively inefficient accretion at low \dot{m} (Xie & Yuan 2012). With a fixed number of Eddington ratios in the random distribution, we set $P_0 = 1$ and numerically control the normalization (and average Eddington ratio) by changing the lower bound $\log(\lambda_{\text{min}})$ of the distribution.

To convert Eddington ratio to luminosity, we estimate black hole mass using the Gültekin et al. (2009) $M_{\text{BH}} - \sigma$

relation:

$$\log(M_{\text{BH}}/M_{\odot}) = \alpha + \beta \log(\sigma/200 \text{ km s}^{-1}) + \epsilon_0 \quad (8)$$

Here $\alpha = 8.12$, $\beta = 4.24$, and the intrinsic scatter $\epsilon_0 = 0.44$. Kormendy & Ho (2013) demonstrate that the $M_{\text{BH}} - \sigma$ relation for classical bulges has significantly higher normalization ($\alpha = 8.49$) and lower scatter ($\epsilon_0 = 0.29$), suggesting that the Gültekin et al. (2009) normalization is lower due to the inclusion of pseudobulges. However nearly all of our galaxies have insufficient data to reliably separate classical bulges and pseudobulges, so we retain the Gültekin et al. (2009) relation. In the Appendix we also test a constant M_{BH}/M_* ratio, finding that it results in a significantly worse fit to the data.

Equation 8 is appropriate only for velocity dispersions corresponding to a galaxy bulge. We remove velocity dispersions from unresolved rotation or disordered kinematics by requiring that the empirically-drawn galaxies be face-on ($b/a > 0.5$), have well-measured velocity dispersion (error in $\sigma < 60 \text{ km s}^{-1}$), and using iterative 2σ clipping to remove outliers. Kassin et al. (2012) find that most $z \sim 0$ galaxies with $\log(M_*/M_{\odot}) \gtrsim 8.5$ are settled disks, suggesting that unsettled disks with dispersion-dominated kinematics are likely to be removed by the 2σ outlier rejection. The 3" fiber aperture means that these velocity dispersions are typically measured over a radius smaller than r_e (see Figure 9). However bulges typically have flat velocity dispersion profiles over $0.1 < r/r_e < 10$: Cappellari et al. (2006) measure a typical $\sigma(r) = \sigma_e(r/r_e)^{-0.066}$ over this range, and so we assume $\sigma \simeq \sigma_e$ for our galaxies. Galaxies with upper limits in velocity dispersion are included using survival analysis, assuming a normal parent distribution (before clipping) described by the median σ and its NMAD.

To convert bolometric luminosity into the extinction-corrected [OIII] line luminosity we use the following bolometric correction:

$$\frac{L_{\text{bol}}}{10^{40} \text{ erg s}^{-1}} = 112 \left(\frac{L[\text{OIII}]}{10^{40} \text{ erg s}^{-1}} \right)^{1.2} \quad (9)$$

This equation is a power-law fit to the luminosity-dependent bolometric corrections found by Lamastra et al. (2009). Equation 9 is roughly consistent with the findings of Stern & Laor (2012) for observed (not corrected for extinction) $L[\text{OIII}]$, given the 1–2 mag of extinction increasing from low to high $L[\text{OIII}]$ observed in our galaxies. We adopt an intrinsic scatter of 0.4 dex in the $L[\text{OIII}]$ bolometric correction which reflects the range of AGN spectral energy distributions and details of the emission geometry. This intrinsic scatter dominates over the measurement errors in line flux and dust correction. Stern & Laor (2012) measure a slightly larger scatter of 0.6 dex for $L[\text{OIII}]$, but some of their measured scatter is due to the range of AGN extinction. A smaller scatter of 0.4 dex is probably more appropriate for the extinction-corrected $L[\text{OIII}]$ used in this work. Using a scatter of 0.6 dex in $L_{\text{bol}}/L[\text{OIII}]$ instead of the adopted 0.4 dex systematically decreases the inferred Eddington ratios by ~ 0.1 dex, with no change in the relative Eddington ratios across galaxy properties.

From $L[\text{OIII}]_{\text{AGN}}$, all of the (extinction-corrected)

emission lines in the BPT and VO87 diagrams can be estimated using line ratios for “pure AGN NLRs”:

$$\text{H}\alpha/\text{H}\beta = 3.1. \quad (10)$$

$$\log([\text{OIII}]/\text{H}\beta) = 0.5 \pm 0.3, \quad (11)$$

$$\log([\text{SII}]/\text{H}\alpha) = -0.2 \pm 0.2, \quad (12)$$

$$\log([\text{NII}]/\text{H}\alpha) = \langle \log([\text{NII}]/\text{H}\alpha)_{\text{gal}} \rangle + 0.45 \pm 0.2. \quad (13)$$

Equation 10 is the intrinsic Balmer decrement that best describes typical AGN NLR conditions (Osterbrock & Ferland 2006), with ionization from the AGN causing a value slightly exceeding the $\text{H}\alpha/\text{H}\beta = 2.86$ of HII regions. Equations 11 and 12 are empirically drawn from the AGN locus in the observed BPT and VO87 diagrams. Equation 13 similarly reflects the range of observed AGNs, but also allows for a metallicity-dependent AGN NLR. The scatter in each equation was chosen to empirically reproduce the observed line-ratio distributions in the BPT and VO87 diagrams, and effectively accounts for a range in NLR geometry and ionization conditions (see Section 5.5).

To model the metallicity-dependent NLR line ratios, we follow the models of Kewley et al. (2001), which show that lower metallicity decreases the $[\text{NII}]/\text{H}\alpha$ ratio of the AGN NLR and galaxy by the same degree, while the AGN $[\text{OIII}]/\text{H}\beta$ and $[\text{SII}]/\text{H}\alpha$ ratios change little. Similar metallicity effects on the AGN narrow-line region and host galaxy are plausible due to the large (few-kpc) size of the typical AGN narrow-line region (e.g., Bennert et al. 2002)¹⁰. Most galaxies have fairly flat metallicity gradients with $\alpha_{\text{O/H}} = -0.1 \text{ dex}/R_e$ (Zaritsky et al. 1994; Sánchez et al. 2014), further suggesting that the NLR metallicity should be similar to the galaxy metallicity measured within the SDSS fiber (which typically covers $0.3\text{--}0.6R_e$, see Figure 9). The scatter in Equation 13 effectively includes the potential effects of scatter in metallicity between the galaxy and the AGN NLR. In the Appendix we also test a simulation with a uniform-metallicity NLR (i.e., a constant NLR $[\text{NII}]/\text{H}\alpha$ ratio), finding that it results in a significantly worse fit to the observations. Section 5.5 demonstrates that the line ratios and scatter assumed in Equations 10–13 result in simulated BPT and VO87 diagrams which are similar to the observed diagrams.

5.2. Testing a Uniform Eddington Ratio Distribution

We begin by testing a “uniform- $L_{\text{bol}}/L_{\text{Edd}}$ ” model similar to that advocated by Aird et al. (2012): the same Eddington ratio distribution in every bin of galaxy properties (color, sSFR, and concentration versus stellar mass). The simulation uses the Eddington ratio distribution, $M_{\text{BH}} - \sigma$ relation, $L_{\text{bol}}/L[\text{OIII}]$ bolometric correction, and metallicity-dependent AGN NLR line ratios outlined in Equations 7–13 above. The normalization of Equation 7 is set to be the same over all galaxy properties: $\log(\lambda_{\text{min}}) = -5.0$ for BPT AGNs and $\log(\lambda_{\text{min}}) = -5.5$

¹⁰ The large size and potential metallicity variation of the AGN NLR is in contrast to the much smaller broad-line region, which is observed to have super-solar metallicity over a wide range in mass and redshift (e.g., Nagao et al. 2006; Juarez et al. 2009; Matsuoka et al. 2011).

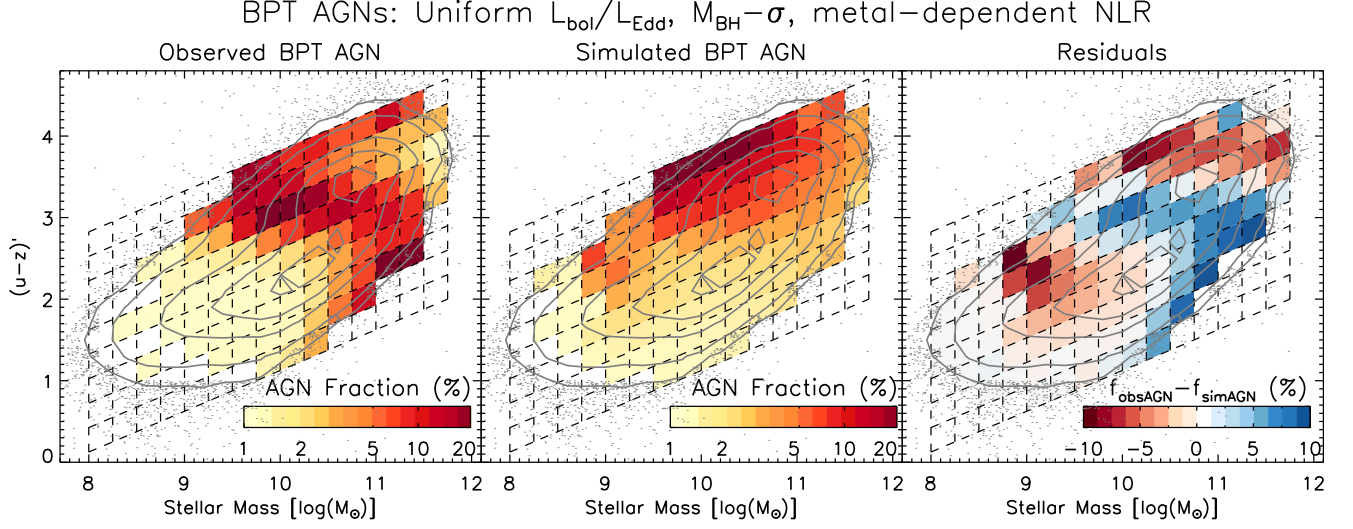


FIG. 11.— The fraction of BPT AGNs with host galaxy color and stellar mass from both observations and the “uniform- $L_{\text{bol}}/L_{\text{Edd}}$ ” simulation. The simulation uses the assumptions outlined in Equations 7–13: a Schechter function $L_{\text{bol}}/L_{\text{Edd}}$, $M_{\text{BH}}-\sigma$ relation, luminosity-dependent $L_{\text{bol}}/L[\text{OIII}]$ bolometric correction, and metallicity-dependent AGN NLR line ratios. AGN fraction is indicated by the bin shading and gray contours represent the distribution of well-measured galaxies. Similar to the simple AGN limits of Section 4.1 and Figure 8, star formation dilution results in fewer AGNs identified in blue galaxies. However the uniform- $L_{\text{bol}}/L_{\text{Edd}}$ model does a poor job of reproducing the data, with too many simulated AGNs in red galaxies and too few in high-mass blue/green galaxies.

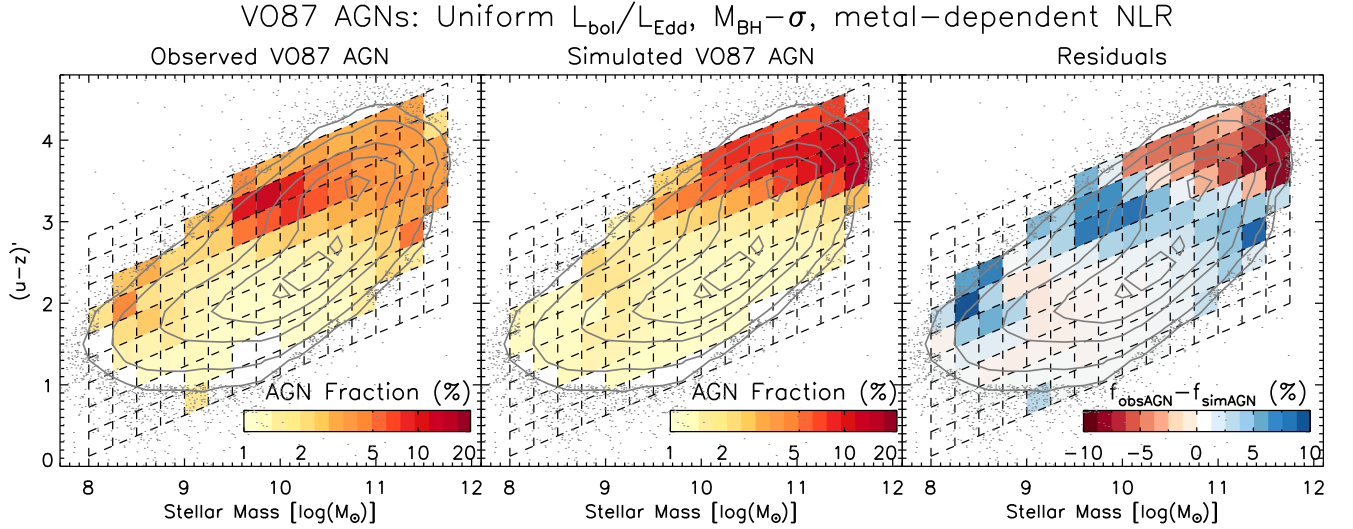


FIG. 12.— The fraction of VO87 AGNs with host galaxy color and stellar mass from the “uniform- $L_{\text{bol}}/L_{\text{Edd}}$ ” simulation compared to the observations. Bin shading indicates the AGN fraction and gray contours represent the well-measured galaxy sample. As in Figure 11, the simulation overpredicts the number of AGNs in massive red galaxies and underpredicts the AGN fraction in massive blue galaxies. The uniform- $L_{\text{bol}}/L_{\text{Edd}}$ simulation also fails to reproduce the AGNs in low-mass hosts identified by the VO87 but not the BPT.

for VO87 AGNs, with each value set to minimize the summed χ^2 values from comparing to the observations:

$$\chi^2 = \sum_{i=1}^{N_{\text{bins}}} \left(\frac{(f_{\text{obsAGN}} - f_{\text{simAGN}})^2}{\sigma^2(f_{\text{obsAGN}})} \right). \quad (14)$$

Here f_{obsAGN} and f_{simAGN} are the observed and simulated AGN fractions among well-measured galaxies, and $\sigma(f_{\text{obsAGN}})$ is the binomial error in f_{obsAGN} (calculated following Cameron 2011).

The “uniform- $L_{\text{bol}}/L_{\text{Edd}}$ ” simulation is compared to the observed BPT AGN fractions across the color–mass diagram in Figure 11. A uniform Eddington ratio distribution does a poor job of reproducing the observations, with significant residuals across the galaxy popu-

lation. The simulations similarly do a similarly poor job of reproducing the observed VO87 AGN population, as seen in Figure 12. The simulated and observed BPT AGN fractions in the sSFR–mass and concentration–mass diagrams are also shown in Figures 13 and 14, respectively. In the Appendix we show that the mismatch with observations is even worse when assuming a constant M_{BH}/M_* ratio or a metal-rich NLR. In all cases the “uniform- $L_{\text{bol}}/L_{\text{Edd}}$ ” model overpredicts the observed AGN fraction in massive red, low-sSFR, concentrated galaxies, underpredicts in the bluest, highest-sSFR, least-concentrated massive galaxies, and overpredicts again in most low-mass galaxies.

The overprediction of AGNs in massive red (low-sSFR, concentrated) galaxies is especially pronounced if we con-

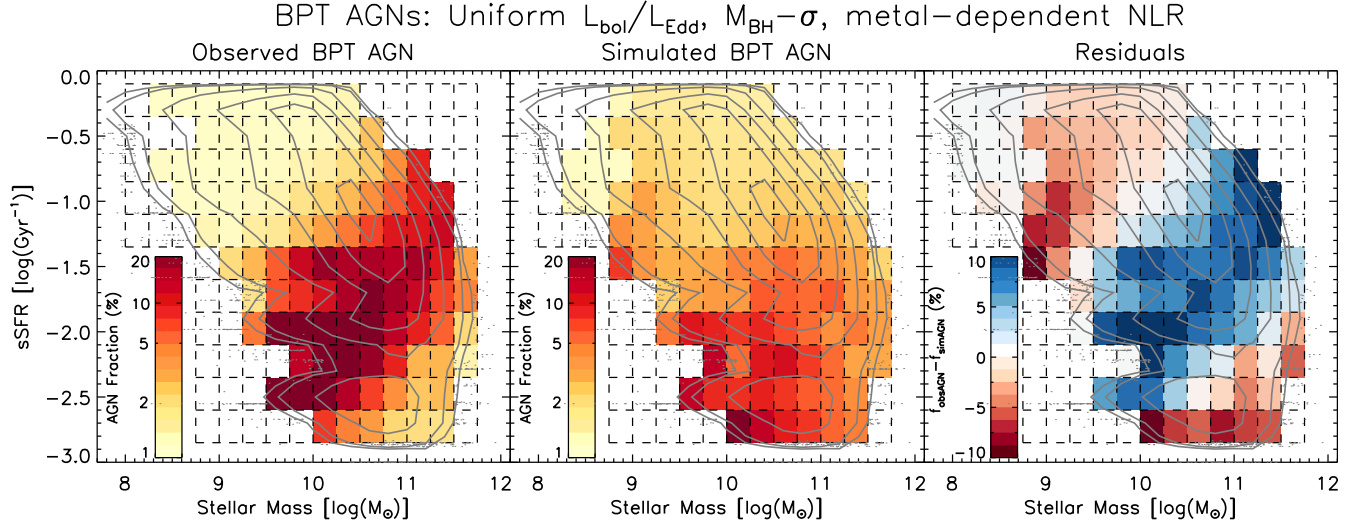


FIG. 13.— The observed and simulated BPT AGN fractions with host galaxy specific star formation rate and stellar mass, using the “uniform- $L_{\text{bol}}/L_{\text{Edd}}$ ” model. The simulation underpredicts the number of AGNs in moderate-sSFR and moderate-mass galaxies, underpredicts the observed AGN fraction at both high and low sSFR and stellar mass. In Sections 5.3 and 5.4 we show that, rather than a uniform Eddington ratio, the observations imply a correlation between Eddington ratio and sSFR in massive galaxies, with some hint of undermassive black holes in low-mass hosts.

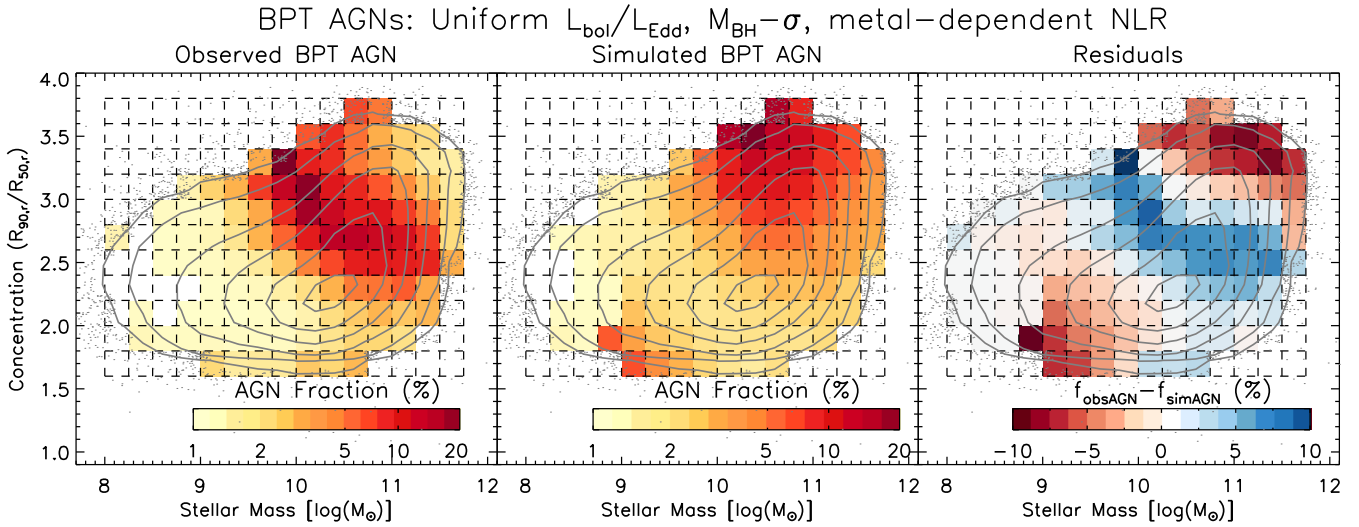


FIG. 14.— The observed and simulated BPT AGN fractions with host galaxy specific concentration ($R_{90,r}/R_{50,r}$) and stellar mass, using “uniform- $L_{\text{bol}}/L_{\text{Edd}}$ ” model. The uniform Eddington ratio model has the same zebra-like mismatch to the data as in Figures 11 and 13, underpredicting the observed AGN fraction in moderate-mass/moderate-concentration galaxies and overpredicting at low-mass/low-concentration and high-mass/high-concentration.

sider the difference in AGN fractions between the well-measured and full samples of galaxies. In Section 3.3 we showed that the apparent AGN fraction for massive red (low-sSFR, concentrated) galaxies for the full sample is lower than in the well-measured sample. Thus the simulated AGN fraction in such galaxies is likely to be even more overpredicted when compared to the full dataset.

From Figures 11–14 we conclude that, with plausible model assumptions for a bolometric correction, the $M_{\text{BH}} - \sigma$ relation, and pure AGN line ratios, the observed fractions of line-ratio AGNs are inconsistent with a uniform Eddington ratio distribution. In the next subsections we instead allow Eddington ratio and black hole mass to be free parameters with galaxy properties. Rather than a uniform Eddington ratio distribution, the observed line-ratio AGN fractions are best reproduced by

a model where (a) AGN accretion rate is correlated with host sSFR in massive ($\log(M_*/M_\odot) > 10$) host galaxies and (b) low-mass ($\log(M_*/M_\odot) < 10$) galaxies may have a lower black hole occupation function.

5.3. Non-Uniform AGN Duty Cycle

Given the poor fit of the “uniform- $L_{\text{bol}}/L_{\text{Edd}}$ ” simulations, in this subsection we instead allow the normalization of the Eddington ratio (i.e., the average Eddington ratio) to be a free parameter with galaxy properties. Varying the normalization of the Eddington ratio distribution effectively changes the AGN duty cycle (i.e., the number of AGNs above some accretion rate threshold). Functionally, this simulation follows steps 1–4 described in the beginning of the Section. We retain the same bolometric correction (Equation 9), $M_{\text{BH}} - \sigma$

relation (Equation 8), and metallicity-dependent NLR (Equations 10–13) as in the uniform- $L_{\text{bol}}/L_{\text{Edd}}$ simulation. We also use the Schechter function to describe the AGN Eddington ratio distribution given in Equation 7 (with the same declining power-law slope of $\alpha = 0.6$), numerically controlling its normalization using the lower bound $(L_{\text{bol}}/L_{\text{Edd}})_{\text{min}}$. However instead of a uniform lower bound, we fit over a grid starting from $\log(L_{\text{bol}}/L_{\text{Edd}})_{\text{min}} = -3$ and decreasing by $\Delta \log(L_{\text{bol}}/L_{\text{Edd}})_{\text{min}} = 0.05$ until the simulations produce an AGN fraction equal to the observations. Bins with observed AGN fractions consistent with zero (using their $1\text{-}\sigma$ binomial error) result in upper limits for the Eddington ratio normalization, since lower Eddington ratios would similarly result in zero simulated AGNs. We report the best-fit Eddington ratios using the distribution’s average: for our Schechter function parameterization, $\langle \log(L_{\text{bol}}/L_{\text{Edd}}) \rangle \simeq 0.91 \log(L_{\text{bol}}/L_{\text{Edd}})_{\text{min}} + 0.25$. A higher average Eddington ratio can also be interpreted as a higher AGN duty cycle (i.e. a higher fraction of galaxies hosting an AGN above some accretion rate).

Figures 15 and 16 present the average Eddington ratios from this “non-uniform $L_{\text{bol}}/L_{\text{Edd}}$ ” model in bins of color–mass, sSFR–mass, and concentration–mass for both BPT AGNs and VO87 AGNs. The left and middle columns of each figure show the average Eddington ratios calculated from the well-measured set of galaxies. In the right column we make a correction to estimate the average Eddington ratio for the full galaxy sample, assuming that poorly-measured galaxies have the same median ratio of $L_{\text{bol}}/L_{\text{Edd}}/[L(\text{OIII})_{\text{total}}/M_*]$ as the well-measured galaxies. Within the narrow ranges of M_* and σ in each bin of galaxy properties, this assumption is essentially the same as assuming the same fractional AGN contribution to $L(\text{OIII})_{\text{total}}$ in both well-measured and poorly-measured galaxies. Correcting for poorly-measured galaxies tends to slightly decrease (by up to 0.3 dex) the average Eddington ratio in high-mass red, low-sSFR, concentrated galaxies (i.e., those galaxies most likely to be weak-lined with poorly-constrained line ratios). In all three panels, the observed AGN fractions in $M_* \lesssim 10^9 M_\odot$ galaxies are frequently consistent with zero, resulting in poorly-constrained upper limits for the intrinsic Eddington ratios.

The relationship between AGN Eddington ratio and galaxy properties is best understood separately for high-mass ($\log(M_*/M_\odot) \gtrsim 10$) and low-mass ($\log(M_*/M_\odot) \lesssim 10$) galaxies. We begin with massive galaxies, examining the average AGN Eddington ratio as a function of stellar mass and specific star formation rate.

Figure 17 presents the average Eddington ratio in massive ($\log(M_*/M_\odot) \geq 10$) galaxies as a function of stellar mass, for both individual bins of sSFR (colored points) and the weighted average of the full massive galaxy population (black lines). The best-fit line to the combined BPT and VO87 models has a slope of 0.065 ± 0.023 : consistent with zero. In other words, in massive ($\log(M_*/M_\odot) \geq 10$) galaxies, we find that AGN accretion is independent of stellar mass. This result agrees with the uniform $L_{\text{bol}}/L_{\text{Edd}}$ with stellar mass proposed by Aird et al. (2012) for X-ray AGN hosts.

However, Figure 18 demonstrates that the average Eddington ratio in massive galaxies is strongly

non-uniform with galaxy sSFR, increasing by ~ 2 dex with increasing sSFR. Previous work similarly found that rapidly accreting AGNs are much more common in massive star-forming hosts than in massive quiescent hosts (e.g., Kauffmann et al. 2003; Heckman et al. 2004; Kauffmann & Heckman 2009; Trump et al. 2013a; Rosario et al. 2013a,b; Matsuoka et al. 2014; Azadi et al. 2015). The solid line in Figure 18 shows the weighted average Eddington ratio over all mass bins, at a given sSFR. We fit a double power-law to the Eddington ratios in each sSFR bin for both the BPT and VO87 model results. With $x = \log(\text{sSFR}/\text{Gyr}^{-1})$ and $y = \log(L_{\text{bol}}/L_{\text{Edd}})$, the best-fit (minimum- χ^2) relationship is given by:

1. For $x = \log(\text{sSFR}/\text{Gyr}^{-1}) < -1.5$,

$$y = (0.92 \pm 0.07)x - (2.29 \pm 0.03). \quad (15)$$

2. For $x = \log(\text{sSFR}/\text{Gyr}^{-1}) > -1.5$,

$$y = (-0.10 \pm 0.11)x - (3.79 \pm 0.09). \quad (16)$$

Error bars in slope and y-intercept are the 1σ errors of the best-fit values. In other words, $L_{\text{bol}}/L_{\text{Edd}}$ increases as a power-law with sSFR until $\log(\text{sSFR}/\text{Gyr}^{-1}) = -1.5$, at which point $\log(L_{\text{bol}}/L_{\text{Edd}})$ becomes flat with $\log(\text{sSFR})$. The slope of the log-log line (exponent of the power-law) is well-constrained to be close to unity, in striking agreement with the constant ratio of $L_{\text{bol}}/L_{\text{Edd}}$ to sSFR in the ensemble of higher-redshift X-ray hosts presented by Mullaney et al. (2012). The turnover and lack of dependence of $L_{\text{bol}}/L_{\text{Edd}}$ on sSFR at $\log(\text{sSFR}/\text{Gyr}^{-1}) > -1.5$ might be due to AGN contamination in the broad-band photometry at high Eddington ratios: contribution from a blue AGN continuum would effectively overestimate sSFR (e.g., Appendix A of Bongiorno et al. 2012). If sSFR is accurately measured and there is negligible AGN contamination, the flattening of $L_{\text{bol}}/L_{\text{Edd}}$ with sSFR may represent a ceiling in AGN accretion for host galaxies on the “star formation mass sequence,” described by $\log(\text{sSFR}/\text{Gyr}^{-1}) \simeq -1.1 \pm 0.3$ at $z \sim 0$ (Whitaker et al. 2012). Similarly, Rosario et al. (2013b) and Azadi et al. (2015) argue that AGNs are more common in star-forming hosts, but otherwise there is no enhancement of AGN activity with additional star formation.

Interpreting the relationship between AGN accretion and galaxy properties from Figures 15 and 16 is more difficult in low-mass galaxies. At the lowest masses ($\log(M_*/M_\odot) < 9$) the Eddington ratios are essentially unconstrained due to zero observed AGNs and extreme star formation dilution. Even when the average Eddington ratios are well-constrained at $9 < \log(M_*/M_\odot) < 10$, such low-mass galaxies may have black hole masses that are not well-described by the $M_{\text{BH}} - \sigma$ relation. Applying the $M_{\text{BH}} - \sigma$ relation might overestimate black hole mass either because σ is poorly measured or results from something other than bulge kinematics, or due to a black hole occupation function that is less than 100%. In the next section we investigate a non-uniform $M_{\text{BH}} - \sigma$ relation.

5.4. Non-Uniform Black Hole Occupation

Greene et al. (2010) demonstrated that low-mass ($\sim 10^9 M_\odot$) galaxies with accurate megamaser-disk M_{BH}

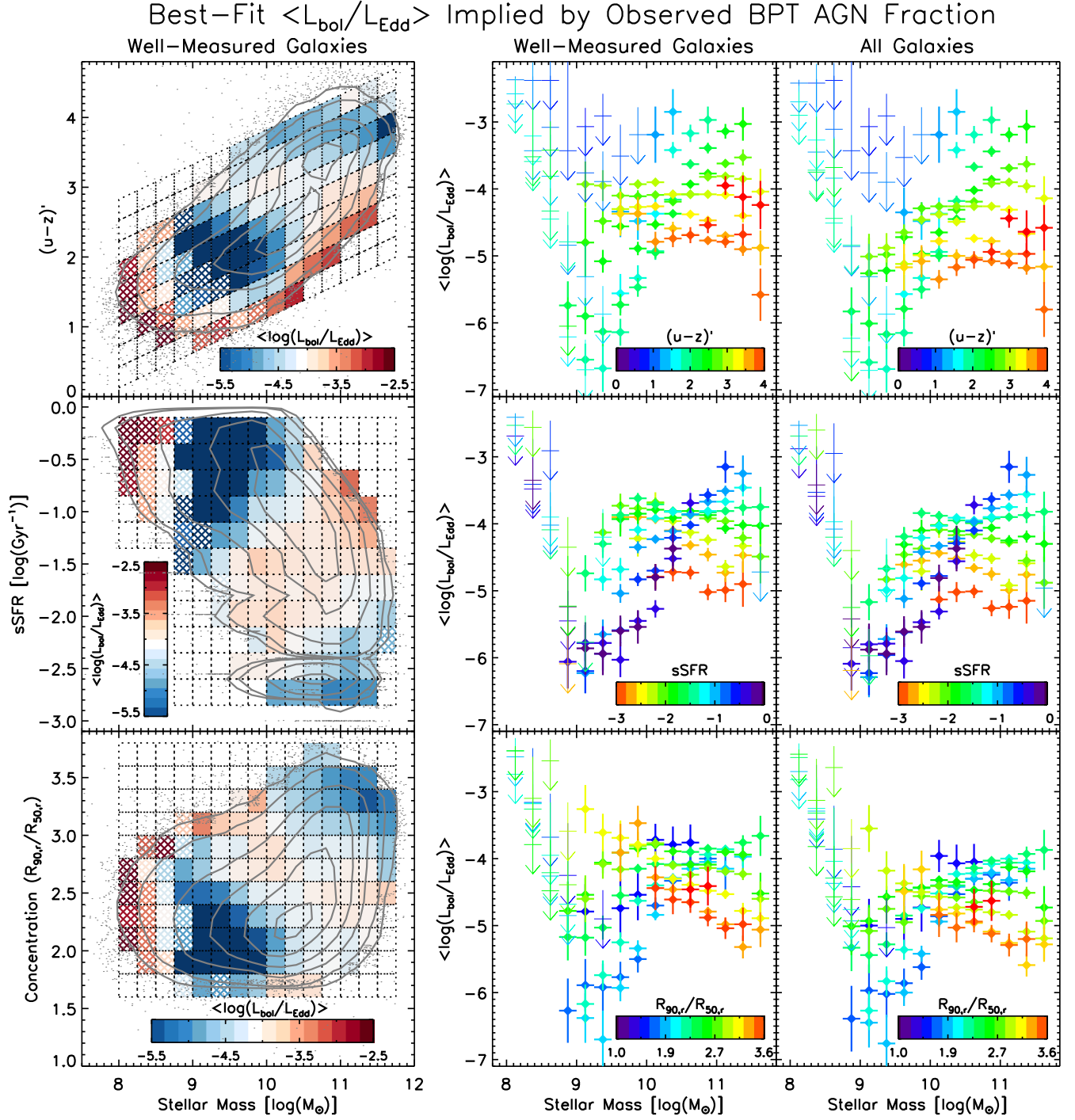


FIG. 15.— *Left:* The average Eddington ratios in bins of galaxy color–mass, sSFR–mass, and concentration–mass from the “non-uniform” $L_{\text{bol}}/L_{\text{Edd}}$ model fits that reproduce the observed BPT AGN fraction for well-measured galaxies in each bin. Gray contours represent the well-measured galaxy sample, and hashed bins denote Eddington ratio upper limits where the observed AGN fraction is consistent with zero (given its binomial error). *Center:* The same average Eddington ratios versus stellar mass in each bin, color-coded by $(u-z)'$, sSFR, or $R_{90,r}/R_{50,r}$. Vertical error bars represent the NMAD of the Monte Carlo simulation results. Upper limits due to an observed AGN fraction consistent with zero (the hashed bins in the left panel) are shown as thinner lines. *Right:* Average Eddington ratios for the full galaxy sample, assuming that poorly-measured galaxies have the same median $L[\text{O III}]_{\text{AGN}}/L[\text{O III}]_{\text{total}}$ as the well-measured galaxies. In massive galaxies, the AGN Eddington ratios tends to be highest in hosts with blue color, high sSFR, and low concentration. The connection between AGN accretion and galaxy properties is murkier in low-mass hosts.

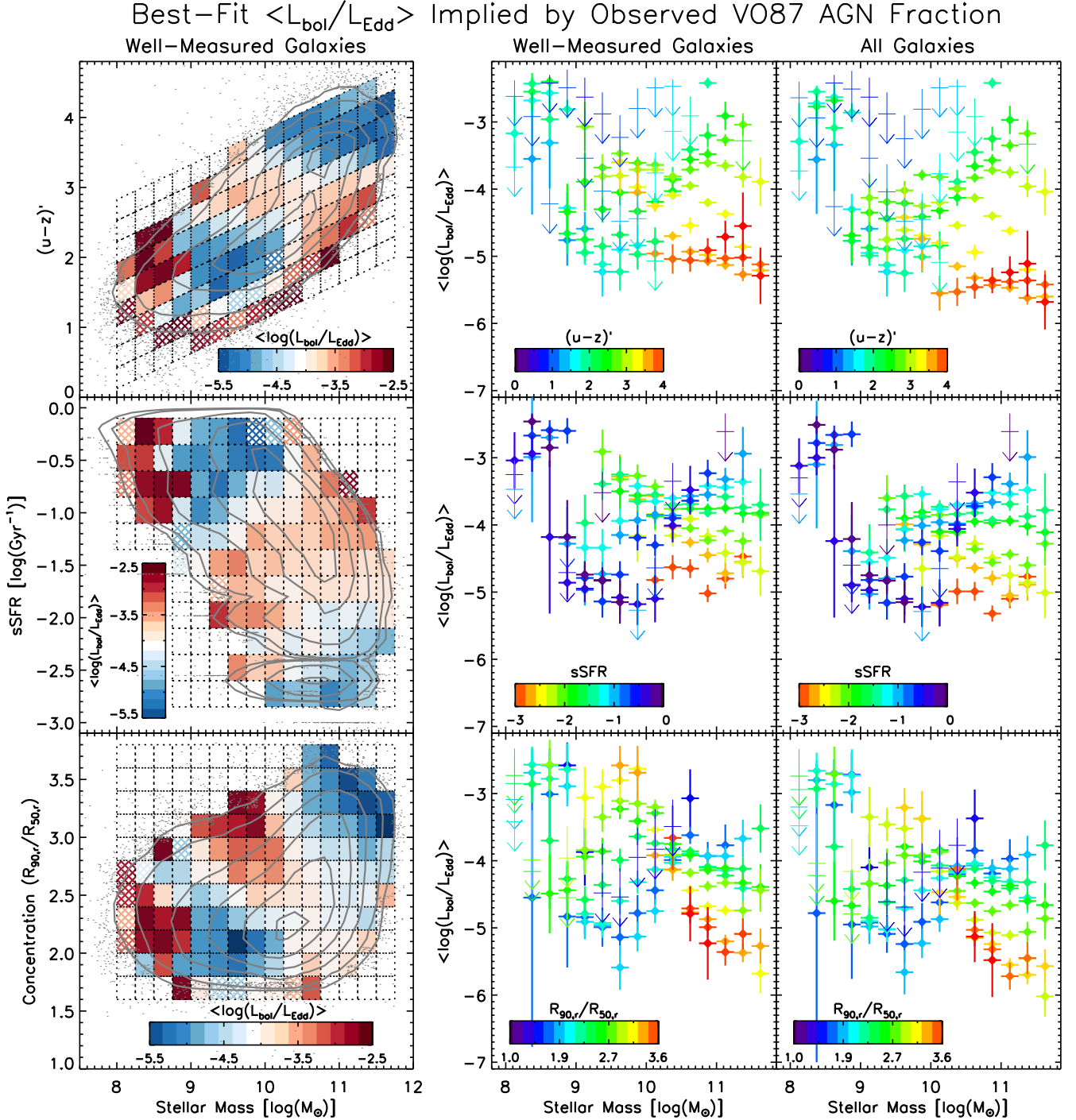


FIG. 16.— The average Eddington ratios from the “non-uniform” $L_{\text{bol}}/L_{\text{Edd}}$ model fits that match the observed VO87 AGN fractions in bins of galaxy color–mass, sSFR–mass, and concentration–mass. The well-measured galaxy sample is shown by gray contours. Upper limits in Eddington ratio are marked as hashed bins (left panel) and thinner lines (center and right panels). Just as was the case for BPT AGNs in Figure 15, there is a connection between Eddington ratio and host galaxy blue color, sSFR, and low concentration in high-mass ($\log(M_*/M_\odot) \gtrsim 10$) galaxies. In low-mass ($\log(M_*/M_\odot) \lesssim 10$) galaxies the connection between host properties and AGN accretion is much less clear.

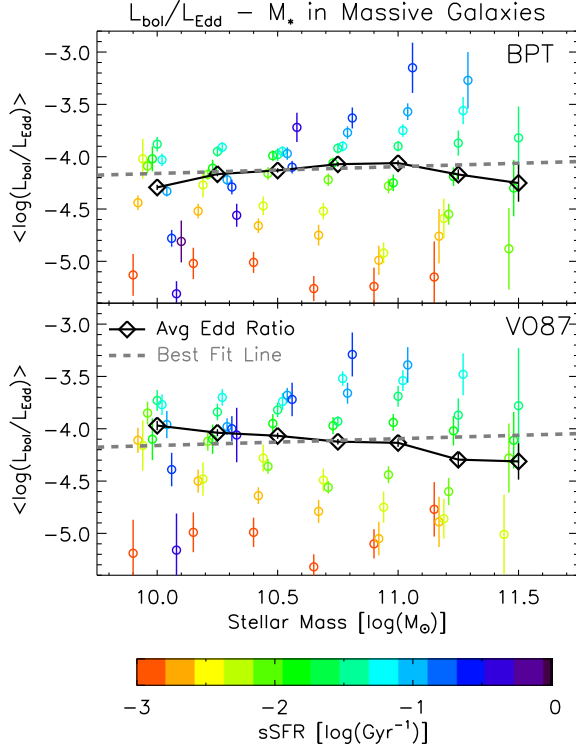


FIG. 17.— The average AGN Eddington ratio implied by the “non-uniform” $L_{\text{bol}}/L_{\text{Edd}}$ model fits to the observed BPT (top) and VO87 (bottom) AGN fractions, as a function of galaxy stellar mass. Only massive ($\log(M_*/M_\odot) \geq 10$) galaxies are shown. Bins in sSFR are shown by the colored points (with small horizontal offsets for clarity) and the black points represent the weighted mean at each stellar mass (along with the error of the weighted mean). The best-fit line (dashed gray line) is consistent with zero, indicating that, in massive galaxies, AGN Eddington ratio is independent of stellar mass.

estimates are undermassive by ~ 0.5 dex with respect to the $M_{\text{BH}} - \sigma$ relation of massive galaxies. This sort of non-uniform $M_{\text{BH}} - \sigma$ relation, with undermassive black holes in low-mass galaxies, can be explained as a consequence of black hole seeding mechanisms. Direct collapse of primordial gas is likely to form the most massive (up to $\sim 10^6 M_\odot$) SMBH seeds (Bromm & Loeb 2003; Begelman et al. 2006; Johnson et al. 2012), but this process becomes inefficient in low-mass halos (van Wassenhove et al. 2010). Instead, low-mass galaxies likely have black holes initially formed as lower-mass (up to $\sim 200 M_\odot$) Pop III remnants (Fryer et al. 2001; Madau & Rees 2001). Thus low-mass galaxies, with low-mass initial seeds and not many mergers over their lifetime, might be expected to have a lower black hole occupation function compared to massive galaxies (Volonteri & Natarajan 2009).

In addition to the physics of black hole seed formation, it is also possible that problematic σ measurements might lead to a non-uniform $M_{\text{BH}} - \sigma$ relation. First, the measured velocity dispersions at $\log(M_*/M_\odot) < 10$ are frequently below the SDSS instrumental resolution ($\sim 70 \text{ km s}^{-1}$). Even when well-measured, the velocity dispersion of a low-mass galaxy may describe disordered kinematics rather than a settled bulge. If the velocity dispersion is overestimated for either of these reasons it will lead to an overestimate of black hole mass. However, the velocity dispersions of low-mass galaxies already im-

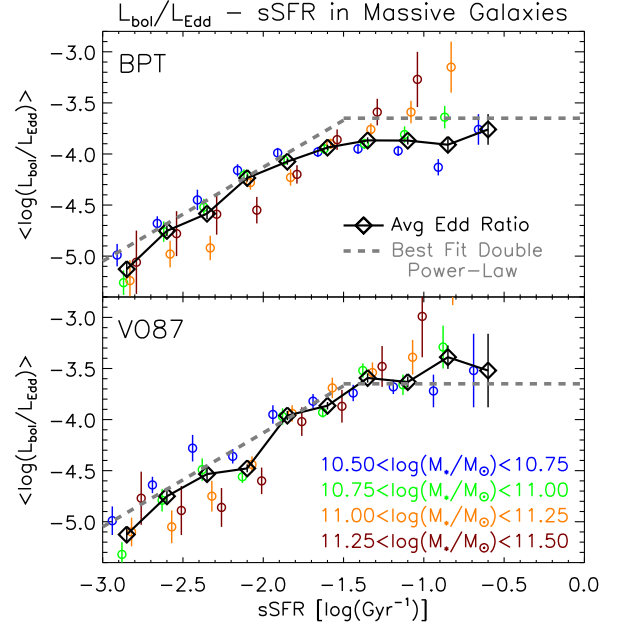


FIG. 18.— The connection between AGN Eddington ratio and host galaxy sSFR for high-mass ($\log(M_*/M_\odot) \geq 10.5$) galaxies, as implied by the BPT AGN (top) and VO87 AGN (bottom) fractions. Individual mass bins are shown by the colored points (offset horizontally from one another for clarity) and the black points represent the weighted mean at each sSFR (along with the error of the weighted mean). The gray lines are a double power-law fit to the combined BPT and VO87 data: $y = 0.92x - 2.29$ at $x < 1.5$ and $y = \log(L_{\text{bol}}/L_{\text{Edd}})$ at $x > 1.5$, where $x = \log(\text{sSFR}/\text{Gyr}^{-1})$ and $y = \log(L_{\text{bol}}/L_{\text{Edd}})$.

ply very low-mass black holes: a velocity dispersion of 35 km s^{-1} , typical of the survival analysis, results in only $M_{\text{BH}} \simeq 10^5 M_\odot$. This value already approaches the “intermediate-mass” black hole regime of direct-collapse SMBH seeds.

Fitting the AGN occupation with M_{BH} as a free parameter avoids problematic σ measurements and allows us to probe the black hole occupation function. We use the same approach as our previous simulations, following steps 1–4 outlined in Section 5. The normalization of the Eddington ratio distribution is fixed by the galaxy sSFR according to Equations 14 and 15 above, with $\langle \log(L_{\text{bol}}/L_{\text{Edd}}) \rangle \simeq 0.91 \log(L_{\text{bol}}/L_{\text{Edd}})_{\text{min}} + 0.25$. We assume that low-mass galaxies follow the same accretion–sSFR relation as massive galaxies, with any deviations caused by non-uniform black hole mass.

Figure 19 and 20 show the best-fit black hole masses with galaxy color-mass, sSFR–mass, and concentration–mass, implied by both BPT and VO87 AGNs. We quantify this M_{BH} in two ways. The left panels present $\log(M_{\text{BH}}/M_*)$, such that bins colored white match the Häring & Rix (2004) relation with $M_* = 1.4 M_{\text{bulge}}$, $M_{\text{BH}}/M_* = 0.001$. The center and right panels display the deviation from $M_{\text{BH}} - \sigma$, measured as the log-ratio of the best-fit M_{BH} and the $M_{\text{BH}}(\sigma)$ expected from the $M_{\text{BH}} - \sigma$ relation. Negative log-ratios and redder bins denote undermassive black holes, while higher log-ratios and bluer bins denote overmassive black holes. Significantly overmassive black holes are likely due to errors in the assumptions, for example, where the $L_{\text{bol}}/L_{\text{Edd}} - \text{sSFR}$ relation fails to adequately describe the data.

The “non-uniform M_{BH} ” model does not provide

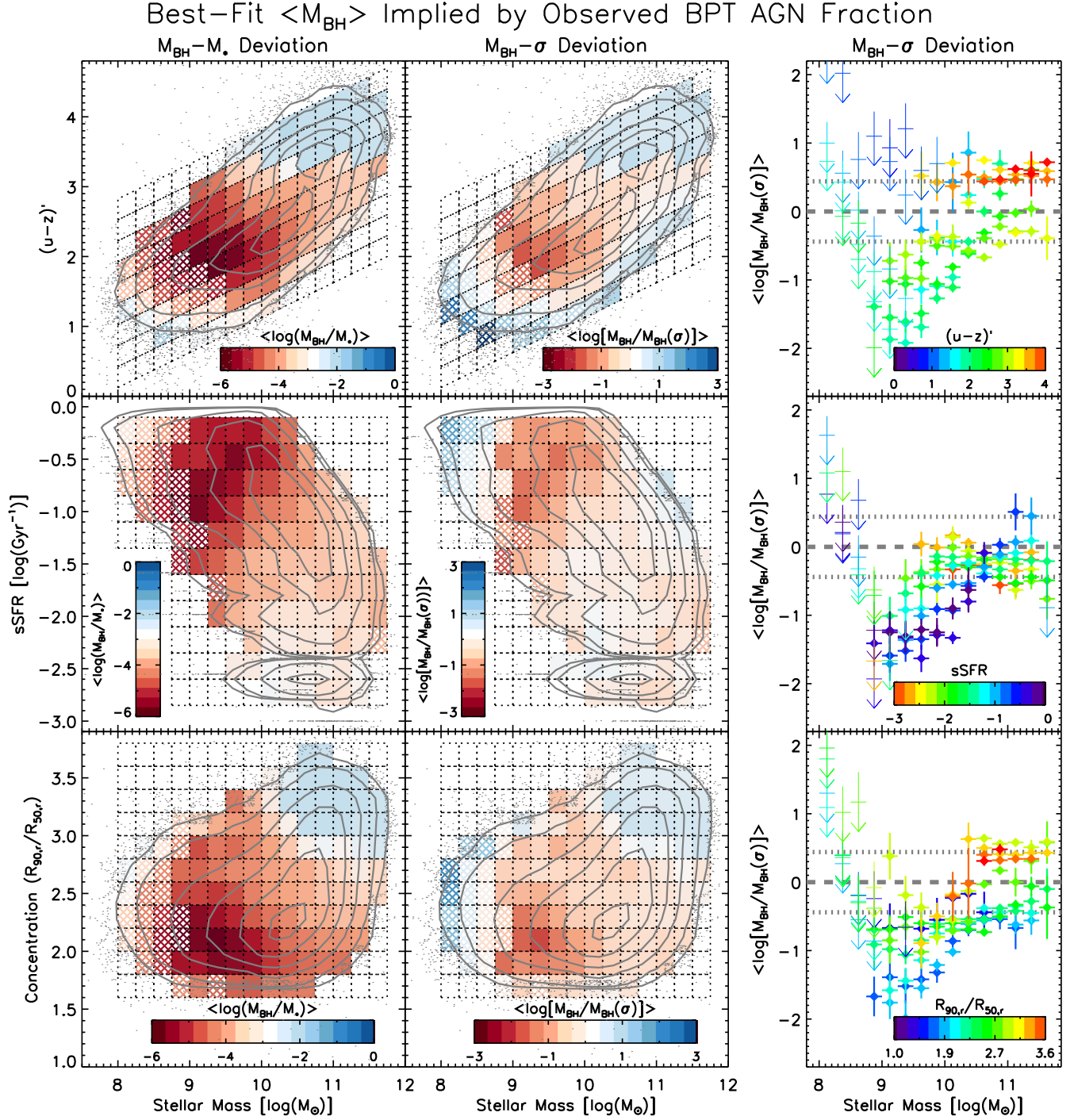


FIG. 19.— The best-fit average M_{BH} implied by the observed BPT AGN fraction in bins of galaxy color-mass, sSFR-mass, and concentration-mass. *Left:* Average black hole mass quantified as $\log(M_{\text{BH}}/M_*)$, where bins colored white match $M_{\text{BH}}/M_* = 0.001$ (the Häring & Rix (2004) relation with $M_* = 1.4M_{\text{bulge}}$). Gray contours show the distribution of well-measured galaxies, and hashed bins denote upper limits where the observed AGN fraction is consistent with zero. *Center:* Average black hole mass quantified as the deviation from $M_{\text{BH}} - \sigma$. Upper limits with no or very few detected AGNs (the hashed bins at left) are shown as thinner lines. *Right:* The same deviation from $M_{\text{BH}} - \sigma$ plotted versus stellar mass in each bin, color-coded by $(u-z)'$, sSFR, or $R_{90,r}/R_{50,r}$. The Gültekin et al. (2009) $M_{\text{BH}} - \sigma$ relation and its 1- σ scatter are shown by the dashed and dotted gray lines. Low-mass ($10^9 - 10^{10} M_{\odot}$) galaxies may have black hole masses that are 0.5–1.5 dex lower than expected from the $M_{\text{BH}} - \sigma$ relation and their velocity dispersions.

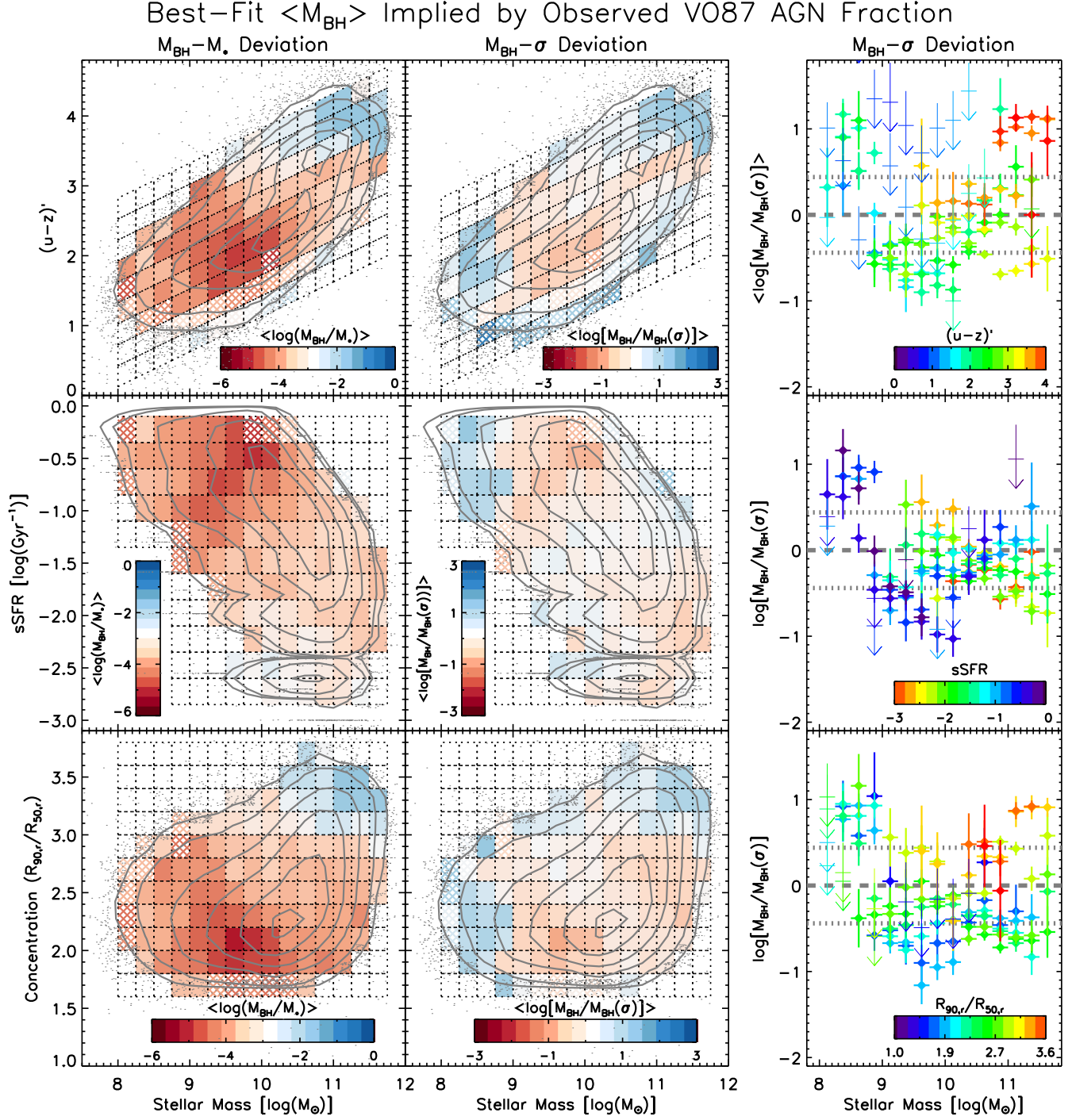


FIG. 20.— The best-fit average M_{BH} , quantified as $\log(M_{\text{BH}}/M_*)$ (left) or deviation from $M_{\text{BH}} - \sigma$ (center and right), implied by the observed V087 AGN fraction in bins of galaxy color–mass, sSFR–mass, and concentration–mass. As before, hashed bins (left panel) and thinner lines (center and right panels) denote upper limits where the observed AGN fraction is consistent with zero. Low-mass ($10^9 - 10^{10} M_\odot$) galaxies may have slightly undermassive black holes that are ~ 0.5 – 1 dex lower than expected from the $M_{\text{BH}} - \sigma$ relation and their velocity dispersions.

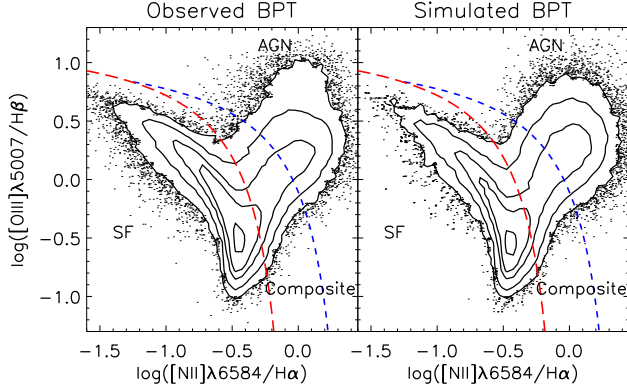


FIG. 21.— The observed and simulated line ratio distributions in the BPT diagram. The dashed red line represents the empirical line of Kauffmann et al. (2003) that we use for AGN/SF classification, and the short-dashed blue line also shows the Kewley et al. (2001) maximal starburst line. The simulated AGN line ratios are broadly consistent with the observed data, with minor differences likely arising from details of NLR physical conditions.

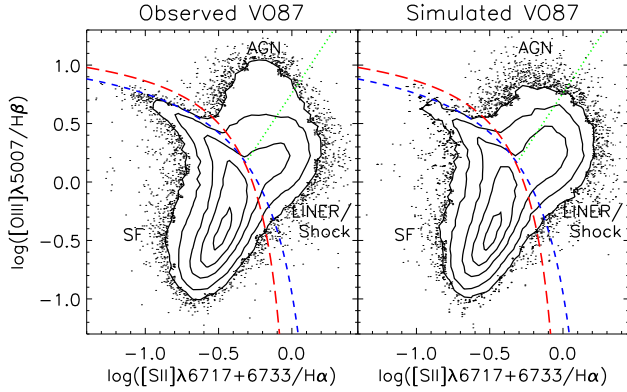


FIG. 22.— The observed and simulated VO87 diagrams. The dashed red and dotted green lines show our adopted AGN/SF and AGN/LINER classification, respectively: we empirically create the AGN/SF line and the AGN/LINER line is from Kewley et al. (2006). The blue short-dashed line also shows the Kewley et al. (2001) maximal starburst line. As in the BPT diagram in Figure 21, there is broad agreement between the observed and simulated VO87 AGN line ratio distributions.

any real constraints on M_{BH} for the least-massive ($\log(M_*/M_\odot) \lesssim 9$) galaxies, since their lack of observed AGNs and extreme star formation dilution allow almost any $M_{\text{BH}} - \sigma$ normalization. The model fits do, however, provide interesting results for galaxies in the range $9 \lesssim \log(M_*/M_\odot) \lesssim 10$. The BPT and VO87 AGN fractions both imply undermassive black holes by 0.5–1.5 dex in these low-mass hosts. This result is particularly true for the least-concentrated and highest-sSFR galaxies, which are also most likely to have poorly-understood velocity dispersions (due to disordered kinematics or below the instrumental resolution) and/or lower black hole occupation. We further discuss how the $M_{\text{BH}} - \sigma$ deviations of Figures 19 and 20 relate to black hole occupation and the SMBH seed distribution in Section 6.5.

5.5. Comparing the Observed and Simulated Line Ratio Distributions

The previous two simulations are fit to match the observed AGN fraction as a function of galaxy properties. It is also useful to see if they reproduce the observed line

ratio distribution: this functions as a consistency check on our assumed “pure AGN NLR” line ratios.

Figure 21 compares the observed and simulated BPT diagrams, and Figure 22 compares the observed and simulated VO87 diagrams. In both cases the simulated line ratios are drawn from a single realization of the Monte Carlo simulations in the non-uniform $L_{\text{bol}}/L_{\text{Edd}}$ model fit to the galaxy color–mass distribution. The line ratio distributions are similar for fits to bins in galaxy sSFR–mass and concentration–mass, and for the non-uniform M_{BH} model, differing only due to the randomly drawn nature of each realization. Because the simulations were fit to match the observed AGN fractions, the number of galaxies classified as AGNs or SF-dominated is identical for both observed and simulated line ratios. The simulated SF sequence is also nearly identical to the observed ratios, since the simulations begin from a randomly-drawn subset of observed non-AGN line ratios.

Meanwhile the simulated AGN line ratios are broadly similar to the observations. The agreement is especially good in the $[\text{NII}]/\text{H}\alpha$ and $[\text{SII}]/\text{H}\alpha$ ratios, suggesting that our assumed metallicity-dependent NLR model (Equations 10–13) is reasonably accurate. There are some differences in the shapes of the observed and simulated $[\text{OIII}]/\text{H}\beta$ distributions. In particular, the observed line ratios probably do not follow a log-normal distribution, but instead depend on physical NLR conditions such as ionization or cloud structure (e.g., Groves et al. 2004; Richardson et al. 2014). The NLR physical conditions may change with AGN Eddington ratio, suggesting that it is inaccurate to assume the same normally-distributed pure line ratios for every AGN. Still, our simple “evolving NLR” description broadly captures the locus and range of observed line ratios, and our assumed log-normal distributions are reasonable in the absence of a better understanding of AGN NLR physical conditions.

6. IMPLICATIONS FOR AGN HOST GALAXY PROPERTIES

The previous sections showed that both the BPT and VO87 AGN selection methods suffer from significant bias in low-mass, blue, high-sSFR, low-concentration galaxies due to star formation dilution. After carefully modeling this bias, we found that the intrinsic AGN population is not well-described by a uniform Eddington ratio distribution over all galaxy properties. Instead there is likely to be a connection between AGN accretion and host galaxy sSFR in massive galaxies. In low-mass galaxies there is also some potential for slightly undermassive black holes compared to the $M_{\text{BH}} - \sigma$ relation.

Below we discuss the ramifications of the line-ratio selection bias and the implied AGN occupation function with galaxy properties.

6.1. Limitations of Line-Ratio AGN Selection

As noted in Section 4.1, the biases of line-ratio AGN selection depend on how AGN power is quantified. The total mass accretion of black holes (integral of \dot{M} over time) is best understood by AGN luminosity, since $L_{\text{bol}} = \eta \dot{M} c^2$. Meanwhile the Eddington ratio $L_{\text{bol}}/L_{\text{Edd}}$ governs the structure of the accretion flow and feedback mode (Narayan & McClintock 2008; Ho 2008; Trump et al. 2011a; Heckman & Best 2014).

Figure 23 presents the fraction of AGNs identified by the BPT and VO87 methods as a function of both AGN

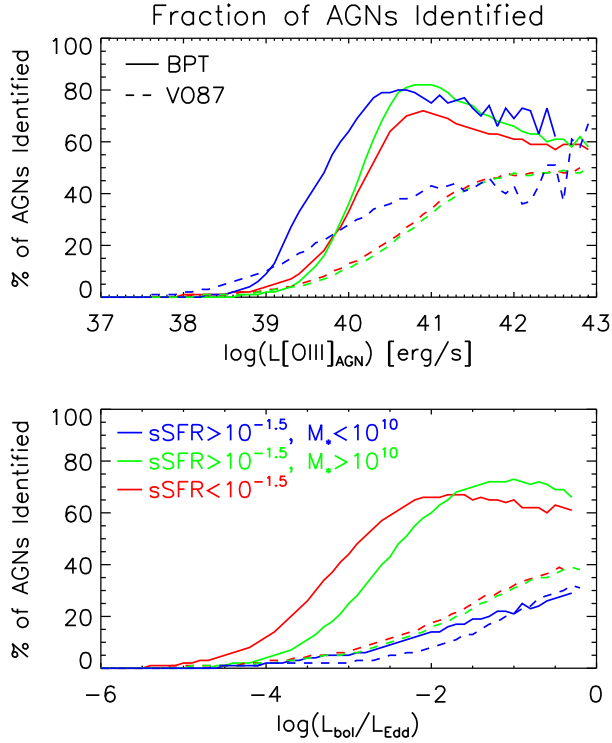


FIG. 23.— The fraction of simulated AGNs (from the “non-uniform $L_{\text{bol}}/L_{\text{Edd}}$ ” simulation) identified by the BPT and VO87 AGN classification methods. Detection fractions are presented for three different bins of galaxy properties: low-mass and low-sSFR (blue lines), high-mass and high-sSFR (green lines), and low-sSFR (which also tend to be high-mass, red lines). In the legend, sSFR is in units of Gyr^{-1} and M_* is in M_{\odot} . In terms of AGN luminosity, AGNs are reliably identified at $L[\text{OIII}] \gtrsim 10^{40.5} \text{ erg s}^{-1}$ regardless of host galaxy properties. The selection function in $L_{\text{bol}}/L_{\text{Edd}}$, on the other hand, is a strong function of galaxy properties, with fewer weakly-accreting AGNs identified in low-mass star-forming galaxies. Similar trends are seen for both the BPT and VO87 classification methods, although VO87 AGN selection has an overall lower efficiency.

luminosity and Eddington ratio. The detection fraction is determined from the “non-uniform $L_{\text{bol}}/L_{\text{Edd}}$ ” simulation presented in Section 5.3, and is the number of simulated AGNs identified by the BPT or VO87 AGN selection. As found by Kauffmann et al. (2003), the AGN detection fraction is high at $L[\text{OIII}] \gtrsim 10^{40.5} \text{ erg s}^{-1}$ ($L[\text{OIII}] \gtrsim 10^7 L_{\odot}$) regardless of galaxy properties. In other words, the use of line-ratio AGN selection is not significantly biased for estimates of *total black hole accretion* with galaxy properties. However, galaxy properties cause a strong bias for line-ratio AGN identification at a given accretion rate, similar to that discussed in Section 4.1 and Figure 8. The strong “star formation dilution” in low-mass star-forming hosts means that, at fixed Eddington ratio, many fewer AGNs are identified than in massive and low-sSFR host galaxies. Estimates of AGN *feedback and fueling efficiency* with galaxy properties are thus strongly biased when using line-ratio AGN selection. Figure 23 also demonstrates that the VO87 AGN selection method has an overall lower efficiency than BPT AGN selection.

The bias against line-ratio AGN selection is worst in galaxies with high star formation rates and low metallicity: i.e., the conditions typical of $z \gtrsim 1$ galaxies (e.g.,

Madau & Dickinson 2014). HII regions associated with rapid star formation may also have harder ionization conditions (Liu et al. 2008; Brinchmann, Pettini & Charlot 2008; Steidel et al. 2014; Shapley et al. 2015), further decreasing the contrast between AGN and star formation. Making matters even worse, the BPT locus at $z \gtrsim 1$ is suggestive of lower-metallicity AGN NLRs (Kewley et al. 2013; Juneau et al. 2014; Coil et al. 2015). Thus it is likely that HII regions dominate the emission lines of $z \gtrsim 1$ galaxies, biasing against AGN line-ratio detection to a greater degree than in our low-redshift SDSS sample (see also Coil et al. 2015).

Other AGN selection methods that use emission-line ratios will be biased in a qualitatively similar fashion to the star formation dilution affecting BPT and VO87 selection. The widely-used “mass-excitation” (MEx, Juneau et al. 2011) and “color-excitation” (CEx, Yan et al. 2011) methods, which retain $[\text{OIII}]/\text{H}\beta$ but replace the $[\text{NII}]/\text{H}\alpha$ or $[\text{SII}]/\text{H}\alpha$ line ratios with stellar mass or color, will have similar (though more explicit) biases against identifying AGNs in blue and low-mass galaxies. The CEx method is likely to be more affected by lower-metallicity AGN NLRs than MEx AGN selection, since lower metallicity makes a galaxy bluer without changing its mass.

Line ratios with higher contrast between AGNs and HII regions are likely to be less affected by star formation dilution. High-ionization lines such as $[\text{NeV}]$ or HeII and (semi-)permitted lines such as CIII or CIV are likely to result in less biased AGN selection since the AGN NLR typically has harder ionization and higher density than HII regions. Among ratios of strong lines, it is possible that the $[\text{NeIII}]/[\text{OII}]$ ratio used in the “TBT” method (Trouille et al. 2011) offers better diagnostic power for AGN selection since $[\text{NeIII}]$ has a critical density ~ 10 times higher than $[\text{OII}]$. However there are many modes of $[\text{NeIII}]$ emission in galaxies, most of which are not well understood (Zeimann et al. 2015). Spatially-resolved line ratios also result in higher contrast between extended star formation and a nuclear AGN, potentially revealing SMBH accretion even when HII regions dominate the integrated emission lines (e.g., Wright et al. 2010; Trump et al. 2011b).

6.2. AGN Contribution to Emission Lines

The main goal of this work has been to characterize the population of emission-line AGN, including those hidden by star formation dilution. But by definition, the presence of significant dilution means that HII regions dominate the observed emission lines over AGN NLR emission. Many of the AGNs identified in this work have little effect on the emission lines from the point of view of characterizing galaxy properties (such as star formation rate or gas-phase metallicity).

We use the “non-uniform $L_{\text{bol}}/L_{\text{Edd}}$ ” model of Section 5.3 to measure the typical AGN contribution to the observed $\text{H}\alpha$ and $[\text{OIII}]$ emission lines. Quantifying AGN luminosity is simpler than inferring the Eddington ratio or black hole occupation function, since AGN luminosity is directly related to AGN detection above the HII region emission. The assumed M_{BH} distribution does not actually matter for determining the typical AGN luminosity: for example, a lower black hole occupation would simply require an accordingly higher Eddington ratio normal-

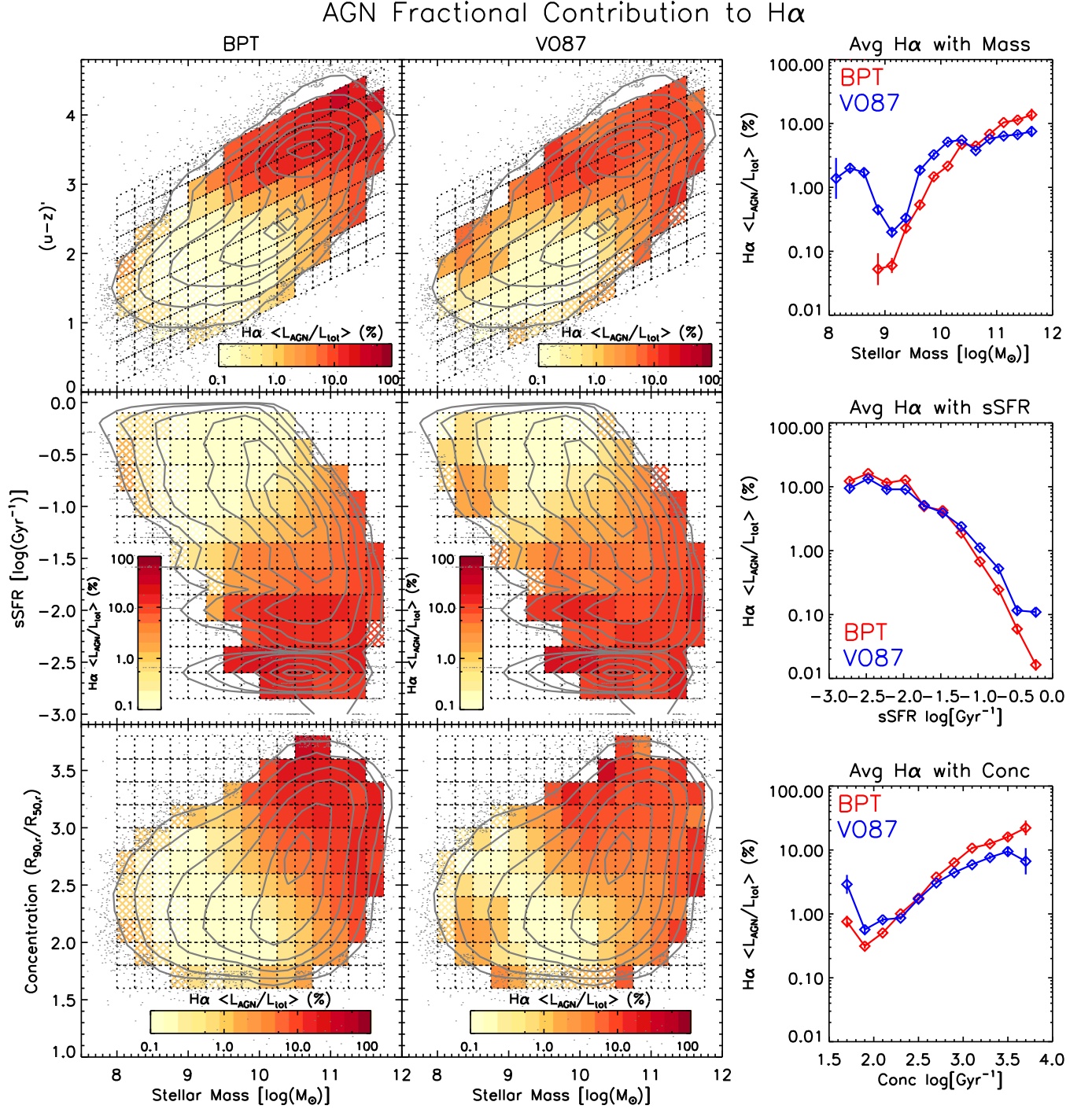


FIG. 24.— The average fraction of H α line emission coming from AGNs in bins of galaxy color-mass, sSFR-mass, and concentration-mass. In the left and center panels, gray contours show the full parent sample of galaxies, and bin shading represents the average AGN contribution. The right panels show the weighted-average AGN contribution with stellar mass, sSFR, and concentration, weighting by the Monte Carlo error in each bin and excluding upper limits. The AGN fraction of H α emission is highest (up to 15%) in massive red/quiescent galaxies, and is lowest ($<1\%$) in low-mass blue/star-forming galaxies. In most galaxies, AGNs contribute $\lesssim 10\%$ to the total H α emission.

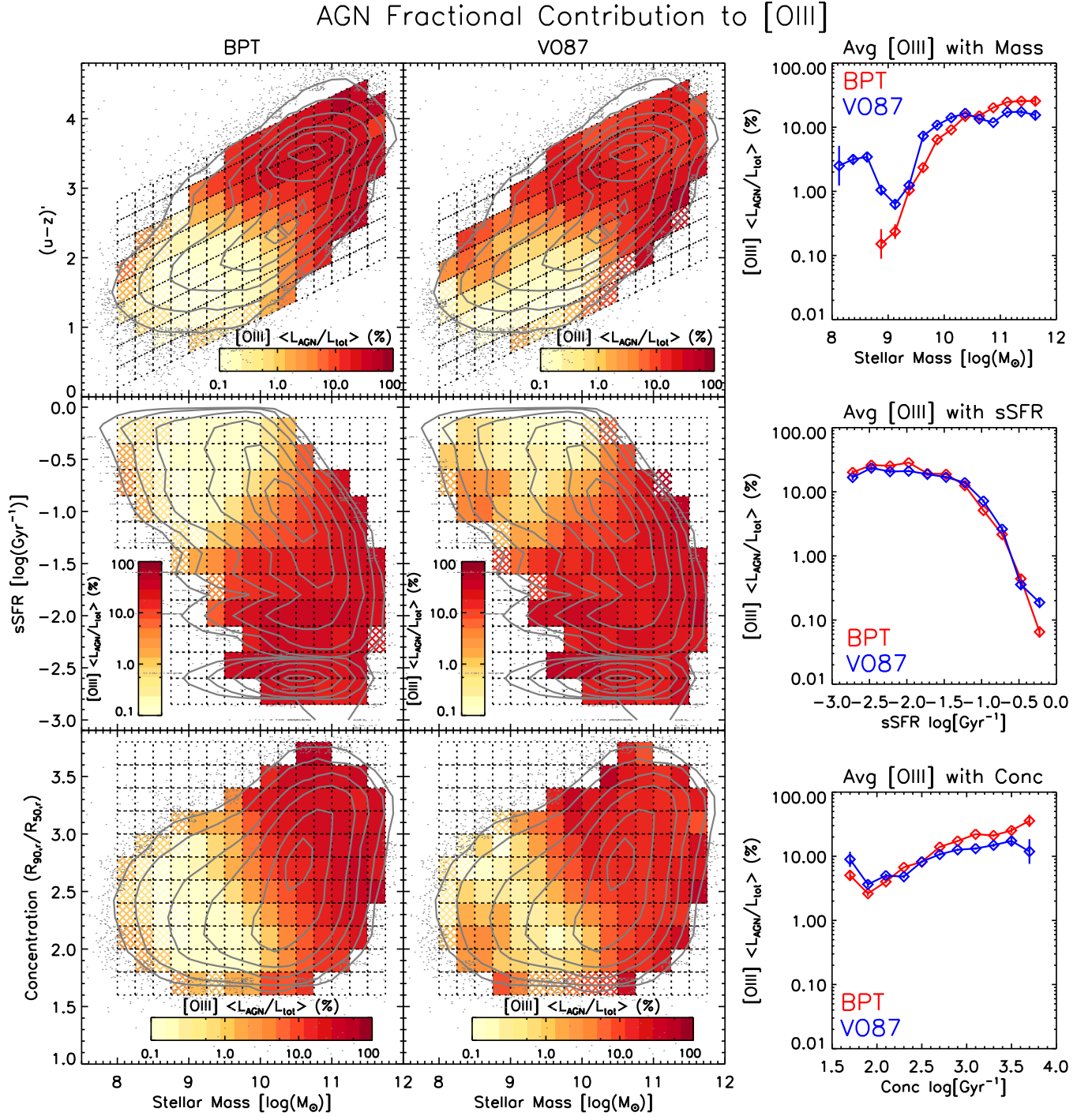


FIG. 25.— The weighted-average fractional AGN contribution to the total [OIII] emission in galaxies binned by color-mass, sSFR-mass, and concentration-mass. As in Figure 24, the averages in the right panels are weighted by the Monte Carlo errors in each bin excluding upper limits. AGNs are a significant portion (~ 20 – 30%) of the average [OIII] emission in massive red galaxies with low sSFR and high concentration, suggesting that the [OIII] line is not a good indicator of galaxy properties in such systems.

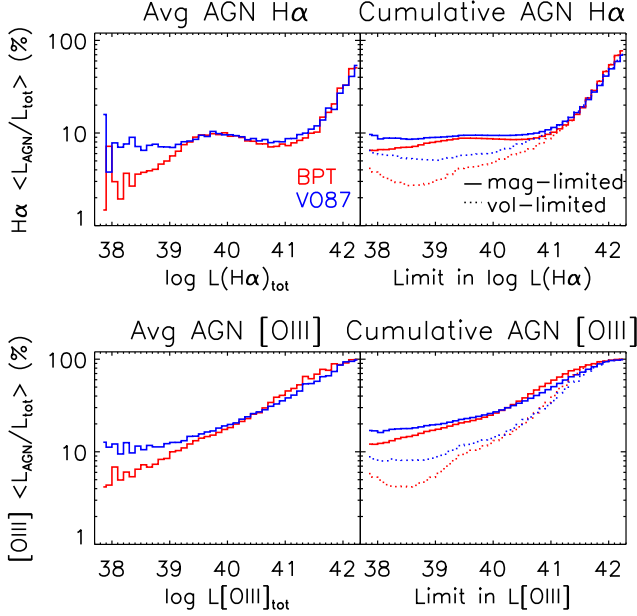


FIG. 26.— The average fractional AGN contribution to $H\alpha$ (top panels) and $[OIII]$ (bottom panels), as a function of total line luminosity (left panels) and limiting line luminosity (right panels). We account for the line-flux limit of the SDSS in the right panels, with the solid line describing the AGN fraction for the magnitude-limited ($r < 17.77$) SDSS and the dotted line using $1/V_{\max}$ weighting to estimate the AGN fraction for a volume-limited survey. As in Figure 24, the AGN contribution to $H\alpha$ is small ($\lesssim 10\%$) in most galaxies, and only luminous ($L(H\alpha) > 10^{42}$ erg s $^{-1}$) galaxies are AGN-dominated. In contrast, the AGN contribution to $[OIII]$ is significant (10–20%) even in weak-lined galaxies and magnitude-limited surveys, and galaxies with $L([OIII]) > 10^{41}$ erg s $^{-1}$ are dominated by AGNs in $[OIII]$ emission.

ization to maintain the same number of detected AGNs.

The fractional AGN contributions to the $H\alpha$ and $[OIII]$ emission lines are shown in Figures 24 and 25, respectively. Both the BPT and VO87 AGN selection methods result in similar estimates of AGN emission-line fractions. The average AGN contribution is highest in massive, low-sSFR, concentrated galaxies, but is $\lesssim 15\%$ in all galaxies. The low average AGN contribution to most galaxies’ $H\alpha$ emission suggests that, for example, $H\alpha$ -derived star formation rates are generally unbiased by AGN emission in similar low-redshift galaxy samples. Meanwhile AGNs contribute a significant fraction (~ 10 – 30%) of the overall $[OIII]$ emission in massive, low-sSFR, concentrated galaxies. In low-mass, high-sSFR, and low-concentration galaxies the AGN fraction of both $H\alpha$ and $[OIII]$ emission is negligible ($\lesssim 1\%$), matching our conclusion that such galaxies have the largest amount of star formation dilution.

We also measure the fractional AGN contribution as a function of line luminosity, shown in the left panels of Figure 26. The right panels of Figure 26 present the average emission-line fraction of AGNs for galaxies above a given line luminosity limit, useful for estimating the typical AGN contribution in emission-line surveys. Each cumulative AGN fraction is limited to the redshift range at which the the SDSS flux limit (1×10^{-16} erg s $^{-1}$ cm $^{-2}$) is above the luminosity limit. The solid line is appropriate for the magnitude-limited ($r < 17.77$) SDSS, while the dotted line shows AGN fractions weighted by the

inverse maximum detection volume, $1/V_{\max}$ (calculated following Hogg 1999), giving the AGN fraction for a volume-limited survey. The larger number of low-mass galaxies (which tend to be star-forming and metal-poor) in volume-limited surveys leads to typically lower AGN fractions compared to magnitude-limited surveys. In general AGNs are an insignificant contribution to $H\alpha$ in all but the most luminous ($L(H\alpha) \gtrsim 10^{41}$ erg s $^{-1}$) galaxies and shallowest surveys. However, AGNs are a significant fraction of a galaxy’s $[OIII]$ emission even in low-luminosity galaxies and deep magnitude-limited surveys, and AGNs dominate galaxy emission at line luminosities of $L([OIII]) \gtrsim 10^{41}$ erg s $^{-1}$.

6.3. AGN Fueling

Section 5 demonstrated that the Eddington ratio distributions implied by both BPT and VO87 AGNs is not uniform across all galaxy properties. At high mass ($\log(M_*/M_\odot) \gtrsim 10$), Section 5.3 and Figure 18 indicated that AGN accretion is connected to specific star formation rate, and otherwise has no dependence on stellar mass. Here we agree with Aird et al. (2012), who found a uniform Eddington ratio distribution with stellar mass for X-ray AGN hosts, along with a moderate enhancement of AGN activity with blue galaxy color. The slope of unity we derive for the $L_{\text{bol}}/L_{\text{Edd}} - \text{sSFR}$ correlation at $\log(\text{sSFR}) < -1.5$ Gyr $^{-1}$ is very similar to that of Mullaney et al. (2012) for X-ray AGN hosts. We also find that the correlation flattens at $\log(\text{sSFR}) > -1.5$ Gyr $^{-1}$. This might be caused by AGN contamination affecting the estimated sSFR at the highest AGN accretion rates. It is also possible that, as suggested by Rosario et al. (2013b) and Azadi et al. (2015), AGNs prefer hosts on the “star-forming mass sequence” but are otherwise uncorrelated with star-forming excess.

Our estimates of the Eddington ratio distribution are less robust at $\log(M_*/M_\odot) \lesssim 10$, since these galaxies have less reliable velocity dispersion measurements used to estimate M_{BH} . Thus we cannot confidently claim any non-uniformity in AGN accretion at low stellar masses. In the Appendix we do, however, find that the observed BPT and VO87 AGN fractions are much better described by the Gültekin et al. (2009) $M_{\text{BH}} - \sigma$ relation than by a constant M_{BH}/M_* ratio. In a galaxy of given sSFR, Eddington ratio seems to be uniform no matter the bulge fraction, but galaxies with smaller bulges tend to have smaller black holes. This contradicts the constant M_{BH}/M_* ratio used by Aird et al. (2012), although some high-redshift observations suggest an evolving $M_{\text{BH}}/M_{\text{bulge}}$ but a constant M_{BH}/M_* fraction (e.g., Jahnke et al. 2009; Schramm & Silverman 2013; Sun et al. 2015).

6.4. AGN Feedback

The high energy output of AGNs suggests the potential for powerful feedback to quench host galaxy star formation. Such feedback could occur either through blowout of the star-forming gas by radiatively-driven winds (Silk & Rees 1998; Fabian 2002; Di Matteo, Springel, & Hernquist 2005), or by radio jets mechanically heating the gas (Croton et al. 2006). The feedback mode likely depends on Eddington ratio, with powerful radiative winds likely only at high accretion

rates and jets dominating the outflows of weakly accreting AGNs (Narayan & McClintock 2008; Ho 2008; Trump et al. 2011a; Heckman & Best 2014). But in general both feedback modes are likely to increase with AGN luminosity.

We define “feedback timescale” as the ratio of a galaxy’s gravitational binding energy to the AGN bolometric luminosity, $\tau_{\text{fb}} = U_{\text{gal}}/L_{\text{AGN}}$. The inverse of this timescale τ_{fb}^{-1} quantifies the efficiency of AGN feedback:

$$\tau_{\text{fb}}^{-1} \simeq 40 \frac{L_{42} R_{10}}{M_{10}^2} \text{ Gyr}^{-1}. \quad (17)$$

Here $L_{42} = L_{\text{AGN}}/(10^{42} \text{ erg s}^{-1})$, $R_{10} = R_{50}/(10 \text{ kpc})$, and $M_{10} = M_*/(10^{10} M_{\odot})$. Very roughly, at a fixed Eddington ratio and fixed black hole occupation defined by $M_{\text{BH}} \sim \sigma^4$, $L_{\text{AGN}} \sim (L_{\text{bol}}/L_{\text{Edd}}) M_{\text{BH}} \sigma^4 \sim (f_b M_*)^2$ (where f_b is the bulge-to-total ratio). Meanwhile, galaxy mass and size are correlated as $M \sim R^{\alpha}$, with $0.15 < \alpha < 0.55$ increasing from low-mass disks to high-mass ellipticals (Shen et al. 2003). For a uniform Eddington ratio distribution this means that AGN feedback efficiency increases with bulge fraction and stellar mass, $\tau_{\text{fb}} \sim f_b^2 M_*^{\alpha}$. Of course, the actual situation is somewhat more complicated, as Sections 5 and 6 showed that the Eddington ratio distribution is not uniform.

We use the “non-uniform $L_{\text{bol}}/L_{\text{Edd}}$ ” simulation of Section 5.3 to estimate the AGN feedback efficiency τ_{fb}^{-1} across galaxy properties. Just as in Section 6.2, the details of the M_{BH} distribution do not matter, since AGN luminosity (with respect to the empirically measured star formation dilution) is directly constrained by the observed AGN fraction. Our feedback estimates depend only on the assumed $L_{\text{bol}}/L[\text{OIII}]$ bolometric correction and “pure AGN” line ratios.

Figure 27 shows the average AGN feedback efficiency $\tau_{\text{fb}}^{-1} = L_{\text{AGN}}/U_{\text{gal}}$ in bins of galaxy color–mass, sSFR–mass, and concentration–mass. In each bin the feedback efficiency is averaged over the Eddington ratio distribution (which has a declining power-law slope $\alpha = 0.6$), with a small number of high- $L_{\text{bol}}/L_{\text{Edd}}$ AGNs and a large population of weakly-accreting AGNs. There are slight differences in the feedback inferred from the observed BPT and VO87 AGN populations, largely at low masses and high sSFR where the BPT selection results in upper limits due to the heavy bias. By either method there is little connection between the average AGN feedback efficiency and galaxy properties at $z < 0.1$: feedback by typical AGNs is likely to operate just as efficiently in low-mass and high-mass galaxies. The uniformity of τ_{fb}^{-1} at high and low sSFR also implies that feedback from line-ratio AGNs is not the dominant mode of star formation quenching in most galaxies of any mass or morphology. This is in agreement with recent simulations showing that AGN winds, even when present at high velocity, have little effect on the larger gas reservoirs within their host galaxies (Gabor & Bournaud 2014; Roos et al. 2015).

6.5. Black Hole Seeds

The SMBH occupation function in low-redshift galaxies carries an imprint of the initial seeding mechanism in the early universe. In particular, low-mass

($\lesssim 150 M_{\odot}$) SMBH seeds from Pop III remnants are likely to be common in most early halos, while massive (10^4 – $10^6 M_{\odot}$) seeds from direct collapse are rare in low-mass halos due to their higher spin parameter (Begelman et al. 2006; Volonteri & Natarajan 2009; van Wassenhove et al. 2010). Subsequent accretion and mergers of these seeds is thought to eventually form the local $M_{\text{BH}} - \sigma$ correlation (e.g., Volonteri & Stark 2011; Volonteri 2012). Due to the high direct-collapse seeding rate and high merger rate, essentially every massive galaxy is likely to end up on the $M_{\text{BH}} - \sigma$ relation. Both the merger rate and the fraction of massive seeds are thought to be lower for low-mass ($\log(M_*/M_{\odot}) \lesssim 10$) hosts, and so many of these galaxies may have under-massive black holes compared to the $M_{\text{BH}} - \sigma$ relation.

We determine the “SMBH occupation function” as the fraction of galaxies with black hole masses well-described by the $M_{\text{BH}} - \sigma$ relation. Our galaxies are assumed to contain a bimodal population of black holes, with one peak of massive seeds described by the Gültekin et al. (2009) $M_{\text{BH}} - \sigma$ relation (Equation 8), and a second log-normal distribution of lower-mass Pop III seeds centered at $150 M_{\odot} \pm 0.5 \text{ dex}$. From this distribution the SMBH occupation function is fit using a simulation similar to that in Section 5.4, with the same bolometric correction (Equation 9), metallicity-dependent NLR (Equations 10–13), and sSFR-dependent Eddington ratio distribution (Equations 14 and 15), while using the bimodal distribution for M_{BH} . From this distribution, the SMBH occupation function is described by the fraction of galaxies hosting black holes drawn from the higher-mass $M_{\text{BH}} - \sigma$ peak.

Figure 28 shows the SMBH occupation function from our model fits to the observed BPT and VO87 AGN fractions. There are some differences between the two selection methods, likely due to the uncertainties associated with NLR metallicity in low-mass galaxies. In addition, the velocity dispersions in $\log(M_*/M_{\odot}) \lesssim 10$ galaxies are poorly understood, due to both the low SDSS resolution ($\sim 70 \text{ km/s}$) and the difficulty in interpretation (bulges versus disordered disks). Nonetheless both the BPT and VO87 AGN fractions imply a slightly lower black hole occupation of ~ 30 – 50% in low-mass and disk-dominated hosts. This result is roughly consistent with the independent study of Miller et al. (2015), who similarly found a marginally lower SMBH occupation function of a few tens of percent for $\log(M_*/M_{\odot}) \lesssim 10$ X-ray AGN hosts. Confirming this marginal evidence and robustly determining the SMBH black hole occupation function at low stellar mass requires higher resolution spectroscopy than available from our SDSS sample.

7. SUMMARY

We constructed a sample of over 300,000 galaxies from the Sloan Digital Sky Survey to investigate the biases of line-ratio AGN selection and recover the intrinsic AGN population across a range of galaxy properties. While line-ratio AGNs are observed to be most common in massive green-valley hosts, we demonstrated that this result is a selection effect caused by the bias from “star formation dilution” in low-mass and star-forming galaxies. After accounting for this bias, we find that AGNs are most common in massive galaxies with high specific star formation rates, implying that SMBH accretion and star

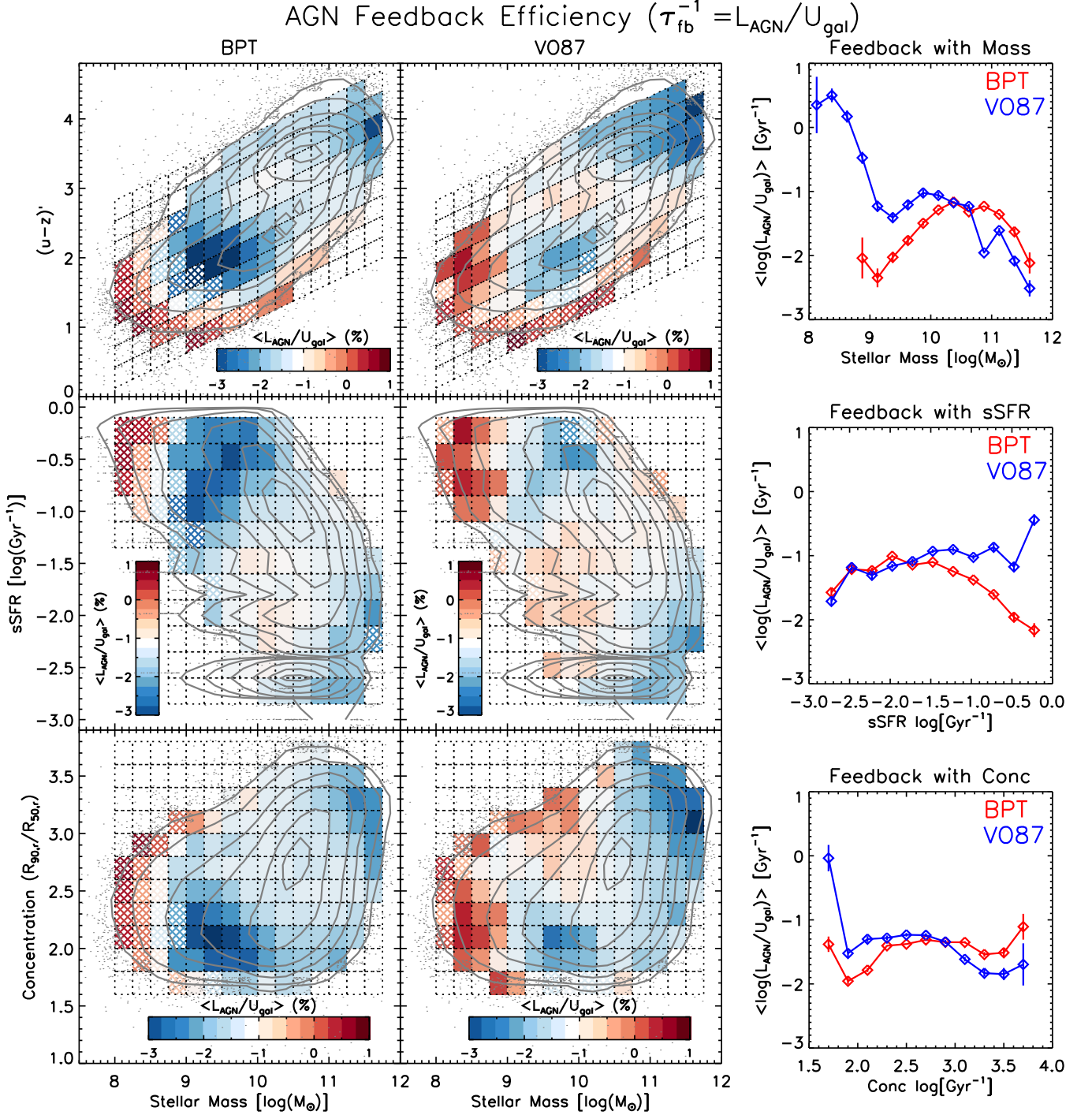


FIG. 27.— The average AGN feedback efficiency $\tau_{\text{fb}}^{-1} = L_{\text{AGN}}/U_{\text{gal}}$ with galaxy color–mass, sSFR–mass, and concentration–mass, inferred by both the BPT and VO87 AGN selection. The average feedback efficiency is given by the bin shading in the left and center panels, with the full parent sample of galaxies shown by gray contours. The feedback efficiency is shown with stellar mass, sSFR, and concentration in the right panels, computed as weighted averages using the Monte Carlo error in each bin and excluding upper limits. AGN feedback efficiency is fairly uniform with galaxy properties, with no evidence that AGNs dominate the quenching of star formation for most galaxies of any type.

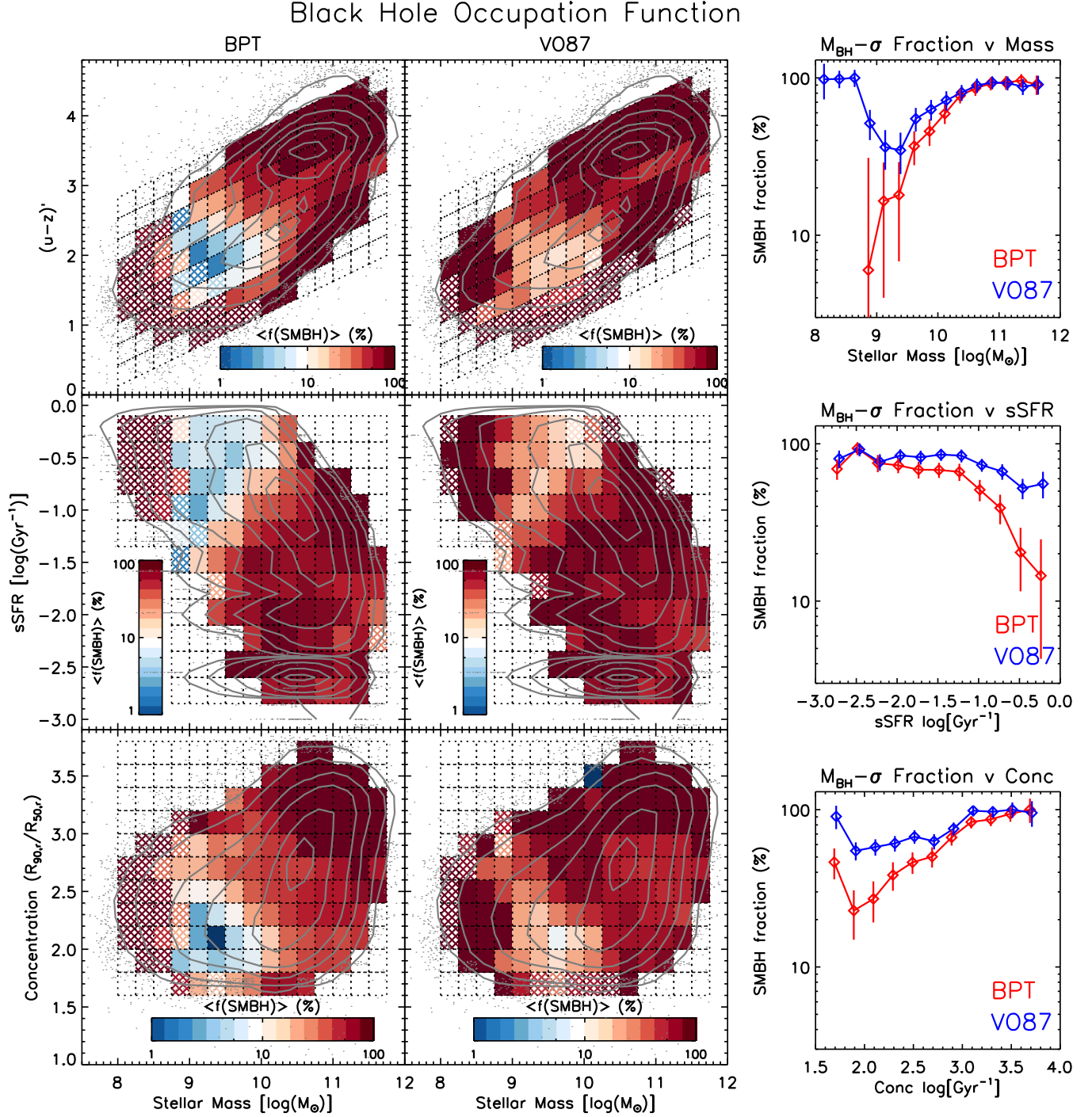


FIG. 28.— The SMBH occupation function derived from our model fit to the observed BPT AGN and V087 AGN fractions. Here we assume that the black hole population is bimodal with two log-normal peaks, one from Pop III star remnants at $150M_\odot$ (with ± 0.5 dex scatter) and one from massive seed “fossils” described by the Gültekin et al. (2009) $M_{\text{BH}}-\sigma$ relation (Equation 14). With the caveat that σ may be inaccurate (in both measurement and interpretation as bulge kinematics) in our low-mass galaxies, there is some hint of a lower SMBH occupation function in $\log(M_*/M_\odot) \lesssim 10$ hosts.

formation are fueled by the same gas reservoir. AGNs contribute little to the overall $H\alpha$ and $[OIII]$ emission lines in low-mass galaxies, but their feedback effects are likely to be just as efficient at all stellar masses and host morphologies. There is marginal evidence that the black hole occupation function may be a factor of a few lower in $\log(M_*/M_\odot) \lesssim 10$ hosts, although this result is not robust due to poorly-understood velocity dispersions in these galaxies. Higher resolution spectroscopy is needed to better constrain SMBH occupation function, while selection methods via spatially resolved line ratios or high-ionization lines suffer less bias and can better reveal the connection between AGN accretion and star formation.

We thank Jenny Greene and Renbin Yan for valuable discussions which contributed to this work. JRT

REFERENCES

- Ahn, C. P., Alexandroff, R., Allende Prieto, C. et al. 2014, *ApJS*, 211, 17
- Aird, J., Coil, A., Moustakas, J. et al. 2012, *ApJ*, 746, 90
- Azadi, M., Aird, J., Coil, A. L. et al. 2015, *ApJ*, 806, 187
- Baldwin, J. A., Phillips, M. M. & Terlevich, R. 1981, *PASP*, 93, 5
- Begelman, M. C., Volonteri, M. & Rees, M. J. 2006, *MNRAS*, 370, 289
- Bennert, N., Falcke, H., Schulz, H., Wilson, A. S. & Wills, B. J. 2002, *ApJ*, 574, 105
- Best, P. N., Kauffmann, G., Heckman, T. M., Brinchmann, J., Charlot, S., Ivezić, Ž. & White, S. D. M. 2005, *MNRAS*, 362, 25
- Blanton, M. R., Dalcanton, J., Eisenstein, D. et al. 2001, *AJ*, 121, 2358
- Blanton, M. R. & Roweis, S. 2007, *AJ*, 133, 734
- Bolton, A. S., Schlegel, D. J., Aubourg, E. et al. 2012, *AJ*, 144, 144
- Bongiorno, A., Merloni, A., Brusa, M. et al. 2012, *MNRAS*, 427, 3103
- Bournaud, F., Dekel, A., Teyssier, R., Cacciato, M., Daddi, E., Juneau, S. & Shankar, F. 2011, *ApJ*, 741, 33
- Bournaud, F., Juneau, S., Le Floch, E. et al. 2012, *ApJ*, 757, 81
- Brinchmann, J., Pettini, M. & Charlot, S. 2008, *MNRAS*, 385, 769
- Bromm, V. & Loeb, A. 2003, *ApJ*, 596, 34
- Calzetti, D., Armus, L., Bohlin, R. C., Kinney, A. L., Koornneef, J. & Storchi-Bergmann, T., 2000, *ApJ*, 533, 682
- Cameron, E. 2011, *PASA*, 28, 128
- Cappellari, M., Bacon, R., Bureau, M. et al. 2006, *MNRAS*, 366, 1126
- Cardelli, J. A., Clayton, G. C. & Mathis, J. S. 1989, *ApJ*, 345, 245
- Charlot, S. & Fall, S. M. 2000, *ApJ*, 539, 718
- Chen, C.-T. J., Hickox, R. C., Alberts, S. et al. 2013, *ApJ*, 773, 3
- Cisternas, M., Jahnke, K., Bongiorno, A. et al. 2011, *ApJ*, 741, 11
- Coil, A. L., Aird, J., Reddy, N. et al. 2015, 2015, *ApJ*, 801, 35
- Conroy, C., Gunn, J. E. & White, M. 2009, *ApJ*, 699, 486
- Croton, D. J., Springel, V., White, S. D. M. et al. 2006, *MNRAS*, 365, 11
- Cucciati, O., Tresse, L., Ilbert, O. et al. 2012, *A&A*, 539, 31
- Dekel, A., Birnboim, Y., Engel, G. et al. 2009, *Nature*, 457, 451
- Di Matteo, T., Springel, V., & Hernquist, L. 2005, *Nature*, 433, 604
- Ellison, S. L., Mendel, J. T., Scudder, J. M., Patton, D. R. & Palmer, M. J. D. 2011, *MNRAS*, 430, 3128
- Fabian, A. C. 2002, *MNRAS*, 308, 39
- Feigelson, E. D. & Nelson, P. I. 1985, *ApJ*, 293, 192
- Ferrarese, L. & Merritt, D. 2000, *ApJ*, 593, 9
- Fryer, C. L., Woosley, S. E. & Heger, A. 2001, *ApJ*, 550, 372
- Fukugita, M., Ichikawa, T., Gunn, J. E., Doi, M., Shimasaku, K. & Schneider, D. P. 1996, *AJ*, 111, 1748
- Gabor, J. M., Impey, C. D., Jahnke, K. et al. 2009, *ApJ*, 691, 705
- Gabor, J. M. & Bournaud, F. 2013, *MNRAS*, 434, 606
- Gabor, J. M. & Bournaud, F. 2014, *MNRAS*, 441, 1615
- Gebhardt, K., Bender, R., Bower, G. et al. 2000, *ApJ*, 539, 13
- Georgakakis, A., Nandra, K., Yan, R. et al. 2008, *MNRAS*, 385, 2049
- Greene, J. E., Peng, C. Y., Kim, M., Kuo, C.-Y., Braatz, J. A., Impellizzeri, C. M. V., Condon, J. J., Lo, K. Y., Henkel, C. & Reid, M. J. et al. 2010, *ApJ*, 721, 26
- Grogin, N. A., Conselice, C. J., Chatzichristou, E. et al. 2005, *ApJ*, 627, 97
- Groves, B. A., Dopita, M. A. & Sutherland, R. S. 2004, *ApJS*, 153, 75
- Gültekin, K., Richstone, D. O., Gebhardt, K. et al. 2009, *ApJ*, 698, 198
- Gunn, J. E., Siegmund, W. A., Mannery, Edward J. et al. 2006, *AJ*, 131, 2332
- Haggard, D., Green, P. J., Anderson, S. F., Constantin, A., Aldcroft, T. L., Kim, D.-W. & Barkhouse, W. A. 2010, *ApJ*, 723, 1447
- Häring, N. & Rix, H.-W. 2004, *ApJ*, 604, 89
- Harrison, C. M., Alexander, D. M., Mullaney, J. R. et al. 2012, *ApJ*, 760, 15
- Heckman, T. M. 1980, *A&A*, 87, 152
- Heckman, T. M., Kauffmann, G., Brinchmann, J., Charlot, S., Tremonti, C. & White, S. D. M. 2004, *ApJ*, 613, 109
- Heckman, T. & Best, P. 2014, *ARA&A*, 52, 589
- Hickox, R. C., Jones, C., Forman, W. R. et al. 2009, *ApJ*, 696, 891
- Hickox, R. C., Mullaney, J. R., Alexander, D. M., Chen, C.-T. J., Civano, F. M., Goulding, A. D. & Hainline, K. N., 2014, *ApJ*, 782, 9
- Ho, L. C., Filippenko, A. V. & Sargent, W. L. W. 2003, *ApJ*, 583, 159
- Ho, L. C. 2008, *ARA&A*, 46, 475
- Ho, L. C. 2009, *ApJ*, 699, 626
- Hogg, D. W. 1999, *arXiv:990.5116*
- Hopkins, P. F., Hernquist, L., Cox, T. J., DiMatteo, T., Robertson, B. & Springel, V. 2008, *ApJS*, 175, 356
- Hopkins, P. F., Hernquist, L., Cox, T. J. & Keres, D. 2008, *ApJS*, 175, 356
- Hopkins, P. F. & Hernquist, L. 2009, *ApJ*, 698, 1550
- Hopkins, P. F., Kocevski, D. D. & Bundy, K. 2014, *MNRAS*, 445, 823
- Jahnke, K., Bongiorno, A., Brusa, M. et al. 2009, *ApJ*, 706, 215
- Johnson, J. L., Whalen, D. J., Fryer, C. L. & Li, H. 2012, *ApJ*, 750, 66
- Juarez, Y., Maiolino, R., Mujica, R., Pedani, M., Marinoni, S., Nagao, T., Marconi, A. & Oliva, E. 2009, *A&A*, 494, 25
- Juneau, S., Dickinson, M., Alexander, D. M. & Salim, S. 2011, *ApJ*, 736, 104
- Juneau, S., Dickinson, M., Bournaud, F. et al. 2013, *ApJ*, 764, 176
- Juneau, S., Bournaud, F., Charlot, S. et al. 2014, *ApJ*, 788, 88
- Kassin, S. A., Weiner, B. J., Faber, S. M. et al. 2012, *ApJ*, 758, 106
- Kauffmann, G., Heckman, T. M., Tremonti, C. et al. 2003b, *MNRAS*, 346, 1055
- Kauffmann, G. & Heckman, T. M. 2009, *MNRAS*, 397, 135
- Kelly, B. C., Vestergaard, M., Fan, X., Hopkins, P., Hernquist, L. & Siemiginowska, A. 2010, *ApJ*, 719, 1315
- Kewley, L. J., Dopita, M. A., Sutherland, R. S., Heisler, C. A. & Trevena, J. 2006, *MNRAS*, 372, 961

- Kewley, L. J., Groves, B., Kauffmann, G. & Heckman, T. 2006, MNRAS, 372, 961
- Kewley, L. J., Dopita, M. A., Leitherer, C., Davé, R., Yuan, T., Allen, M., Groves, B. & Sutherland, R. 2013, ApJ, 774, 100
- Kocevski, D. D., Lubin, L. M., Lemaux, B. C., Gal, R. R., Fassnacht, C. D., Lin, R. & Squires, G. K. 2009, ApJ, 700, 901
- Kocevski, D. D., Faber, S. M., Mozena, M. et al. 2012, ApJ, 744, 148
- Kormendy, J. & Ho, L. C. 2013, ARA&A, 51, 511
- Koss, M., Mushotzky, R., Veilleux, S. & Winter, L. 2010, ApJ, 716, 125
- Kroupa, P. 2001, MNRAS, 322, 231
- Lamastra, A., Bianchi, S., Matt, G., Perola, G. C., Barcons, X. & Carrera, F. J. 2009, A&A, 504, 73
- Liu, X., Shapley, A. E., Coil, A. L., Brinchmann, J. & Ma, C.-P. 2008, ApJ, 678, 758
- Madau, P. & Rees, M. J. 2001, ApJ, 551, 27
- Madau, P. & Dickinson, M. 2014, ARA&A, 52, 415
- Magorrian, J., Tremaine, S., Richstone, D. et al. 1998, AJ, 115, 2285
- Marconi, A. & Hunt, L. K. 2003, ApJ, 589, 21
- Matsuoka, K., Nagao, T., Marconi, A., Maiolino, R. & Taniguchi, Y. 2011, A&A, 527, 100
- Matsuoka, Y., Strauss, M. A., Price, T. N., III, DiDonato, M. S. 2014, ApJ, 780, 162
- Miller, B. P., Gallo, E., Greene, J. E., Kelly, B. C., Treu, T., Woo, J.-H. & Baldassare, V. 2015, ApJ, 799, 98
- Montero-Dorta, A. D. et al. in prep.
- Moran, E. C., Filippenko, A. V. & Chornock, R. 2002, ApJ, 579, 71
- Mullaney, J. R., Daddi, E., Béthermin, M. et al. 2012, ApJ, 753, 30
- Nagao, T., Marconi, A. & Maiolino, R. 2006, A&A, 447, 157
- Nandra, K., Georgakakis, A., Willmer, C. N. A., Cooper, M. C., Croton, D. J., Davis, M., Faber, S. M., Koo, D. C., Laird, E. S. & Newman, J. A. 2007, ApJ, 660, 11
- Narayan, R. & McClintock, J. E. 2008, NewAr, 51, 733
- O'Donnell, J. E. 1994, ApJ, 422, 158
- Osterbrock, D. E. & Ferland, G. J. 2006, Astrophysics of Gaseous Nebulae and Active Galactic Nuclei, 2nd. ed., Sausalito, CA: University Science Books
- Petrosian, V. 1976, ApJ, 209, 1
- Prugniel, P. & Soubiran, C. 2001, A&A, 369, 1048
- Richardson, C. T., Allen, J. T., Baldwin, J. A., Hewett, P. C. & Ferland, G. J. 2014, MNRAS, 437, 2376
- Roos, O., Juneau, S., Bournaud, F. & Gabor, J. M. 2015, ApJ, 800, 19
- Rosario, D. J., Santini, P., Lutz, D. et al. 2013, ApJ, 771, 63
- Rosario, D. J., Trakhtenbrot, B., Lutz, D. et al. 2013, A&A, 560, 72
- Salim, S. Rich, R. M., Charlot, S. et al. 2007, ApJS, 173, 267
- Sánchez, S. F., Rosales-Ortega, F. F., Iglesias-Páramo, J. et al. 2014, A&A, 563, 49
- Sánchez, S. F., Pérez, E., Rosales-Ortega, F. F. et al. 2015, A&A, 574, 47
- Sanders, D. B., Soifer, B. T., Elias, J. H., Madore, B. F., Matthews, K., Neugebauer, G. & Scoville, N. Z. 1988, ApJ, 325, 74
- Schawinski, K., Virani, S., Simmons, B., Urry, C. M., Treister, E., Kaviraj, S. & Kushkuley, B. 2009, ApJ, 692, 19
- Schawinski, K., Urry, C. M., Virani, S. et al. 2010, ApJ, 711, 284
- Schramm, M. & Silverman, J. D. 2013, ApJ, 767, 13
- Shapley, A. E., Reddy, N. A., Kriek, M. et al. 2015, ApJ, 801, 88
- Shen, S., Mo, H. J., White, S. D. M., Blanton, M. R., Kauffmann, G., Voges, W., Brinkmann, J. & Csabai, I. 2003, MNRAS, 343, 978
- Shlosman, I., Frank, J. & Begelman, M. C. 1989, Nature, 338, 45
- Schulze, A. & Wisotzki, L. 2010, A&A, 516, 87
- Silk, J. & Rees, M. J. 1998, A&A, 331, 1
- Silverman, J. D., Mainieri, V., Lehmer, B. D. et al. 2008, ApJ, 675, 1025
- Silverman, J. D., Lamareille, F., Maier, C. et al. 2009, ApJ, 696, 396
- Smee, S. A., Gunn, J. E., Uomoto, A. et al. 2013, AJ, 146, 32
- Steidel, C. C., Rudie, G. C., Strom, A. L. et al. 2014, ApJ, 795, 165
- Stern, J. & Laor, A. 2012, MNRAS, 426, 2703
- Strauss, M. A., Weinberg, D. H., Lupton, R. H. et al. 2002, AJ, 124, 1810
- Sun, M., Trump, J. R., Brandt, W. N. et al. 2015, ApJ, 802, 14
- Tanaka, M. 2012, PASJ, 64, 37
- Treister, E., Schawinski, K., Urry, C. M. & Simmons, B. D. 2012, ApJ, 758, 39
- Tremonti, C. A., Heckman, T. M., Kauffmann, G. et al. 2004, ApJ, 613, 898
- Trouille, L., Barger, A. J. & Tremonti, C. 2011, ApJ, 742, 46
- Trump, J. R., Impey, C. D., Kelly, B. C. et al. 2011a, ApJ, 733, 60
- Trump, J. R., Weiner, B. J., Scarlata, C. et al. 2011b, ApJ, 743, 144
- Trump, J. R., Hsu, A. D., Fang, J. J. et al. 2013, ApJ, 763, 133
- Trump, J. R. 2013c, Conference Proceedings for Galaxy Mergers in an Evolving Universe (Hualien, Taiwan), ed. Wei-Hsin Sun, Nick Scoville, ASPC, 477, 227
- Trump, J. R., Barro, G., Juneau, S. et al. 2014, ApJ, 793, 101
- van Wassenhove, S., Volonteri, M., Walker, M. G. & Gair, J. R. 2010, MNRAS, 408, 1139
- Veilleux, S. & Osterbrock, D. E. 1987, ApJS, 63, 295
- Volonteri, M. & Natarajan, P. 2009, MNRAS, 400, 1911
- Volonteri, M. & Stark, D. P. 2011, MNRAS, 417, 2085
- Volonteri, M. 2012, Science, 337, 544
- Whitaker, K. E., van Dokkum, P. G., Brammer, G. & Franx, M. 2012, ApJ, 754, 29
- Wild, V., Heckman, T. & Charlot, S. 2010, MNRAS, 405, 933
- Wright, S. A., Larkin, J. E., Graham, J. R. & Ma, C.-P. 2010, ApJ, 711, 1291
- Wyder, T. K., Treyer, M. A., Milliard, B. et al. 2005, ApJ, 619, 15
- Xie, F.-G. & Yuan, F. 2012, MNRAS, 427, 1580
- Xue, Y. Q., Brandt, W. N., Luo, B. et al. 2010, ApJ, 720, 368
- Yan, R., Ho, L. C., Newman, J. A. et al. 2011, ApJ, 728, 38
- Yan, R. & Blanton, M. R. 2012, ApJ, 747, 61
- York, D. G., Adelman, J., Anderson, J. E., Jr. et al. 2000, AJ, 120, 1579
- Zaritsky, D., Kennicutt, R. C., Jr. & Huchra, J. P. 1994, ApJ, 420, 87
- Zeimann, G. R., Ciardullo, R., Gebhardt, H., Gronwall, C., Hagen, A., Trump, J. R., Bridge, J. S., Luo, B. & Schneider, D. P. 2015, ApJ, 798, 29

APPENDIX

TESTING OTHER MODELING ASSUMPTIONS

In this Appendix we justify the modeling assumptions used in the simulations of Section 5 (and outlined in Equations 7–13) by testing other plausible assumptions. The models used the same dust extinction for both HII and AGN NLR emission lines, and we test that assumption here. The original “uniform- $L_{\text{bol}}/L_{\text{Edd}}$ ” simulation is also compared with additional simulations that replace the metallicity-dependent NLR ratios with metal-rich (constant) NLR ratios, or replace the $M_{\text{BH}} - \sigma$ relation with a constant M_{BH}/M_* ratio. We also test different power-law slopes for the Schechter function describing the Eddington ratio distribution.

Dust Corrections

Our estimates of the intrinsic AGN occupation fraction used dust-free emission lines, beginning from dust-corrected emission lines observed for star-forming galaxies, and then adding dust-free model AGN NLR emission lines. Thus the

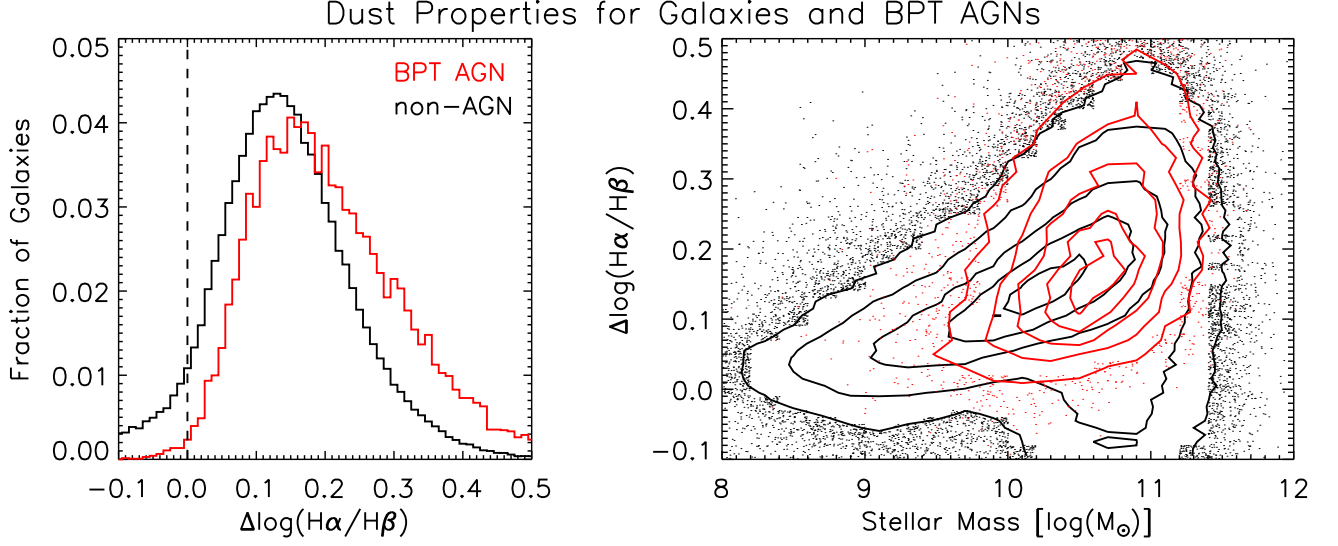


FIG. 29.— The distribution of dust extinction for galaxies classified as BPT AGNs and non-AGNs (SF galaxies and LINERs). We quantify the dust extinction as $\Delta \log(\text{H}\alpha/\text{H}\beta) \equiv \log(\text{H}\alpha/\text{H}\beta)_{\text{obs}} - \log(\text{H}\alpha/\text{H}\beta)_{\text{i}}$, where the intrinsic Balmer decrement $(\text{H}\alpha/\text{H}\beta)_{\text{i}}$ is 3.1 for AGNs and 2.86 for non-AGNs (Osterbrock & Ferland 2006). AGNs have marginally more dust extinction than the full set of non-AGNs (left panel), but this is because BPT AGNs are identified only in massive galaxies. AGNs have nearly identical dust extinction compared to non-AGNs of the same stellar mass (right panel).

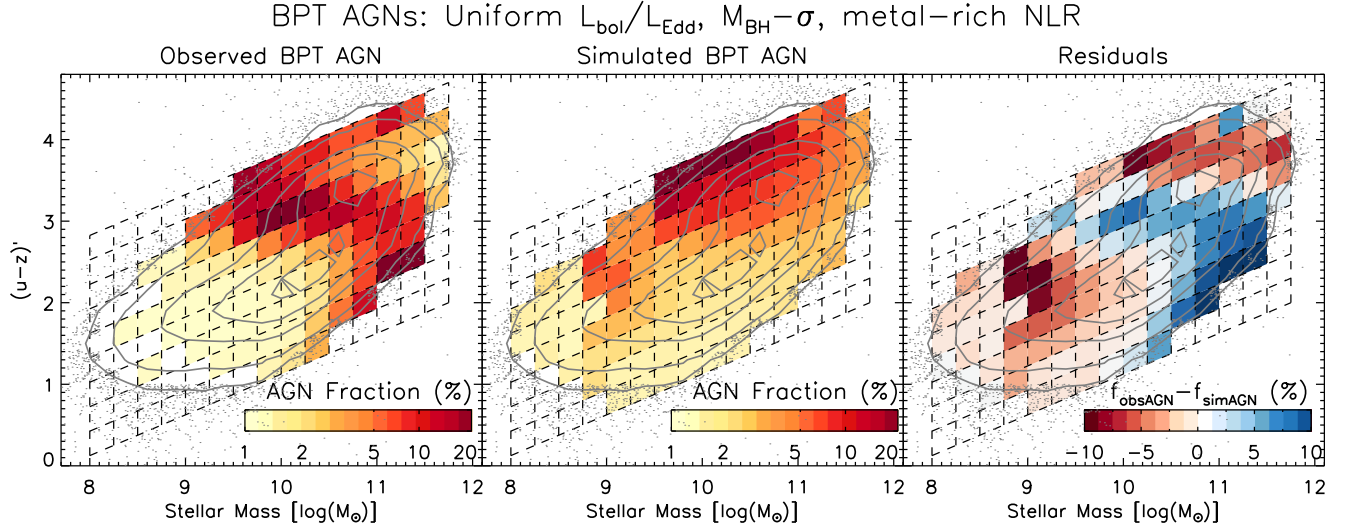


FIG. 30.— The observed and simulated fractions of BPT AGNs with host galaxy color and stellar mass for the “uniform $L_{\text{bol}}/L_{\text{Edd}}$ ” simulation with metal-rich NLR line ratios. Bin shading indicates the AGN fraction and the gray contours represent the distribution of well-measured galaxies. Using a metal-rich NLR results in a larger overprediction of BPT AGNs in low-mass galaxies compared to the metallicity-dependent NLR used in Section 5.2.

TABLE 1
 $\chi^2/1000$ VALUES FOR SIMULATED AGN FRACTIONS

Model	BPT			VO87		
	$(u-z)' - M_*$	sSFR - M_*	$C_r - M_*$	$(u-z)' - M_*$	sSFR - M_*	$C_r - M_*$
Uniform $L_{\text{bol}}/L_{\text{Edd}}$, $M_{\text{BH}} - \sigma$, metal-dependent NLR	12.8	10.7	9.83	2.62	2.32	2.37
Uniform $L_{\text{bol}}/L_{\text{Edd}}$, $M_{\text{BH}} - \sigma$, metal-rich NLR	23.1	19.2	15.7	2.62	2.32	2.37
Uniform $L_{\text{bol}}/L_{\text{Edd}}$, $M_{\text{BH}} - M_*$, metal-rich NLR	46.0	33.2	34.0	4.59	4.34	4.97
Shallow ($\alpha = 0.2$) $L_{\text{bol}}/L_{\text{Edd}}$ distribution	24.5	18.6	16.7	4.59	4.34	4.97
Flat ($\alpha = 0.05$) $L_{\text{bol}}/L_{\text{Edd}}$ distribution	28.2	21.4	18.9	5.48	4.09	4.27

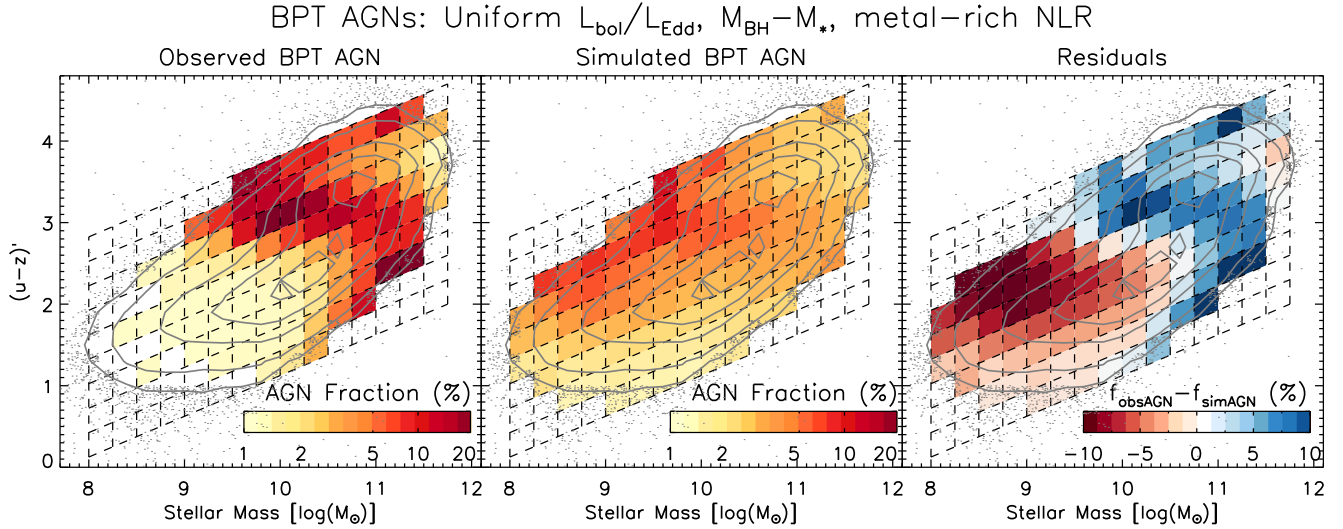


FIG. 31.— The observed and simulated fractions of BPT AGNs with host galaxy color and stellar mass for the “uniform $L_{\text{bol}}/L_{\text{Edd}}$ ” simulation with metal-rich NLR line ratios and a constant M_{BH}/M_* ratio. As before, the AGN fraction is indicated by the bin shading and the well-measured galaxy distribution is given by the gray contours. Assuming a constant M_{BH}/M_* ratio results in a significantly worse match to the observations than the simulation using the $M_{\text{BH}}-\sigma$ relation in Figure 30 (and in Section 5.2).

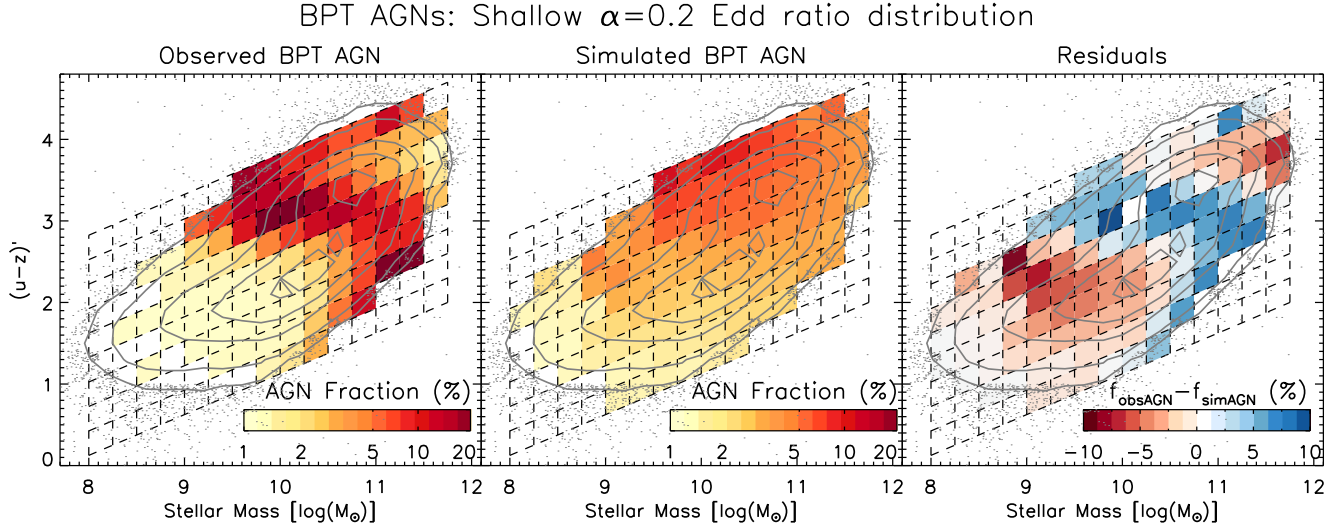


FIG. 32.— A comparison of the observed and simulated BPT AGN fractions in the galaxy color–mass diagram, using a simulation with a “shallow” Eddington ratio distribution of power-law slope $\alpha = 0.2$. The shallow $L_{\text{bol}}/L_{\text{Edd}}$ distribution results in larger residuals than the distribution with $\alpha = 0.6$ adopted in the remainder of this work (e.g., Figure 11).

models implicitly assume the same dust extinction for both star-forming galaxies and AGNs: a plausible assumption, given that the AGN NLR gas is at $>\text{kpc}$ scales from the galaxy center (Bennert et al. 2002), similar to locations of HII regions. We directly compare the dust extinction of BPT-classified AGNs and non-AGNs in Figure 29, quantified as the excess Balmer decrement $\Delta \log(\text{H}\alpha/\text{H}\beta) \equiv \log(\text{H}\alpha/\text{H}\beta)_{\text{obs}} - \log(\text{H}\alpha/\text{H}\beta)_{\text{i}}$. Here the intrinsic Balmer decrement $(\text{H}\alpha/\text{H}\beta)_{\text{i}} = 2.86$ for HII regions and $(\text{H}\alpha/\text{H}\beta)_{\text{i}} = 3.1$ for AGNs (Osterbrock & Ferland 2006). Compared to galaxies of the same (high) stellar mass, AGNs have nearly identical Balmer decrements, justifying our assumption that both HII region and AGN NLR gas are affected by the same dust extinction.

Constant-Metallicity NLR and Constant M_{BH}/M_* Ratio

To test a constant, metal-rich NLR we replace Equation 13 with:

$$\log([\text{NII}]/\text{H}\alpha) = 0.0 \pm 0.2, \quad (\text{A1})$$

In other words, we fix the AGN $[\text{NII}]/\text{H}\alpha$ ratio to a normal distribution rather than having it depend on the $[\text{NII}]/\text{H}\alpha$ ratio of the host galaxy. The metal-rich NLR assumption uses the same equations as the Section 5 simulations (Equations 10–12) for the other AGN NLR line ratios: this means there is no difference between the metallicity-dependent and metal-rich VO87 AGN simulations. We follow the same steps outlined in Section 5.2 to create a “uniform- $L_{\text{bol}}/L_{\text{Edd}}$ ” simulation with a metal-rich AGN NLR, using the same $\log(\lambda_{\text{min}}) = -5.0$ for BPT AGNs and $\log(\lambda_{\text{min}}) = -5.5$ for VO87 AGNs to normalize the Eddington ratio distribution and minimize the total χ^2 in comparing

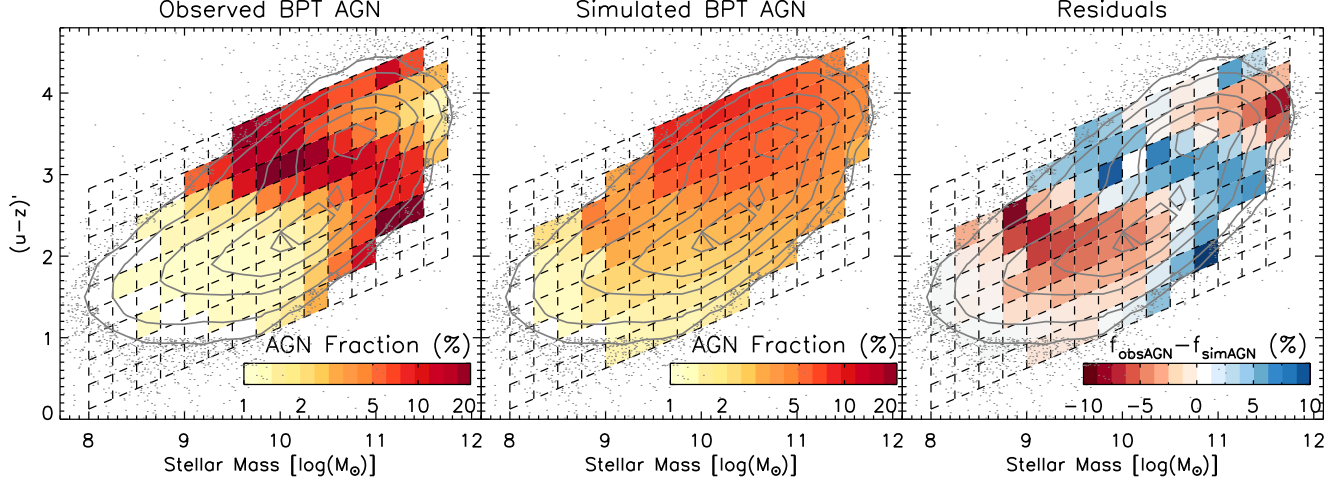
BPT AGNs: Flat $\alpha=0.05$ Edd ratio distribution

FIG. 33.— A comparison of the observed and simulated BPT AGN fractions in the galaxy color–mass diagram for a simulation with a “flat” Eddington ratio distribution of power-law slope $\alpha = 0.05$. The simulation with a flat $L_{\text{bol}}/L_{\text{Edd}}$ distribution produces a significantly poorer fit to the data than the steeper $\alpha = 0.6$ $L_{\text{bol}}/L_{\text{Edd}}$ distribution.

to observations. This uniform- $L_{\text{bol}}/L_{\text{Edd}}$, metal-rich NLR simulation for BPT AGNs is compared to observations in the color–mass diagram in Figure 30.

We additionally test a different relationship between black hole mass and galaxy properties by replacing Equation 8 with:

$$M_{\text{BH}}/M_* = 0.001, \quad (\text{A2})$$

with an intrinsic scatter of 0.5 dex. This is consistent with the $M_{\text{BH}}/M_{\text{bulge}}$ relation of Häring & Rix (2004), assuming $M_{\text{bulge}} = M_*/1.4$. Aird et al. (2012) used a similar constant M_{BH}/M_* ratio in their study showing that X-ray AGNs have a uniform Eddington ratio distribution over a wide range of host galaxy stellar mass. In the local universe velocity dispersion correlates with black hole mass much better than does total stellar mass (e.g., Kormendy & Ho 2013), but several $z \gtrsim 1$ studies suggest that $M_{\text{BH}}/M_{\text{bulge}}$ evolves with redshift while M_{BH}/M_* is constant (e.g., Jahnke et al. 2009; Schramm & Silverman 2013; Sun et al. 2015). Thus there is some motivation for comparing a constant M_{BH}/M_* ratio with the $M_{\text{BH}} - \sigma$ assumption used in Section 5. We create a “uniform- $L_{\text{bol}}/L_{\text{Edd}}$ ” simulation with both a metal-rich NLR and a constant M_{BH}/M_* ratio following the same steps as in Section 5.2, minimizing the total χ^2 by setting $\log(\lambda_{\text{min}}) = -5.75$ in both the BPT and VO87 simulations. Figure 31 displays this uniform- $L_{\text{bol}}/L_{\text{Edd}}$, metal-rich NLR, constant- M_{BH}/M_* simulation for BPT AGNs in the color–mass diagram.

Table 1 compares the $\chi^2/1000$ values from each simulation for BPT and VO87 AGN fractions in the color–mass, sSFR–mass, and concentration–mass host galaxy diagrams. As seen in Figures 30 and 31, using a metal-rich AGN NLR or a constant M_{BH}/M_* relation results in significantly worse matches between the simulated and observed AGN fractions. Thus we are justified in using the metallicity-dependent NLR and $M_{\text{BH}} - \sigma$ relation for our simulations in Section 5.

Different Power-Law Slopes for the Eddington Ratio Distribution

The simulations in Sections 5 and 6 used a Schechter form of the Eddington ratio distribution (Equation 7) with a power-law slope $\alpha = 0.6$. Observations of X-ray and narrow-line AGNs, as well as models for AGN fueling, are consistent with this parameterization (Hopkins & Hernquist 2009; Kauffmann & Heckman 2009; Aird et al. 2012), but neither are strongly constraining due to their considerable uncertainties. Other observations suggest a somewhat shallower power-law slope: Hickox et al. (2014) argue that $\alpha = 0.2$ better describes the observed L_{AGN} –SFR correlation, and Schulze & Wisotzki (2010) measure $\alpha = 0.05$ for low-redshift broad-line AGNs. Here we test the effects of adopting shallower Eddington ratio distributions on the fit between the simulated and observed AGN fractions for the uniform- $L_{\text{bol}}/L_{\text{Edd}}$ model.

Figure 32 compares the uniform- $L_{\text{bol}}/L_{\text{Edd}}$ simulation with an Eddington ratio distribution of slope $\alpha = 0.2$ with the observed AGN fraction. This “shallow” $L_{\text{bol}}/L_{\text{Edd}}$ distribution was normalized (minimizing the χ^2) using a lower $\log(\lambda_{\text{min}}) = -7$ for BPT AGNs and $\log(\lambda_{\text{min}}) = -6.5$ for VO87 AGNs. The fit to the observed AGN fractions is significantly worse than the fiducial $\alpha = 0.6$ used in Sections 5 and 6, with χ^2 values $\sim 1.5\times$ higher, as shown in Table 1.

The uniform- $L_{\text{bol}}/L_{\text{Edd}}$ simulation with a “flat” $\alpha = 0.05$ Eddington ratio distribution is compared to the observations in Figure 33. Normalizing the flat $L_{\text{bol}}/L_{\text{Edd}}$ distribution requires a very low minimum Eddington ratio: $\log(\lambda_{\text{min}}) = -10$ for BPT AGNs and $\log(\lambda_{\text{min}}) = -9$ for VO87 AGNs. The χ^2 values for the $\alpha = 0.05$ distribution are roughly double those of the fiducial $\alpha = 0.6$ Eddington ratio distribution (see Table 1), with a higher-amplitude “striping” pattern of residuals in the color–mass diagram. For a uniform Eddington ratio distribution in all host galaxy

types, the steeper $\alpha = 0.6$ Eddington ratio distribution provides the best (lowest- χ^2) match to the observed AGN fractions.